Correlating grain boundary properties to distributions during anisotropic grain growth - an interface field study in two and three dimensions

March 16, 2012

Debashis Kar

Materials Science and Engineering, Carnegie Mellon University

Advisors :

Prof. A D Rollett

Prof. G S Rohrer

Committee :

Prof. D E Laughlin

Prof. R F Sekerka

Prof. P C Pistorius

Abstract

A multi-phase field method is presented both in two and three dimensions to model grain boundary migration and to study the effect of anisotropy in boundary energy on populations during grain growth. The misorientation-dependent distribution of boundaries is correlated to the anisotropy in boundary energy, which scales with the sum of surface energies for grains on either side. These surface energies are inclination-dependent in the crystal frame of reference. The steady-state morphology of isolated grains, shrinking with time, is different for varying anisotropic conditions. For a given anisotropy of boundary energy, it is shown that the evolution of grain boundary character is different in the case of isolated shrinking grains when compared to that of polycrystalline grain growth. The effect of different boundary conditions imposed at junctions is found to be the key factor influencing the development of anisotropic grain boundary character in polycrystalline systems. In the later half of the present work grain boundary energies for arbitrary boundary types are estimated through use of appropriate interpolation methods and distance metrics. The anisotropy in boundary populations is correlated to the anisotropy in interpolated energies to demonstrate that for an initial random texture, an inverse relation between boundary energy and population holds true across the entire grain boundary space.

Contents

List of Figures

List of Tables

Description	Symbol
Boundary energy	γ
Boundary mobility	m
Reduced mobility	μ
Boundary width	λ
Boundary curvature	k
Anisotropy strength	δ
Angle between normal and [001]	θ
Angle between projection of normal on xy plane and [100]	φ
Gridstep	Δx
Timestep	Δt
Mean grain radius	R
ith phase-field variable	ϕ_i
Interface field corresponding to *ith* and *jth* phase-fields	ψ_{ij}
Potential energy coefficient	w
Kinetic energy coefficient	ε
Mobility coefficient	τ
Gradient operator	∇
Laplacian operator	Δ or ∇^2
Potential and kinetic coefficients	(A, B)
Arbitrary units	$a.u.$
Multiples of Random Distribution	MRD
Ratio of line energies (or mobilities)	r
Grain boundary 5-parameter indices	$(c_1, c_2, c_3, c_4, c_5)$
Euler angles (Bunge)	(ϕ_1, Φ, ϕ_2)
ith symmetry operator	O_i
Orientation matrix for grain A	g_A
Boundary normal	(n_x, n_y, n_z)
Distance between boundary types using Morawiec's metric	χ^2
Distance using Olmsted's metric	d^2

Table 1: Symbols and notations

Chapter 1

Introduction and background

1.1 Motivation

In the case of polycrystalline materials, it is often observed that the distribution of boundaries is non-random [57, 32]. This non-random or *anisotropic* distribution of grain boundaries can have a significant effect on macroscopic properties of these materials, which include but are not limited to fracture toughness, corrosion resistance or mechanical strength.

This has of course motivated the development of *grain-boundary engineered* materials, which have a high population of *special* boundaries (known as Σ or CSL boundaries), such that these materials have better mechanical properties compared to conventional materials having a random distribution of grain boundaries [51]. Some examples are worthy of mention here - lead-acid battery materials having a high population of these special boundaries (specifically $\Sigma 3$ boundaries) show greater resistance to corrosion and failure, and nickel-based alloys where the resistance to stress-corrosion cracking and the population of special GBs scale with each other (see Fig,1.1). Hence the motivation to engineer materials which are preferentially populated with certain boundaries types. And to produce such a non-uniform distribution of boundaries, it is necessary to alter boundary properties accordingly (as an inverse relation appears to exist between boundary energies and populations in metals and ce-

ramics [57, 56, 32]). Hence the next obvious question - is there a natural correlation between interface populations and interfacial properties, or in other words, given a set of interfacial properties, can one predict interface distributions ? If we turn this question around, we can also ask - if we want a certain distribution of grain boundaries, what sort of anisotropic boundary properties should we have ?

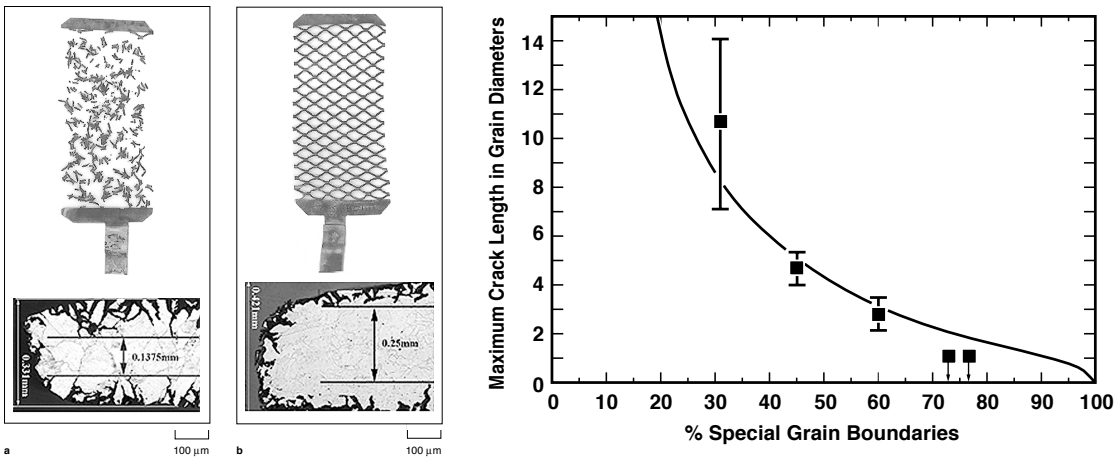

Figure 1.1: (a) Intergranular corrosion and cracking in conventional lead-acid batteries having low (13%) population of *special* boundaries compared to (b) which shows relatively negligible cracking and has a high population (about 63%) of CSL boundaries introduced through GBE. (c) Maximum intergranular crack length and the fraction of special boundaries in a Ni-based alloy scale with each other. This figure was reproduced from reference [51].

1.2 Background

Non-uniform grain boundary properties can play a significant role on their populations, and result in grain-boundary texture in the material. Texture, in the present context, implies a non-uniform distribution of crystallographic properties, indicating that either the grains (in the polycrystalline framework) are preferentially oriented along certain directions, or certain boundary types are more populated than others, or both. The material is then said to have an *orientation texture* or a *boundary texture* respectively. It is to be noted that grain boundaries in three dimensions have five degrees of freedom - three related to the misorientation between

the crystals on either side (needed to rotate one crystal to another), and two related to the inclination of the boundary plane in space (see Fig.1.2). So grain-boundary texture can either be misorientation or inclination based.

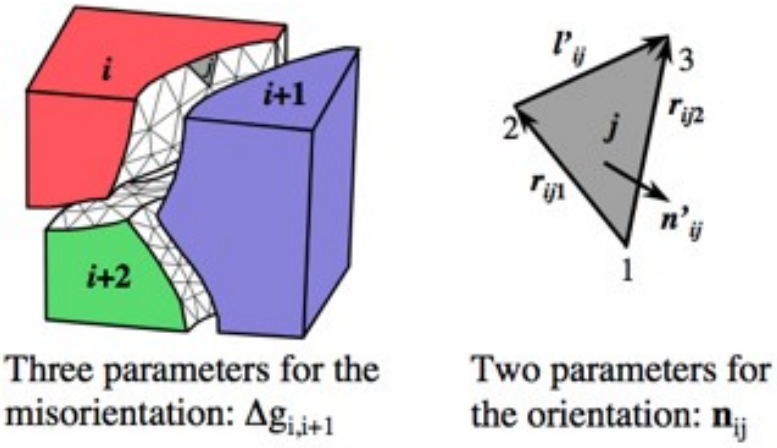

Figure 1.2: Grain boundaries in three dimensions have five degrees of freedom - the first three related to crystal misorientation, and the last two to the inclination of the boundary normal in space. This figure was reproduced from reference [55].

Grain boundary properties, like energy or mobility can be related to macroscopic observables (like boundary velocity v) as

$$\nu = m\gamma k \tag{1.1}$$

where, m, γ and k denote mobility, energy and boundary curvature respectively. In curvature-driven models, grain boundaries move along the boundary normal towards their centre of curvature. The mobility and energy terms are often combined as a reduced mobility $\mu = m\gamma$.

Grain boundaries (GB) meet at junctions, at angles determined by the relative energies of the GB segments in these junctions. Knowing the values of these boundary energies, one can use Neumann's triangle for mechanical equilibrium, and show that these angles are related by the following relation [4], if one assumes that the boundary energy is inclination (or boundary-plane) independent .

$$\frac{\gamma_{12}}{sin\alpha_3} = \frac{\gamma_{23}}{sin\alpha_1} = \frac{\gamma_{31}}{sin\alpha_2} \tag{1.2}$$

where, γ and α denote the boundary energy and the included angle opposite to boundary. In the isotropic case, where all boundaries have equal energies, boundaries meet at angles equal to 120° at the triple junctions. When boundaries have different energies, they rotate and lengthen till mechanical equilibrium is achieved at junctions (see Fig.1.3).

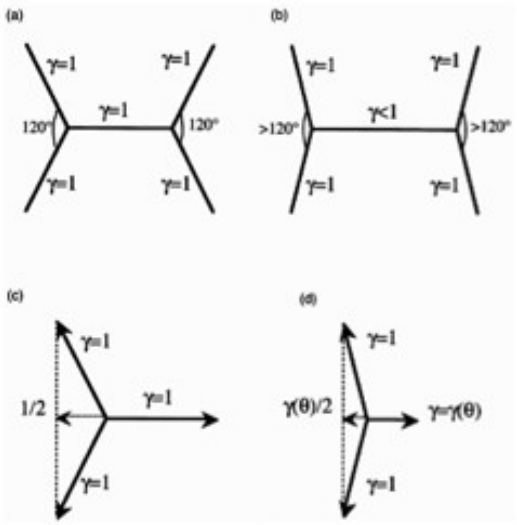

Figure 1.3: Grain boundaries rotate and lengthen at boundary junctions till mechanical equilibrium is restored (figure reproduced from [23]).

In case, the boundary energies are inclination-dependent (that is varying with the boundary normal), torque terms appear which tend to rotate boundaries to low-energy inclinations. Herring's equations for mechanical equilibrium at boundary junctions for such cases can be expressed as (refer [4])

$$\sum \left(\gamma \hat{t} + \frac{\partial \gamma}{\partial \varphi} \hat{n} \right) = 0 \tag{1.3}$$

where, φ is the inclination angle of the boundary, and $\hat{t}$ and $\hat{n}$ represent the tangent and the normal vectors to the grain boundary respectively (see Fig.1.4).

An alternate way of representing inclination-dependent energies was given by Cahn and

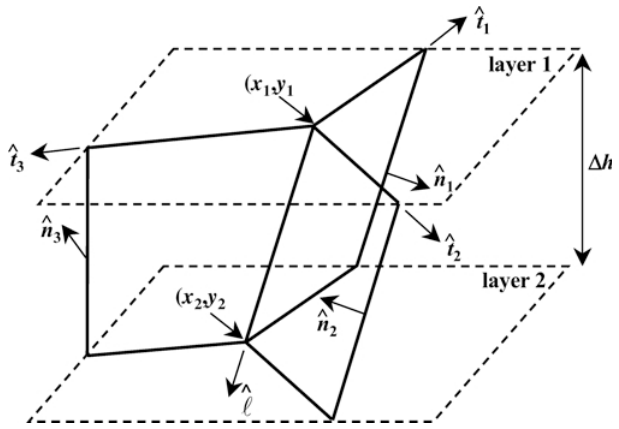

Figure 1.4: Torque terms tend to rotate bondaries to low-energy inclinations, when the boundary energy is inclination-dependent. This figure was reproduced from reference [55].

Hoffman [5, 6], where they replaced energies $\gamma(n)$ and torques $\frac{\partial \gamma}{\partial n}$ by a single capillarity vector $\xi(n)$ (see fig.1.5). Cahn showed that the ξ-plot is similar to the $\gamma(n)$ Wulff plot, and it gives a more complete description of surface energy anisotropy and expected equilibrium shapes.

Regarding grain growth kinetics, the von-Neumann-Mullins relation [refer [45, 69]] expresses the rate of grain growth in two dimensions as

$$\frac{\partial A}{\partial t} = -m\gamma(2\pi - \sum_{i=1}^{n} \alpha_i) = -2\pi m\gamma(1 - \frac{n}{6}) \tag{1.4}$$

where, A, α_i denote grain boundary area and turning angle at each grain corner (or triple junction), as seen in Fig.1.6.

The simplest models of grain growth assume isotropic properties where all boundaries have equal mobilities and energies irrespective of grain boundary type [3, 62]. As can be derived from the previous relation, one expects that in two dimensions, grains having more than six edges grow, while others shrink with time, during isotropic curvature-driven grain growth. As stated earlier, boundary velocity v is proportional to curvature $k = \frac{1}{r}$. Hillert proposed a simple power-law equation relating mean grain radius R to time t (in two dimensions) [refer [22]]

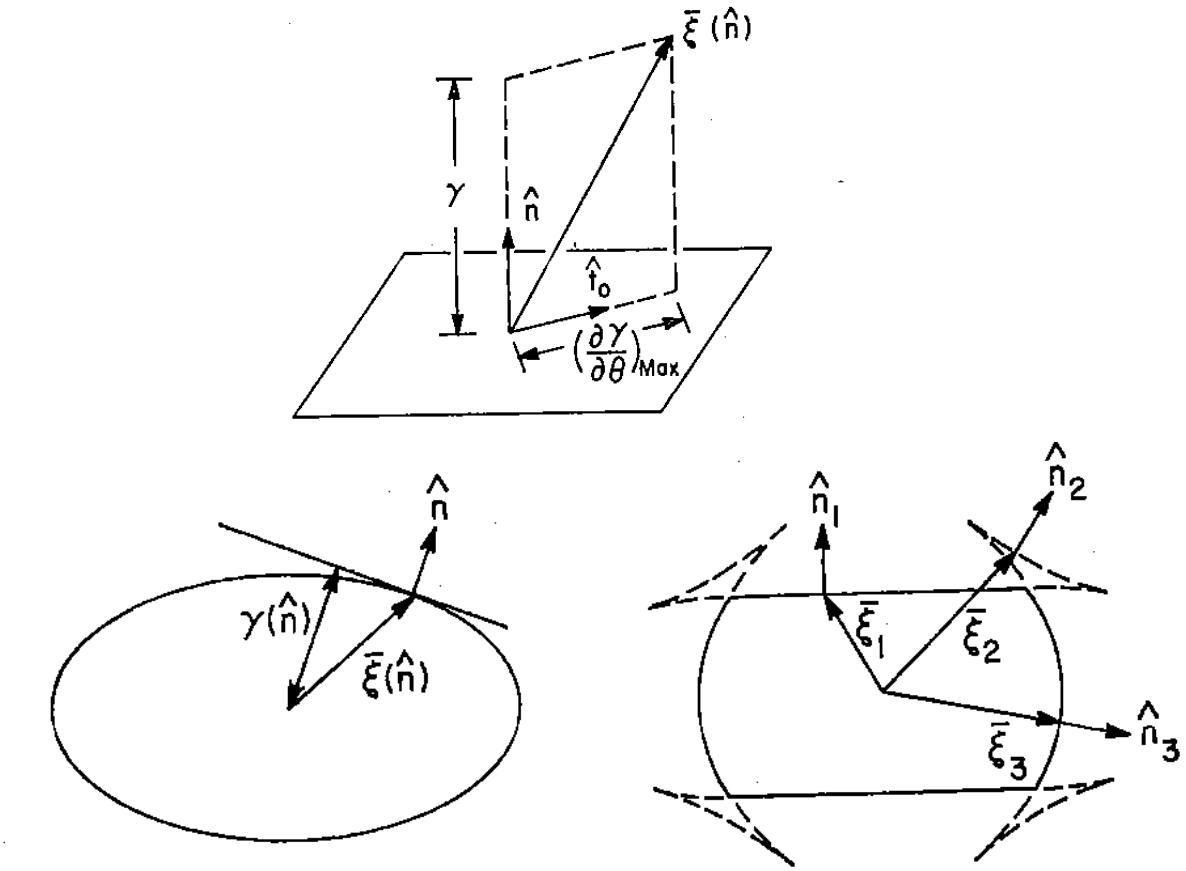

Figure 1.5: (a) Defining of ξ-vector (b) Similarity of the Wulff plot and the ξ-plot. These were reproduced from Cahn's paper [5].

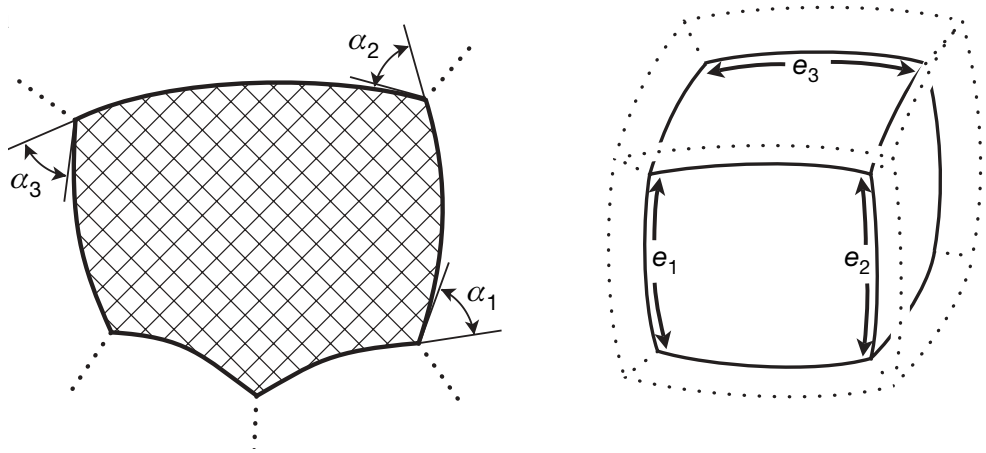

Figure 1.6: (a) Representation of grains in a two dimensional polycrystalline network - whether a grain grows or shrinks with time depends on topological factors (as its number of sides) (b) corresponding representation of idealized grain in three dimensions (reproduced from reference [36]).

$$v = \frac{\partial R}{\partial t} = -\alpha m \gamma k \tag{1.5}$$

resulting in $R^p - R_0^p = Bt, p = 2$, R and R_0 being the average grain radius at time $t = t$ and $t = 0$ respectively. It has been shown by polycrystalline models of grain growth [3, 62] that a power-law exists for domain growth, where the average grain area A linearly scales with time t

$$A - A_0 = Kt^n, n = 1 \tag{1.6}$$

In three dimensions, the von Neumann's relation was generelized by Srolovitz et al. as [36]

$$\frac{\partial V}{\partial t} = -2\pi m \gamma \left(L(D) - \frac{1}{6} \sum_{i=1}^{n} e_i(D) \right) \tag{1.7}$$

where, $L(D)$ denotes a linear measure of domain D, and e_i represents the length of ith triple line of domain D, $1 \leq i \leq n$ (see Fig.1.6).

It has been shown, both in experimental and simulation studies, that grain boundary properties do have a relation to their populations. In magnesia, the boundary energy and population are inversely correlated [57], as seen in Fig.1.7. Grain boundary planes having low energies ($\{100\}$ in this case) are relatively more populated. In aluminium, planes with low surface energies ($\{111\}$ in this case) have higher populations [56]. Similarly in nickel (another face-centred cubic metal), $\{111\}$ planes being low in energy are more populated [32] (see Fig.1.7), supporting the notion that an inverse relation exists between grain-boundary energies and distributions.

Although energy γ and mobility m are related to the boundary velocity v as in eq. 1.5, recent work indicates these are independent of each other. Olmsted *et al.* performed a series of molecular-static simulations on bicrystal geometries and extracted realistic values of grain boundary energies and mobilities of a limited set of 388 boundary types [49]. Comparing

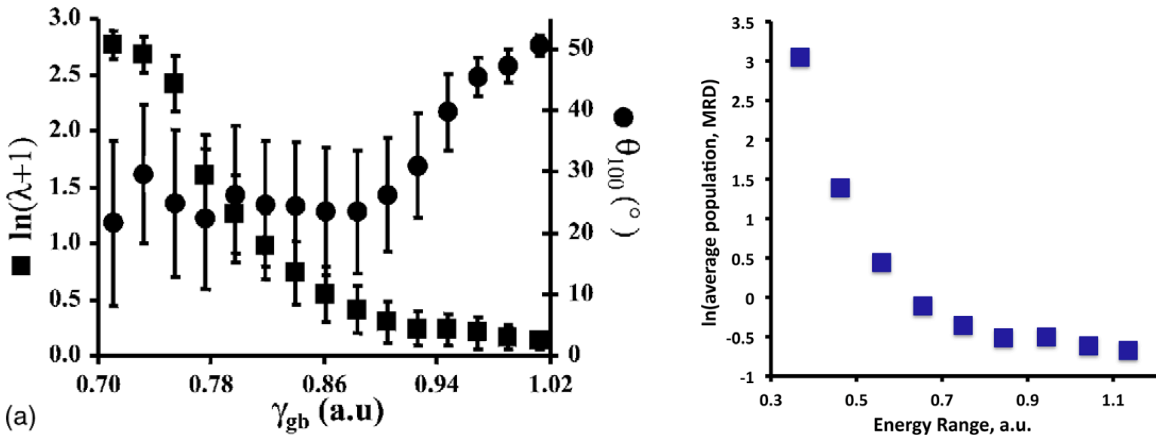

Figure 1.7: (a) Populations plotted vs. grain-boundary energies in magnesia (see squares) - note they are inversely related, as also in (b) nickel. Figures reproduced from [57, 32].

the energies of these boundaries with their mobilities no obvious correlation seems to exist. In fig. the variation of boundary energy with boundary mobility is shown for boundary types refered to as $\Sigma 3$ and $\Sigma 5$. Some low-energy boundaries have low mobilities (such as the coherent $\Sigma 3$ boundaries), but this does not always hold true. Also there does not appear to a correlation between boundary width (across which crystal orientation changes from one grain to another) and boundary energy - coherent $\Sigma 3$ boundaries have low width and low energies, but this should not imply that there is a direct scaling between boundary width and boundary energy.

This inverse relationship is predicted by simulations of grain growth in materials having anisotropic boundary energies. Gruber et al. showed, by use of finite-element simulations, that low-energy boundary planes are more populated, (see Fig.1.9) and that an anisotropy in boundary energy has a greater effect on boundary distributions than boundary mobility [17]. In a later paper, using the framework of a discrete model (Monte Carlo) they showed that an anisotropy in boundary energy has a greater effect on misorientation distributions than an anisotropy in mobility [19]. The energy function used has a form identical to one proposed by Read-Shockley [54], where the boundary energy scales with the misorientation angle for low misorientations, and is constant for high misorientations (typically greater than

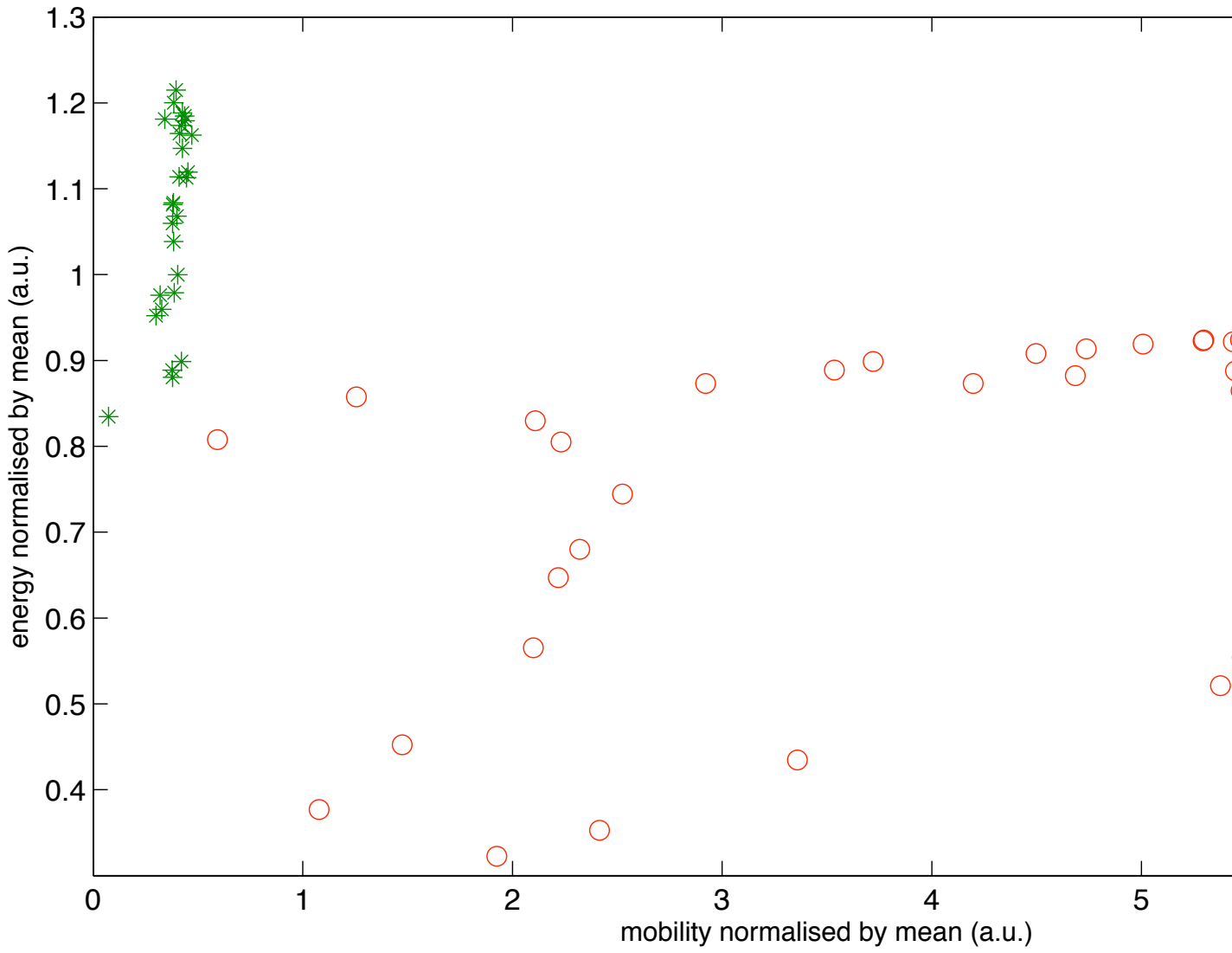

Figure 1.8: Variation of boundary energy with mobility for boundary types Σ3 and Σ5. These values have been extracted from recent work by Olmsted *et al [49]*. There appears to be no direct correlation between the two quantities.

15°), as in Fig.1.10. As can be seen in Fig.1.11, misorientation distributions (in multiples of random density MRD) scales inversely with the misorientation-based GB energy.

$$\gamma_{RS}(\theta) = \left(\frac{\theta}{\theta'}\right)\left[1 - ln\left(\frac{\theta}{\theta'}\right)\right], \theta \leq \theta' \tag{1.8}$$

$$\gamma_{RS}(\theta) = 1, \theta > \theta' \tag{1.9}$$

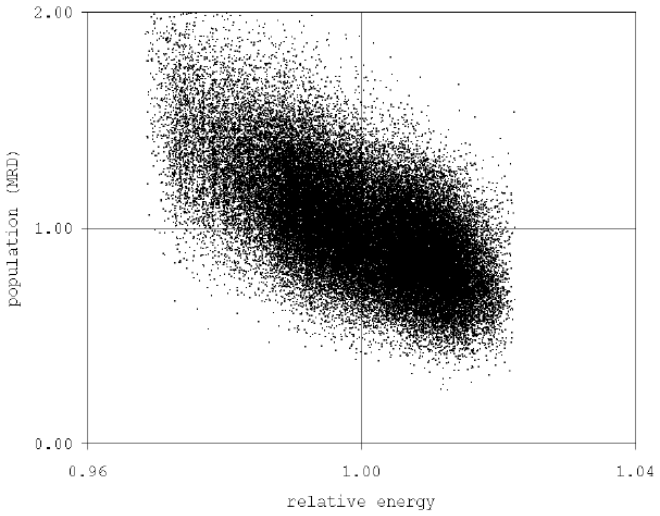

Figure 1.9: Interface populations plotted with relative GB energies - note inverse relation inspite of significant scatter. This figure was reproduced from reference [17].

Kazaryan et al. simulated anisotropic grain growth, in two dimensions, using a diffused-field approach (a phase-field model where boundaries have a finite width, and one does not explicitly need to record their position) and arrived at similar conclusions [28]. Upmanyu et al. showed that an anisotropy in boundary mobility only affected the overall rate of grain growth, whereas an anisotropy in boundary energy resulted in non-uniform grain boundary distributions (compared to distributions when the boundary properties were assumed to be isotropic), as can be seen in Fig.1.12 [68].

As explained earlier, grain boundaries (in three dimensions) have five degrees of freedom. Hence a complete anisotropic description of grain-boundary energy should depend both on

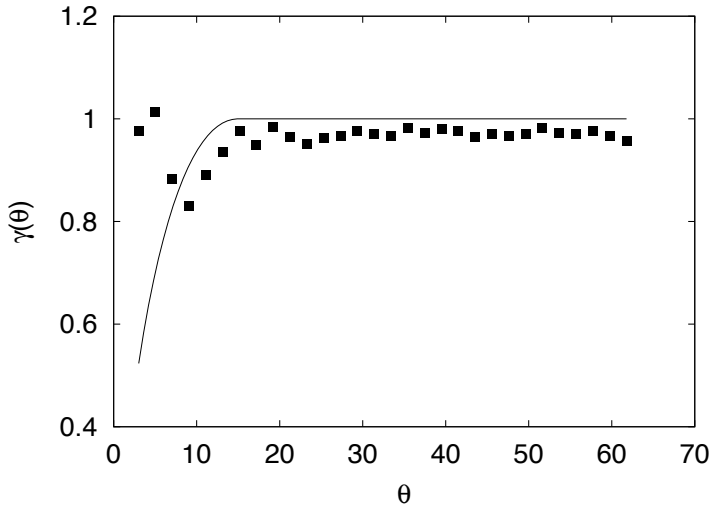

Figure 1.10: Read-Shockley based variation of boundary energy with misorientation - a GB misoriented by more than 15° is typically regarded to be a high-angle GB. The dotted line represents the energy function derived for magnesia from simulations. (figure reproduced from [20]).

lattice misorientation (across the boundary) and on the inclination of the boundary normal. It has been experimentally observed in face-centred cubic metals, that there is an appreciable variation of boundary energy with inclination, at a constant misorientation. A couple of examples of GB energy variation in fcc metals are shown here (see Figs.1.13,1.14,1.15) for reference - the first depicts the variation of energy with misorientation angle [56], and the variation of boundary energy for the particular case of symmetric-asymmetric tilt [001] (and [110] symmetric tilt) boundaries in aluminium [50]. In the second case, the variation of grain boundary energy with misorientation angle for the case of symmetric [001] tilt boundaries, and the overall variation of GB energy (over all misorientations) with inclination is shown for nickel [32].

The simplest anisotropic models assume that the boundary energy does not depend on inclination, and varies only with misorientation, having a form similar to the Read-Shockely expression shown above (see fig.1.10). Holm et al. simulated grain growth using a Monte-Carlo method, with a misorientation-based GB energy, and show that although texture played a significant role in growth kinetics, in all cases low-energy misorientations (which in

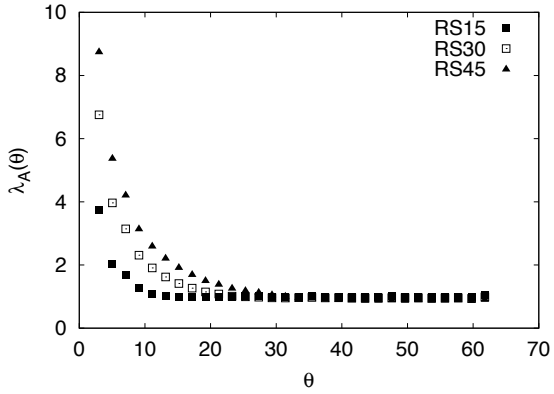

(a) Area weighted MDFs in multiples of random distribution (MRD).

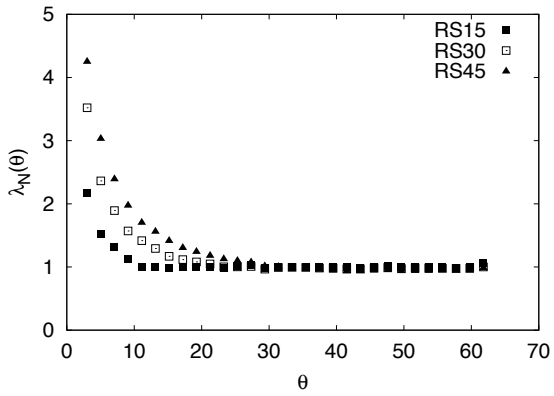

(b) Number weighted MDFs in multiples of random distribution (MRD).

Figure 1.11: (a) Number-weighted and (b) area-weighted misorientation distributions as derived from simulations by Gruber et al. This figure was reproduced from reference [19].

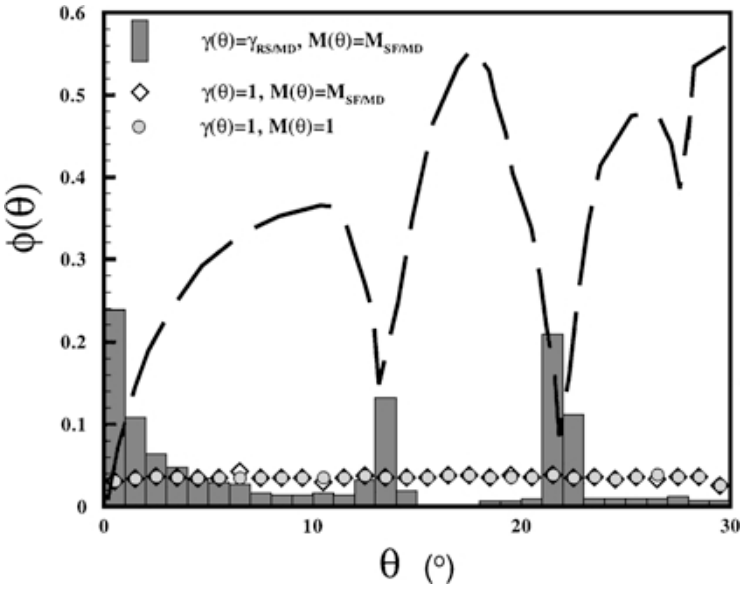

Figure 1.12: MDF plotted (histograms) with a Read-Shockley based boundary energy (dotted line) - mobility anisotropy gives a distribution (diamonds) similar to the isotropic case (circles) (reproduced from [68]). Note that certain special or CSL boundaries have been assigned relatively low energies.

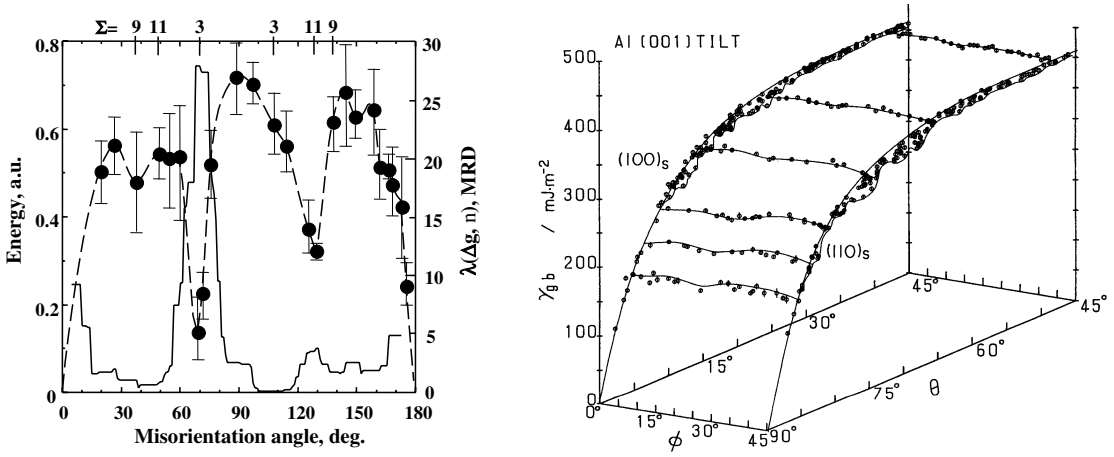

Figure 1.13: (a) Variation of boundary populations and energies with misorientation in aluminium for symmetric tilt [110] boundaries (reproduced from [56]), and (b) energy variation of symmetric-asymmetric tilt [001] boundaries (reproduced from [50]).

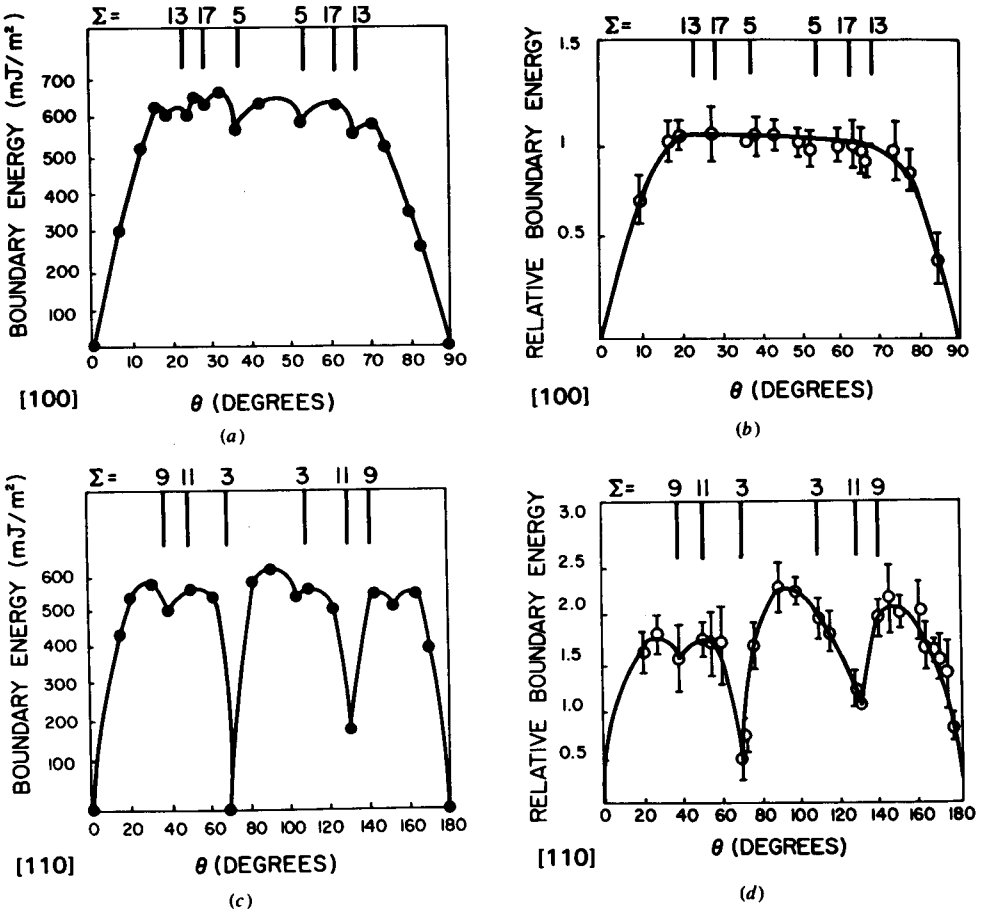

Figure 1.14: Calculated (a,c) and measured (b,d) energies for symmetrical [100] and [110] tilt boundaries in aluminium. This figure was reproduced from reference [14].

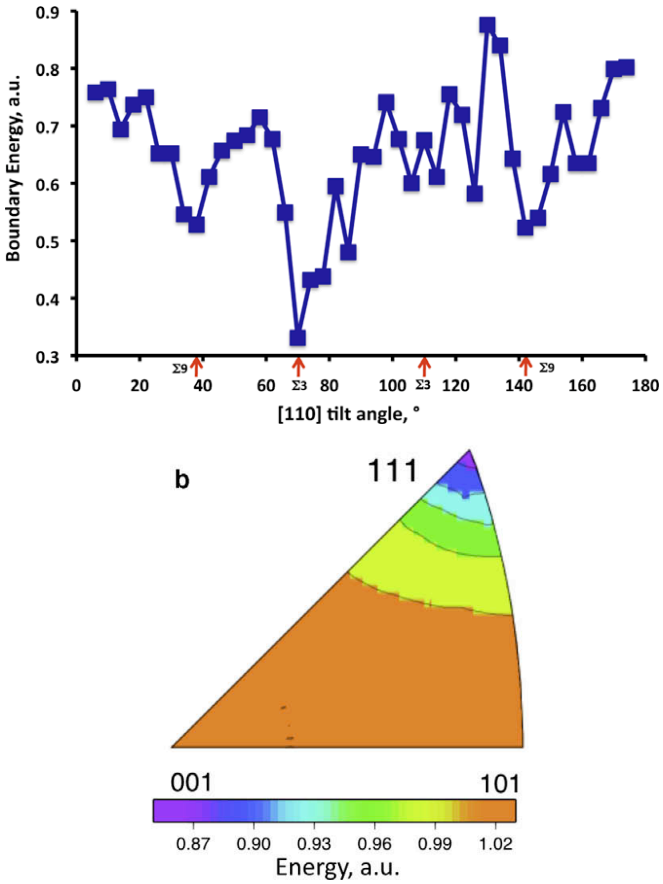

Figure 1.15: (a) GB energy for symmetric tilt [110] boundaries varying with misorientation angle (b) averaging over all misorientations, {111} planes (in the crystal reference frame) have the lowest energy in nickel (reproduced from [32]).

this case correspond to low-angle boundaries) lengthened at the expense of high-energy ones [23]. Similar conclusions were reached at by Gruber et al. using Monte Carlo simulations (in two and three dimensions), again with a purely misorientation-based boundary energy (and random texture), where both number-weighted and area-weighted statistics showed a high fraction of low-angle boundaries [19, 20].

On the other hand, models which incorporate an inclination-based energy have been developed using a phase-field approach. It is to be noted that such models have been largely applied to study solidification phenomena and closely mimic dendritic morphologies. For the case of two dimensions, an inclination-based energy of the following form was used by Karma et al. [27, 11]

$$\gamma(\theta) = \gamma_0 \left(1 + \delta \left(|sin\theta| + |cos\theta|\right)\right) \tag{1.10}$$

which, considering spherical symmetry, can be reduced to

$$\gamma(\theta) = 1 + \delta cos(m'\theta) \tag{1.11}$$

where, δ, m' denote the strength of anisotropy and the order of symmetry ($m' = 4$ for a four-fold symmetric function) respectively. θ denotes the inclination angle that the boundary normal makes with a reference axis (the sample x axis in this case). A similar form of spherical anisotropy was observed in two-dimensional experimental observations of solidified droplets in Al-Cu and Al-Si systems by Napolitano et al. [47] .

Changes in conserved and non-conserved variables with time are determined using relevant governing equations [31].

$$\frac{\partial \phi}{\partial t} = -m \left[\nabla^2 \phi - \frac{\partial f(\phi, c)}{\partial \phi}\right] \tag{1.12}$$

$$\frac{\partial c}{\partial t} = \nabla^2 \left(m \left[\nabla^2 c - \frac{\partial f(\phi, c)}{\partial c}\right]\right) \tag{1.13}$$

where, $\phi = \{\phi_i, 1 \leq i \leq n\}$ and $c = \{c_j, 1 \leq j \leq p\}$ represent non-conserved and conserved species respectively.

The variation of boundary energy γ with inclination θ results in the introduction of higher derivatives in the evolution equations (as γ_θ) which might be discontinuous near cusps (minima in the inclination-energy Wulff plots). Hence, often regularization methods are used where sharp cusps are replaced by smooth differentiable functions [11]. Voorhees et al. used an alternative convexification method, which ensured that interfacial stiffness $(\gamma + \gamma_{\theta\theta})$ is positive for all inclinations [13]. These adjustments are necessary to ensure that the method remains stable for boundaries at all inclinations, and is able to reproduce faceted morphologies at the same time.

Recently Moelans et al. developed a phase-field approach for studying anisotropic grain growth in two dimensions [40, 41], incorporating an anisotropy in boundary energy which is dependent both on lattice misorientation and inclination. The interfacial width w was maintained constant irrespective of boundary inclination, while the grain boundary energy γ varied with the boundary normal $\hat{n}$. But the method is limited to two dimensions and not been used to model large-scale microstructure evolution. Also as mentioned above, non-convex inclinations need to be regularized for maintaining stability in simulations.

Coming to the issue of model development for simulating grain growth in three dimensions, it is to be noted that such models are either limited by overall domain size or by the nature of the anisotropic function used. Grest et al. simulated normal grain growth in three dimensions (using a Monte Carlo framework) using isotropic grain-boundary properties [2]. Wakai et al. studied steady-state grain growth kinetics using a finite-element solver (the Surface Evolver), assuming all boundaries have equal energies and mobilities [70]. Ivasishin et al. developed a three-dimensional Potts model using a misorientation-based anisotropic mobility [25], and looked at the effect of initial texture and a misorientation-based boundary mobility on the grain growth exponent.

Using a discrete framework, like the Potts model, it is tedious to directly extend an

anisotropic model from two to three dimensions, due to inherent difficulties in deriving gradients and boundary normals for curved interfaces in three dimensions (as in two dimensions) for a voxelised representation of a polycrystalline grain structure. One has to smooth and interpolate otherwise *jagged* boundaries to derive approximate inclinations in such a case [26, 61]. On the other hand, it is quite straightforward to extend diffused models (such as the phase-field approach) to higher dimensions, where one need not explicitly track boundaries, which are inherently defined as locations of high gradients in field variables.

Kim et al. simulated ideal grain growth in three dimensions using a diffused model of interface fields developed by Steinbach and Pezzolla [63]. The computations were carried on a relatively large domain ($420 - cubed$) and corresponding grain growth statistics were extracted, but the boundary properties were assumed to be isotropic [29]. Krill and Chen developed a novel grain-reassignment procedure to model large-scale grain growth in three dimensions, but here also an uniform boundary mobility (and energy) was used [24]. Saito et al. used an anisotropic mobility step-function (boundaries between grains belonging to different texture components are assigned an uniform high mobility compared to others) and used appreciably large domains ($320 - cubed$) [64]. On the other hand, an inclination-based anisotropic energy was incorporated in three dimensions by Karma and Rappel to model dendritic tip morphologies. The form of the energy function used was cubic-symmetric, and can be expressed as

$$\gamma = \gamma_0 \left[1 + \delta \left(cos^4\theta + sin^4\theta \left\{1 - 2cos^2\varphi sin^2\varphi\right\}\right)\right] \tag{1.14}$$

where, θ, φ represent the angle between interface normal and the crystal [001] axis, and the angle between the projection of the interface normal on the xy plane (in the frame of reference of the crystal) and the crystal [100] axis respectively [27, 53]. The model succesfully simulated the preferential selection of certain crystal inclinations over others (see Fig.1.16) for a relatively low anisotropy strength (less than 5%).

Similarly, Granasy et al. modeled polycrystalline alloy solidification, with an anisotropic

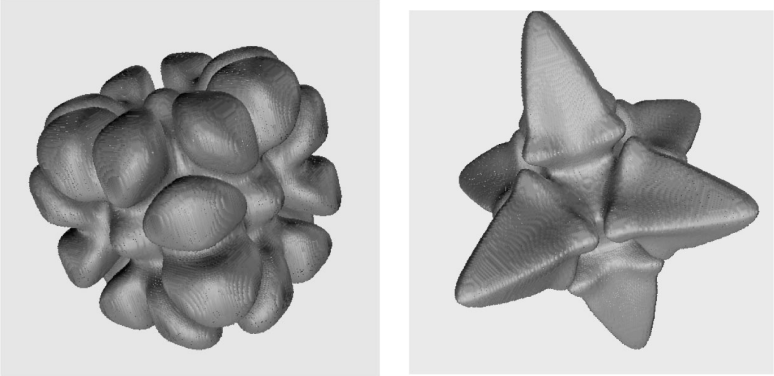

Figure 1.16: Dendritic morphologies for increasing strength of anisotropy. These are reproduced from [27] for (a) $\delta = 0$ and (b) $\delta = 0.047$ in eq.1.14.

inclination-based mobility (see relation given below), where growing nuclei were preferentially bounded by different crystal facets (depending on the relative strengths of ε_1 and ε_2 , see Fig.1.17) [52].

$$m(n) = m_0 \left[1 + \varepsilon_1 \left\{ \sum_{i=1}^{3} n_i^4 - \frac{3}{5} \right\} + \varepsilon_2 \left\{ \sum n_i^4 - 66 n_1^2 n_2^2 n_3^2 - \frac{17}{7} \right\} \right] \tag{1.15}$$

Napolitano and Liu used a similar expression as eq.1.15 to describe the shape anisotropy of Sn-rich particles in the Al-Sn system [46].

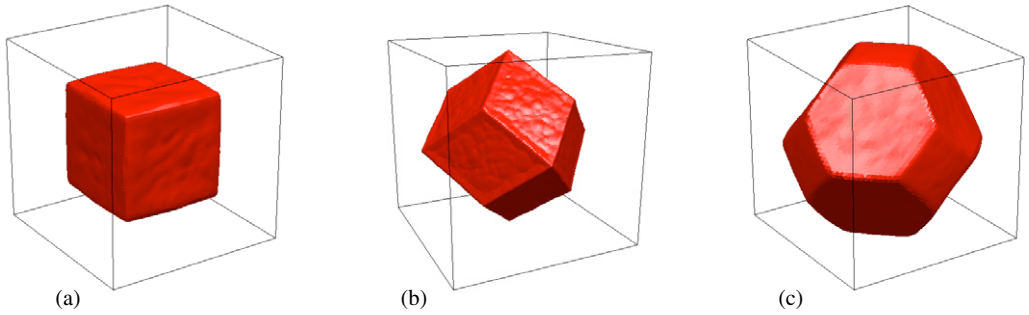

Figure 1.17: Solidification nuclei bounded by varying crystal facets for (a) $\varepsilon_1 = -1.5$, $\varepsilon_2 = 0.3$ (b) $\varepsilon_1 = 0$, $\varepsilon_2 = 0.6$ and (c) $\varepsilon_1 = 0$, $\varepsilon_2 = -0.3$ in eq.1.15 (reproduced from **(author?)** [52]).

1.3 Hypothesis

The present work seeks to demonstrate that an inverse corelation exists between grain boundary energies and populations, which holds both in two and three dimensions, for an initial random texture. Also it is hypothesized that mechanical equilibirum conditions at triple junctions have a significantly greater effect on the development of an anisotropic boundary character than kinetic factors (as boundary mobility), when boundary properties are non-uniform or anisotropic. Isolated grains should evolve differently from grains in a polycrystalline system due to the presence of boundary junctions. In polycrystalline systems, low-energy boundaries grow at the expense of high-energy boundaries, both in number and in area.

1.4 Objectives

The present work seeks to develop an interface-field method, both in two and three dimensions, to model large-scale polycystalline grain growth, incorporating anisotropic boundary properties. The use of an interface-field approach instead of the usual phase-field approach help to decompose multiphase field interactions as a sum of interactions of associated interface fields [63]. The microstructure is represented as a *sparse* array, where we store interface field values only for voxels at grain boundaries (and junctions) - this results in a significant reduction in requirements for computational time and memory [18]. Hence the present method can be used to simulate large-scale anisotropic microstructure evolution in three dimensions, in contrast to previous work [68, 41], and can produce more reliable statistics to better correlate the anisotropy in boundary distributions to the anisotropy in boundary properties.

In Chapter. 2 (Part-I), the interphase-field approach is presented and validated for model systems (for example the isotropic shrinkage of isolated grains). Effects of changing the boundary width and timsestep on boundary motion are explored. An energy-extension

procedure is presented to permeate anisotropic boundary energies along grain boundaries to boundary junctions. Details of the extension procedure are discussed in Appendix D. In Part-II, large-scale simulations are performed, in two and three dimensions. and the misorientation-dependent distribution of boundaries is correlated to the anisotropy in boundary energy, which scales with the sum of surface energies for grains on either side. These surface energies are inclination-dependent in the crystal frame of reference. The evolution of isolated grains is contrasted to the evolution of grains in a ploycrystalline network. Although it has been predicted that in polycrystalline systems equilibrium constraints at boundary junctions affect the development of anisotropy in boundary populations in previous work [30, 23], we seek to quantify this effect, by comparing the anisotropy in populations with varying equilibrium constraints imposed at boundary junctions. To test whether low-energy boundaries grow both in number and in area (as the *critical-events* model predicts [20]) or only in area (through a *boundary-lengthening* mechanism [23]) the anisotropy in number-weighted and area-weighted populations are compared.

In Chapter. 3, interpolation techniques are presented to estimate the distribution in grain boundary energies for face-centered cubic metals (like nickel and aluminum). Such techniques are necessary to determine the energy of arbitrary grain boundary types based on known energies of a limited number of GB types, which have been calculated using experimental methods [32] or simulations [49]. The variation of interpolated energies with the grain boundry type depends on the choice of the distance metric used. These interpolated energies are incorporated in the interface-field framework to predict grain boundary motion and microstructure evolution in real materials, and to better correlate the anisotropy in boundary character with observed boundary distributions in such materials. Details on incorporating interpolated energies in the interface-field method are discussed in Appendix C.

Finally in Chapter. 4, possible directions to extend the present capability of the interface-field approach are discussed - methods to reformulate the governing equations to account

for boundary torques are presented, such that a complete five-parameter description of anisotropic boundary properties can be incorporated in the present framework (see Appendix A). Details of numerical implementation are also presented (refer Appendix B).

Hence, the present method provides a robust approach to model anisotropic grain boundary migration and microstructure evolution, both in two and three dimensions, and is equipped to predict correlations between non-uniform boundary properties and populations. A relatively fast and parallelized method is presented which can be used to perform large-scale simulations in three dimensions and can be used to better correlate microstructure evolution observed in real materials to simulations.

Chapter 2

An interface-field method for anisotropic motion of grain boundaries

2.1 Introduction

One approach to represent a polycrystalline system and model interface migration is to use a phase-field approach, where each grain corresponds to a unique 'phase', and boundaries are diffuse having a finite width. This model was first used by Cahn and Allen to simulate antiphase domain coarsening [1]. It is different from discrete models of microstructural evolution, as one does not need to explicitly track the position of interfaces. Boundaries are inherently represented as regions of high gradients in field variables. Here grains do not abrubtly change orientation near boundaries, and grain boundaries have a finite width to accomodate gradients in orientation.

Chen et al modeled grain growth in three dimensions [24] assuming uniform boundary energies and mobilities using a phase-field approach. Sekerka et al. considered anisotropy in the kinetic prefactor in the evolution equations [67], and observed that the morphology of the steady-state kinetic shapes depended both on the width and depth of the cusp of the particular anisotropy function used. Instead, when an inclination-based anisotropy in the

gradient energy coefficient is considered, the variation of the free-energy functional yields additional terms, such as higher derivatives of the gradient energy prefactor with inclination [38]. The interface thickness in the aforementioned case scales with interfacial energy, hence to maintain a constant interface width irrespective of the boundary inclination, both the energy coefficient and the depth of the potential function should have a similar anisotropic variation with inclination [34].

Since higher derivatives of the anisotropic function with inclination (such as γ_θ) can be discontinuous in the vicinity of a cusp, the method can become ill-posed and unstable, and additional treatment of the energy functional is essential for these inclinations. Karma et al. used a modified version of the following inclination-based energy anisotropy $\gamma(\theta) = \gamma_0(1 + \delta(|sin\theta| + |cos\theta|))$ where they approximated the sharp cusps with rounded ones to simulate growth of dendritic tips [11]. Amberg used a similar regularization [33] to model evolution of a Widmanstatten morphology. Wise et al. used a Willmore regularization method, where the square of the mean curvature is added to the energy term to avoid instability near cusps and to smooth corners [66]. Voorhees used a energy convexification scheme [13] which ensured that the interfacial stiffness $\gamma + \gamma_{\theta\theta}$ is positive for all inclinations, to model the shape evolution of anisotropic crystals using a Cahn-Hilliard formulation (and conserved phase fields). [1]

In a recent paper, Wollants et al. simulated polycrystalline grain growth with arbitrary misorientation and inclination dependence in two dimensions, while maintaining a constant interface width [40]. Regularization of the energy function was necessary for the nonconvex

[1] If the inclination-based energy function $\gamma(\theta)$ has sharp cusps at certain inclinations, the interfacial stiffness $S(\theta) = \gamma + \gamma_{\theta\theta}$ can diverge at these cusps, leading to numerical instability at these inclinations [11]. In the work refered to, the first derivative γ_θ is discontinuous at cusps. The anisotropic function $\gamma(\theta)$ is modified such that sharp cusps are replaced by smooth rounded corners, enforcing continuity of γ and γ_θ. The interfacial stiffness, on the other hand, is discontinuous at cusps, but no longer suffers from divergence. In [13], Voorhees used a four-fold anisotropic function (similar to eq.2.10), which results in missing inclinations for anisotropy strengths greater than 1/15. For missing inclinations, the $1/\gamma$ (in two dimensions) plot is concave and the interfacial stiffness $\gamma + \gamma_{\theta\theta} < 0$, which leads to numerical instability at these inclinations. This was avoided by convexifying the anisotropic function $\gamma(\theta)$ such that the equilibrium shape remains identical (as the convex body of the $1/\gamma$ plot by tangent construction) while the interfacial stiffness $\gamma + \gamma_{\theta\theta} > 0$ for all inclinations.

regions of the interfacial stiffness (where $\gamma + \gamma_{\theta\theta} < 0$) when the grain boundary energy is strongly anisotropic with inclination. In another recent paper, Voorhees and McKenna investigated the effect of misorientation and the presence of junctions on the evolution of grain shapes using a set of two-grain simulations [39].

In the first half of the present chapter (**Part-I**), an interface field formulation is presented, both in two and three dimensions. The potential and kinetic energy functionals used in the present method are identical to ones used by Steinbach et al. [63]. We perform a set of two-grain simulations to validate the interface-field approach, and to compare the results with previous work by Voorhees *et al.* who used phase fields instead of interface fields to represent a grain structure [39, 42]. Effects of changing the interface width and timestep are explored. An energy extension procedure is introduced to permeate anisotropic energies along boundaries to junctions - hence the effect of different boundary constraints imposed at junctions on steady-state dihedral angles can be investigated. Based on these simulations, appropriate values of the timestep dt, interface width λ and grainsize R (or the grainsize to interface width ratio R/λ) are chosen.

In the second half of the present chapter (**Part-II**), a series of simulations for isolated shrinking grains are performed and the grain boundary character is extracted. Also a set of polycrystalline simulations are performed with different equilibrium conditions imposed at junctions using the energy-extension procedure. The anisotropy in misorientation-dependent grain boundary energies is correlated to the anisotropy in grain boundary character, where the grain boundary energy scales with the sum of inclination-dependent surface energy terms for the grains on either side. The purpose is to contrast the evolution of anisotropic boundary character for isolated grains to that of polycrystalline systems due to the presence of grain boundary junctions. Kinderlehrer *et al.* briefly commented that local equilibrium at triple junctions dictate the development of steady state boundary character in polycrystalline systems [30]. We seek to quantify this effect and to predict correlations between energies and populations in large-scale polycrystalline simulations starting from a random distribution of

grain orientations (random texture). The hypothesis that *the effect of equilibrium constraints at boundary junctions on the development of anisotropic boundary character is significantly greater than the effect of kinetic factors on the same*, is tested in the following manner - a set of polycrystalline simulations are performed, where the boundary mobility is strongly anisotropic (with an isotropic boundary energy) and the corresponding boundary character is compared to those extracted from simulations where the boundary energy is anisotropic (with an isotropic boundary mobility). This seeks to demonstrate whether an anisotropy in boundary energy or an anisotropy in boundary mobility has a strong influence on the grain boundary character. Also the number-weighted and area-weighted grain boundary distributions are extracted to investigate whether low-energy boundaries increase in area and not in number (as predicted by Holm [23]) or both (as Gruber *et al.* suggest [20]) resulting in the anisotropy in grain boundary populations. The effect of intial texture on grain boundary distributions is explored, and the anisotropy in boundary energy (and mobility) is correlated to the anisotropy in boundary populations.

Part I

- Model formulation

2.2 The interface field method

The phase field method represents a polycrystalline material as an ensemble of phase-field variables $\{\phi\}$ (an informative description of the phase-field formulation for modeling grain growth can be found in references [9, 8]). A phase-field variable ϕ_i is uniquely associated with the ith grain and has a value of 1 in the interior of grain i and 0 outside. Its value changes from 1 to 0 across a boundary ij that grain i shares with its neighbor j.

$$\{\phi\} = \{\phi_1, \phi_2, ...,\phi_\mathrm{i}, ..., \phi_\mathrm{N}\} \tag{2.1}$$

The free energy of such a system depends on the phase field values and their gradients, and can be defined as a summation of gradient and potential terms

$$F(\{\phi\}) = \int_\Omega (f^{gr} + f^{pot}) dV \tag{2.2}$$

The gradient and potential terms depend on the gradient and phase-field values respectively (as in eqs.2.3,2.4). The competing effects of these terms at boundaries tends to diffuse them, hence interfaces in phase-field models have a finite width.

The expressions used in the present work are identical to ones used by Steinbach [63]

$$f^{gr} = \sum_{\gamma=1}^{N} \sum_{\delta=\gamma+1}^{N} \frac{\varepsilon_{\gamma\delta}}{2} \nabla\phi_\gamma . \nabla\phi_\delta \tag{2.3}$$

$$f^{pot} = \sum_{\gamma=1}^{N} \sum_{\delta=\gamma+1}^{N} w_{\gamma\delta} \left|\phi_\gamma\right| \left|\phi_\delta\right| \tag{2.4}$$

As can be seen from eqs.2.3,2.4, the gradient energy functional f^{gr} is defined at boundaries where gradients are non-trivial, and tends to increase the interface width (to reduce gradients), while the potential energy functional f^{pot} (which is nontrivial only at boundaries) tends to decrease interface width to reduce its value.

The potential function decays rapidly as one moves from the interface to a grain interior

(see fig.2.1). The functions used in the fig.2.1 are of the form $\phi_1(x) = \left(\frac{x}{a}\right)$ and $\phi_2(x) = 1 - \phi_1(x)$ for the interface region $0 < x < a$, hence in the present example where the phase fields are approximated to be linear in the boundary region, they are equal to each other at $x = \frac{a}{2}$.

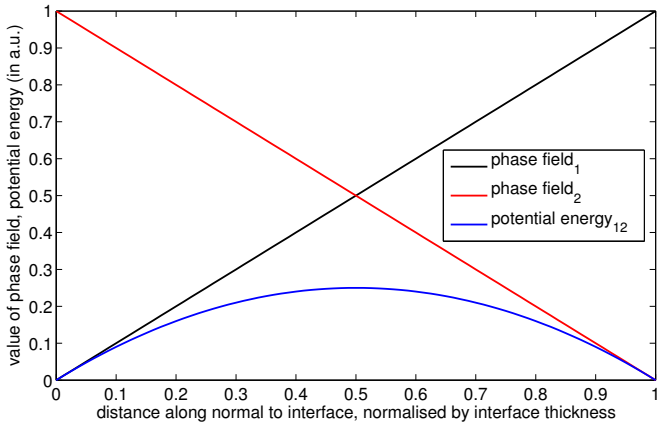

Figure 2.1: Variation of phase field values and potential energy function within the interfacial region.

An additional constraint is placed such that at any location, all the fields (also referred to as order parameters) add up to unity

$$\sum_{\alpha=1}^{N} \phi_i = 1 \tag{2.5}$$

The time-dependent evolution of these order parameters can be directly correlated to boundary motion. Since these fields are non-conserved (the volume of each grain changes with time), the time-dependent Ginzburg-Landau (TDGL) equation is used

$$\frac{\partial \phi_i}{\partial t} = -L \frac{\partial F}{\partial \phi_{\mathrm{i}}} \tag{2.6}$$

2.2.1 Interface fields and governing equations of motion

Since at any given time the phase-field values change only in the vicinity of boundaries, and those within a grain interior remain unaltered, one can, for purposes of computational

efficiency, solely determine the changes in these values within interfacial regions. We use an interface field method, developed by Steinbach et al. [63]. When two fields ϕ_α and ϕ_β intersect, an interface field $\psi_{\alpha\beta}$ is defined as (see fig.2.2). Since for the boundary region $(0 < x < a\ )\ 0 \leq \phi_\alpha(x), \phi_\beta(x) \leq 1$, the interface field $\psi_{\alpha\beta}$ varies as in fig.2.2 $(-1 \leq \psi_{\alpha\beta} \leq 1)$. Here, the phase fields have been approximated to be linear in the boundary region.

$$\psi_{\alpha\beta} = \phi_\alpha - \phi_\beta \tag{2.7}$$

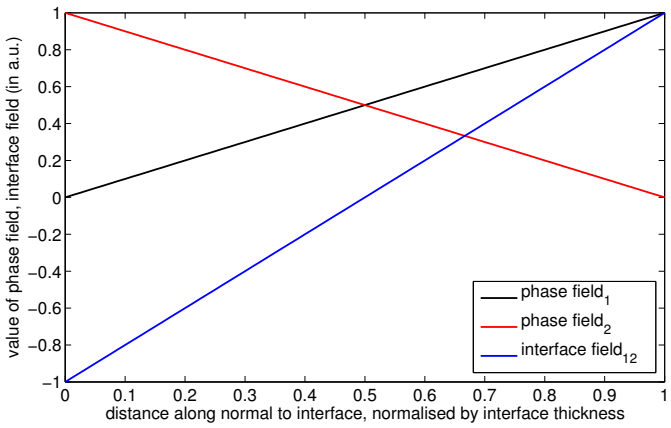

Figure 2.2: Variation of interface field and phase fields within interfacial region.

In case of grain boundaries, only one interface field is defined and in case of triple junctions (or higher junctions) three or more of these fields overlap (see fig. 2.3). In general for N phase fields $\binom{N}{2}$ interface fields exist.

Using the energy functional in eqs.2.3,2.4 the change in $\psi_{\alpha\beta}$ with time can be derived as [63]

$$\psi_{\alpha\beta}(t + \triangle t) - \psi_{\alpha\beta}(t) = m_{\alpha\beta}\left[\sum_{\gamma\neq\alpha}\left(-\frac{\varepsilon_{\alpha\gamma}}{2}\nabla^2\phi_\gamma - w_{\alpha\gamma}\phi_\gamma\right) - \sum_{\gamma\neq\beta}\left(-\frac{\varepsilon_{\beta\gamma}}{2}\nabla^2\phi_\gamma - w_{\beta\gamma}\phi_\gamma\right)\right]\triangle t \tag{2.8}$$

here, (ε, w) and m are the energy and mobility coefficients respectively. To incorporate anisotropic boundaries, these have to be functions of boundary inclination and misorienta-

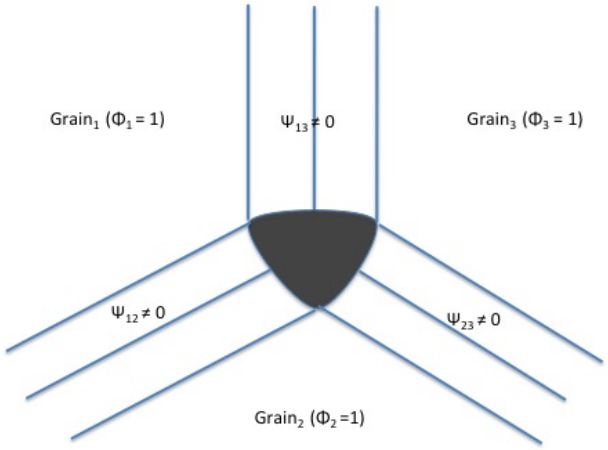

Figure 2.3: Interface fields defined at grain boundaries and triple junctions, with all three interface fields coexisting at junction cores.

tion, and eq.2.8 should then include higher derivatives. Details on how to include such terms can be seen in Appendix A.

The corresponding change in a phase-field variable is the mean of the changes of its associated interface fields

$$\phi_\alpha(t + \triangle t) - \phi_\alpha(t) = \frac{\sum_{\beta \neq \alpha} (\psi_{\alpha\beta}(t + \triangle t) - \psi_{\alpha\beta}(t))}{N} \tag{2.9}$$

Gradients (and laplacians) in phasefields are calculated as centered differences along the reference x, y (and z) axes (using an explicit finite difference scheme). A Forward Euler scheme is used to determine the phase field at time $t = t + \Delta t$, $\phi(t + \Delta t)$ if its value at the previous step $t = t$, $\phi(t)$ is known. Details can be found in Appendix B. The requisite conditions for stability will be discussed later. At the edges of the computational domain, a periodic boundary condition (PBC) is used - the neighbors of a point at the end lies on the opposite end (as in fig. 2.4).

2.2.2 Anisotropic boundaries and treatment of triple junctions

For anisotropic boundaries, the kinetic and potential energy coefficients in eqs.2.3,2.4 have to be modified. Assuming that the boundary energy is dependent on boundary inclination

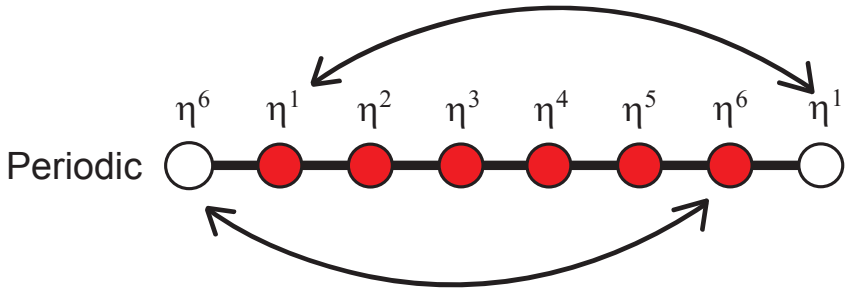

Figure 2.4: The neighbor of a point at the end of the domain lies on the opposite end.

θ (considering here the case of two dimensions) it can be given by

$$\gamma(\theta) = \gamma_0(1 + \delta cos(m'\theta)) \tag{2.10}$$

here γ_0, m' and δ represent the mean boundary energy, order of symmetry and degree of anisotropy respectively [28]. A similar form of spherical anisotropy was observed in two-dimensional experimental observations (cross-sections) of solidified droplets in Al-Cu and Al-Si systems by Napolitano et al. [47] .

The indices $[n_x, n_y]$ for the boundary normal in the sample frame can be obtained by averaging the gradients of the phase fields along standard directions (in this case along $\{100\}$ and $\{111\}$ in the sample reference frame), using the weighted essentially non-oscillatory (WENO) scheme [60, 59]. The motivation for choosing this particular scheme is its non-oscillatory behavior near sharp corners on boundaries, where there is a sudden change or jump of the boundary normal. In two dimensions, the inclination angle θ can be expressed in terms of gradients of the interface field $\psi_{\alpha\beta}$ (for a boundary where phase fields ϕ_α and ϕ_β intersect) along the reference axes (x and y) as in eq.2.14 [38]. Here, the boundary energy is expressed as a function of the boundary normal, and varies with the inclination angle θ that the boundary normal makes a reference axis.

$$\theta = atan\left(\frac{\psi_{\alpha\beta_y}}{\psi_{\alpha\beta_x}}\right) \tag{2.11}$$

The normal vector (obtained in the sample frame of reference) is then rotated in the crystal frame of reference of the grains on either side. In the present model the grain boundary energy between grains i and j is chosen as the mean of surface energy terms with respect to each grain (which is a reasonable assumption for ceramic systems [57]) as in eq.2.16, where each of the surface energy terms has a form identical to eq.2.10.

$$\gamma_{ij}(\theta) = \frac{\gamma(\theta_i) + \gamma(\theta_j)}{2} \tag{2.12}$$

This is analogous to the notion that when two crystals meet to make a boundary, the binding energy is fixed, and thus the grain boundary energy scales directly with the sum of the energies of the surfaces that bound the crystals on either side.

In three dimensions, the boundary energy γ can be expressed as a cubic-symmetric function dependent on the inclination angles (θ, φ) of the boundary normal $[n_x, n_y, n_z]$.

$$\gamma(\theta, \varphi) = \gamma_0 \left[1 + \delta \left(cos^4\theta + sin^4\theta \left\{1 - 2cos^2\varphi sin^2\varphi\right\}\right)\right] \tag{2.13}$$

here δ represents the degree of anisotropy that controls the relative values of energies along specific crystallographic directions (see fig.2.5). The inclination angles θ (between the projection of the normal to the plane of the paper and the reference x axis) and φ (between the boundary normal and the reference z axis) can be expressed in terms of gradients of the interface field $\psi_{\alpha\beta}$ (for a boundary where phase fields ϕ_α and ϕ_β intersect) along the reference axes (x, y and z) as in eqs.2.14,2.15

$$\theta = atan\left(\frac{\psi_{\alpha\beta_y}}{\psi_{\alpha\beta_x}}\right) \tag{2.14}$$

$$\varphi = acos\left(\psi_{\alpha\beta_z}\right) \tag{2.15}$$

and the grain boundary energy is expressed as the mean of the surface energy terms with respect to the grains on either side

$$\gamma_{ij}(n_x, n_y, n_z) = \frac{\gamma(n_x, n_y, n_z)_i + \gamma(n_x, n_y, n_z)_j}{2} \tag{2.16}$$

The interface width λ and boundary energy γ can be related to the gradient and potential energy coefficients in eqs. 2.3,2.4 as $\lambda \propto \sqrt{\frac{\varepsilon}{w}}$ and $\gamma \propto \sqrt{\varepsilon w}$ [34]. In order to maintain constant interface width irrespective of the boundary inclination (and independent of the boundary energy) one has to ensure that $\sqrt{\frac{\varepsilon}{w}}$ essentially remains constant while $\sqrt{\varepsilon w}$ varies with inclination. Hence both w and ε should have similar inclination dependence as the interface energy γ

$$w(\theta, \varphi) = w_o \left[1 + \delta \left(cos^4\theta + sin^4\theta \left\{1 - 2cos^2\varphi sin^2\varphi\right\}\right)\right] \tag{2.17}$$

and

$$\varepsilon(\theta, \varphi) = \varepsilon_o \left[1 + \delta \left(cos^4\theta + sin^4\theta \left\{1 - 2cos^2\varphi sin^2\varphi\right\}\right)\right] \tag{2.18}$$

In the present work, eq.2.8 is expressed as

$$\frac{\psi_{\alpha\beta}(t + \triangle t) - \psi_{\alpha\beta}(t)}{\triangle t} = \frac{1}{\tau} \sum (A\nabla^2\phi + B\phi) \tag{2.19}$$

A and B are similar to the gradient-energy coefficient ε and the potential energy maximum w respectively. Here they take the following exact form

$$A(\theta, \varphi) = \frac{4}{\pi^2}\kappa \left[1 + \delta \left(cos^4\theta + sin^4\theta \left\{1 - 2cos^2\varphi sin^2\varphi\right\}\right)\right] \tag{2.20}$$

$$B(\theta, \varphi) = \frac{4}{\kappa} \left[1 + \delta \left(cos^4\theta + sin^4\theta \left\{1 - 2cos^2\varphi sin^2\varphi\right\}\right)\right] \tag{2.21}$$

where κ scales with the boundary width λ that is chosen to be 8.0 in the present work. Since in eqs. 2.20,2.21 $\sqrt{\frac{A}{B}}$ is constant, the interface width λ is independent of the boundary

energy. In the present model, due to the absence of higher derivatives in the evolution equations, or sharp cusps in the boundary energy, a regularization scheme to prevent ill-posedness is not essential.

The boundary energy γ is rescaled (as in eq.2.22) so that the mean boundary energy is unity.

$$\gamma_{rescaled}(n_x, n_y, n_z) = \gamma_{rescaledmin} + (\gamma_{rescaledmax} - \gamma_{rescaledmin}) \left(\frac{\gamma(n_x, n_y, n_z) - \gamma_{min}}{\gamma_{max} - \gamma_{min}} \right) \quad (2.22)$$

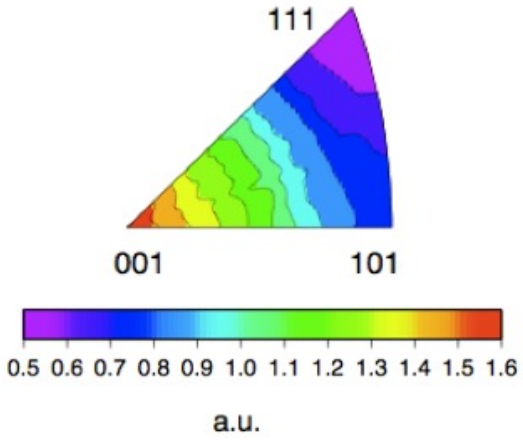

Figure 2.5: Variation of boundary energy with inclination, in three dimensions as in eq.2.13 with $\delta = 0.3$ and rescaled to $0.5 \leq \gamma \leq 1.5$.

In the method explained above, junction core energies (higher order terms in the energy functional when more than two fields overlap) can be neglected, given that interface width and size of junction cores is small compared to the length of boundaries and the overall domain size [21]. Recently the stability of solutions for dihedral angles at junctions was investigated by Guo et al [21]. The solutions were independent of boundary mobilities and depended only on the relative values of boundary energies. In other words, Young's law was satisfied at the boundary junctions. Also, junctions are assigned sufficiently high mobilities, and do not *drag* moving boundaries [16, 15] - hence junction kinetics do not control microstructure evolution.

At the boundary junction phase-field profiles deviate from the actual grain boundary

(see fig. 2.6) - hence normals estimated at junctions using phase field values (and their gradients) are inherently inaccurate. Methods to incorporate these approximate normals in the evolution equations introduce oscillations in the phase-field values at the triple junctions, which eventually spread throughout the entire domain. To prevent such instabilities, it is essential to explicitly assign energies to interface fields at triple junctions based on the procedure described below. It is to be noted that either equal energies can be associated with these fields (case-I) or anisotropic energies can be extended along grain boundaries (case-II).

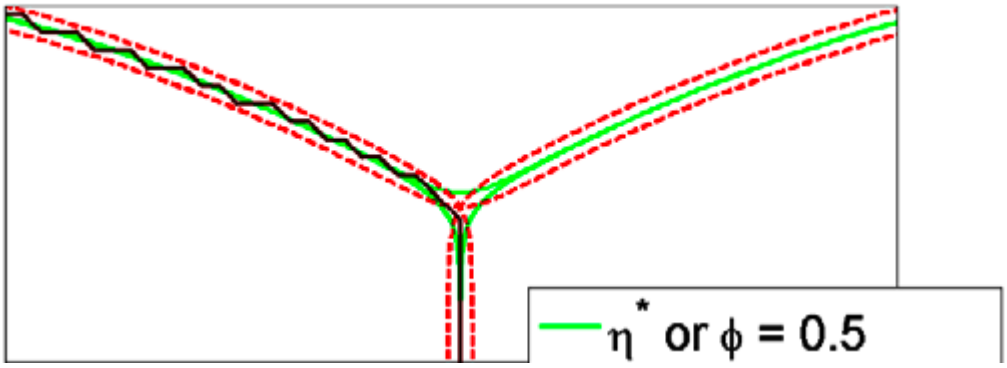

Figure 2.6: At the triple junction, the contour lines (say for $\phi = 0.5$ labeled green, and for $\phi = 0.3$ labeled red) deviate from the sctual grain boundary (derived from a sharp interface approximation, labeled black). Figure reproduced from [42].

In case-I, the energies of grain boundaries is anisotropic (the form of the energy function is similar to to eq.2.13 in three dimensions), while the energies associated with the interface fields at junctions is explicitly isotropic, which implies that boundaries are constrained to meet at equal angles. In case-II, an energy extension method is used (see fig. 2.7) which ensures that anisotropic energies are extended along grain boundaries and associated with the interface fields $\psi_{01}, \psi_{02}, \psi_{12}$ (with the phase fields ordered as $\phi_0 > \varphi_1 > \varphi_2$). The percolation of energies to the boundary junctions is implemented in the following manner - for each point in a multiphase region (having N, the number of non-zero fields, greater than two) a value equivalent to the average of non-zero neighboring energies is stored. This

process is continued until all points in the junction region have non-zero energies.

In case of triple junctions, the corresponding equations of motion for the phase-fields (ϕ_1, ϕ_2, ϕ_3 ordered as $\phi_1 > \phi_2 > \phi_3$) can be expressed as (refer [63, 21])

$$\begin{aligned}\frac{\partial \phi_1}{\partial t} &= -\tau_{12}\left(\varepsilon_{12}\left[c_1\nabla^2\phi_2 + c_2\phi_2\right] + \varepsilon_{13}\left[c_1\nabla^2\phi_3 + c_2\phi_3\right] - \varepsilon_{12}\left[c_1\nabla^2\phi_1 + c_2\phi_1\right] - \varepsilon_{23}\left[c_1\nabla^2\phi_3 + c_2\phi_3\right]\right) \\ &\quad -\tau_{13}\left(\varepsilon_{12}\left[c_1\nabla^2\phi_2 + c_2\phi_2\right] + \varepsilon_{13}\left[c_1\nabla^2\phi_3 + c_2\phi_3\right] - \varepsilon_{13}\left[c_1\nabla^2\phi_1 + c_2\phi_1\right] - \varepsilon_{23}\left[c_1\nabla^2\phi_2 + c_2\phi_2\right]\right)\end{aligned}$$

$$\begin{aligned}\frac{\partial \phi_2}{\partial t} &= \tau_{12}\left(\varepsilon_{12}\left[c_1\nabla^2\phi_2 + c_2\phi_2\right] + \varepsilon_{13}\left[c_1\nabla^2\phi_3 + c_2\phi_3\right] - \varepsilon_{12}\left[c_1\nabla^2\phi_1 + c_2\phi_1\right] - \varepsilon_{23}\left[c_1\nabla^2\phi_3 + c_2\phi_3\right]\right) \\ &\quad -\tau_{23}\left(\varepsilon_{12}\left[c_1\nabla^2\phi_1 + c_2\phi_1\right] + \varepsilon_{23}\left[c_1\nabla^2\phi_3 + c_2\phi_3\right] - \varepsilon_{13}\left[c_1\nabla^2\phi_1 + c_2\phi_1\right] - \varepsilon_{23}\left[c_1\nabla^2\phi_2 + c_2\phi_2\right]\right)\end{aligned}$$

$$\begin{aligned}\frac{\partial \phi_3}{\partial t} &= \tau_{13}\left(\varepsilon_{12}\left[c_1\nabla^2\phi_2 + c_2\phi_2\right] + \varepsilon_{13}\left[c_1\nabla^2\phi_3 + c_2\phi_3\right] - \varepsilon_{13}\left[c_1\nabla^2\phi_1 + c_2\phi_1\right] - \varepsilon_{23}\left[c_1\nabla^2\phi_2 + c_2\phi_2\right]\right) \\ &\quad +\tau_{23}\left(\varepsilon_{12}\left[c_1\nabla^2\phi_1 + c_2\phi_1\right] + \varepsilon_{23}\left[c_1\nabla^2\phi_3 + c_2\phi_3\right] - \varepsilon_{13}\left[c_1\nabla^2\phi_1 + c_2\phi_1\right] - \varepsilon_{23}\left[c_1\nabla^2\phi_2 + c_2\phi_2\right]\right)\end{aligned}$$

c_1 and c_2 denote the $(\frac{4w}{\pi^2})$ and $(\frac{4}{w})$ prefactors respectively. In case-I (isotropic junctions) the energy coefficients ε_{ij} are fixed as unity whereas in case-II anisotropic energies are extended along boundaries to junctions such that ε_{ij} assume anisotropic values. Details for the percolation of anisotropic energies (which are dependent on boundary inclination in the crystal frame of reference at grain boundaries) to junctions is discussed in Appendix D. If an energy value equivalent to zero is assigned ($\varepsilon_{ij} = 0$) then the junctions become static (or fixed). Hence, either equal energies ($\varepsilon_{ij} = 1.0$ as in case-I) or anisotropic energies ($\varepsilon_{ij} \neq 1.0$ as in case-II) have to be associated with the interface fields in boundary junctions. This does not neccesitate assigning an orientation or normal to points in boundary junctions as energies are explicitly asssigned here.

The assumption that should be noted is that boundary segments at junctions should be sufficiently straight. The junctions in the aforementioned cases will be referred to as isotropic junctions (case-I) and anisotropic junctions (case-II) respectively. Also it should be noted that for simplicity, torque terms which occur due to inclination-dependence of energy are not accounted for in the present model. Hence, Herring's relations for mechanical balance at boundary junctions for inclination-dependent boundary energies will reduce to Young's equations for balance of line energies. Any difference in inclination distributions in cases I and II should be a natural consequence of satisfying Young's law at boundary junctions.

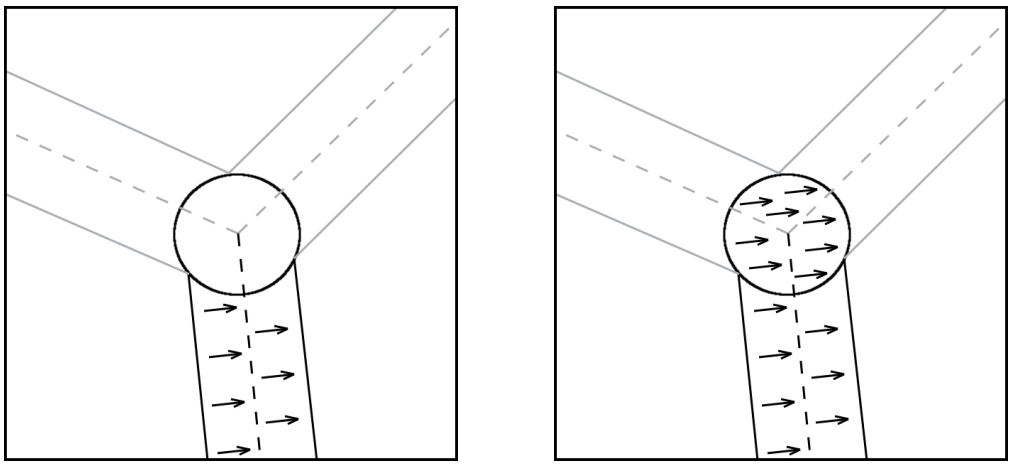

Figure 2.7: (a) Without energy extension all energies in junction cores are identical to 1.0 (b) energy extension along grain boundaries such that anisotropic boundary energies are extended to junctions.

2.3 Model validation and parameter estimation

2.3.1 Effect of changing timestep - stability criteria for forward differencing scheme

Since an explicit forward difference scheme is used the phasefield values at timestep $t = t+\Delta t$ using values at a previous timestep $t = t$, the ratio of timestep $\triangle t$ to $(\Delta x)^p$ (where $\triangle x$ is the discretization stepsize in space) should be less than some constant c using the *Courant-*

Friedrichs-Lewy condition. This condition states that [71, 10]

" the time step must be kept small enough so that information has enough time to propagate through the space discretization...."

which can be expressed as $\frac{v\triangle t}{(\triangle x)^p} \leq c$, where v is a measure of propagation velocity of information. For a Forward-Time Central-Space (FTCS) scheme (using Forward Euler in time and centered differences in space) the exponent p takes the value of 2.

Using different values of timestep $\triangle t$ and gridstep $\triangle x$ we find that the dimensionless constant c takes the value of 0.02 (empirically determined). The CFL condition for stability for the isotropic case (all boundaries having equal velocities) is reduced to

$$\frac{\triangle t}{(\triangle x)^2} \leq 0.02 \tag{2.23}$$

In the anisotropic case, since the interface velocity v scales with boundary mobility m and energy γ as in eq.1.1, this criteria can be modified as

$$m_{max}\gamma_{max}\frac{\triangle t}{(\triangle x)^2} \leq 0.02 \tag{2.24}$$

In the present set of simulatons we use $\Delta x = 1$, hence in the isotropic case, a maximum value of 0.02 can be chosen for Δt. In the following figure (see fig.2.8) we show the evolution of boundaries (in a 128^2 grid having 16 grains) using different values of Δt. In phasefield simulations, a single timestep is said to have occured when all grid points have been considered for update once. Here for each timestep Δt chosen ($\Delta t = 0.01, 0.02, ...$) we update the entire grid N times, where N is chosen such that the effective total time evolved in all cases is T

$$N\Delta t = T \tag{2.25}$$

For values of Δt greater than 0.04, instabilities grow with time and spread through the computational domain. Hence, we choose a value of $\triangle t = 0.02$ in the simulations presented

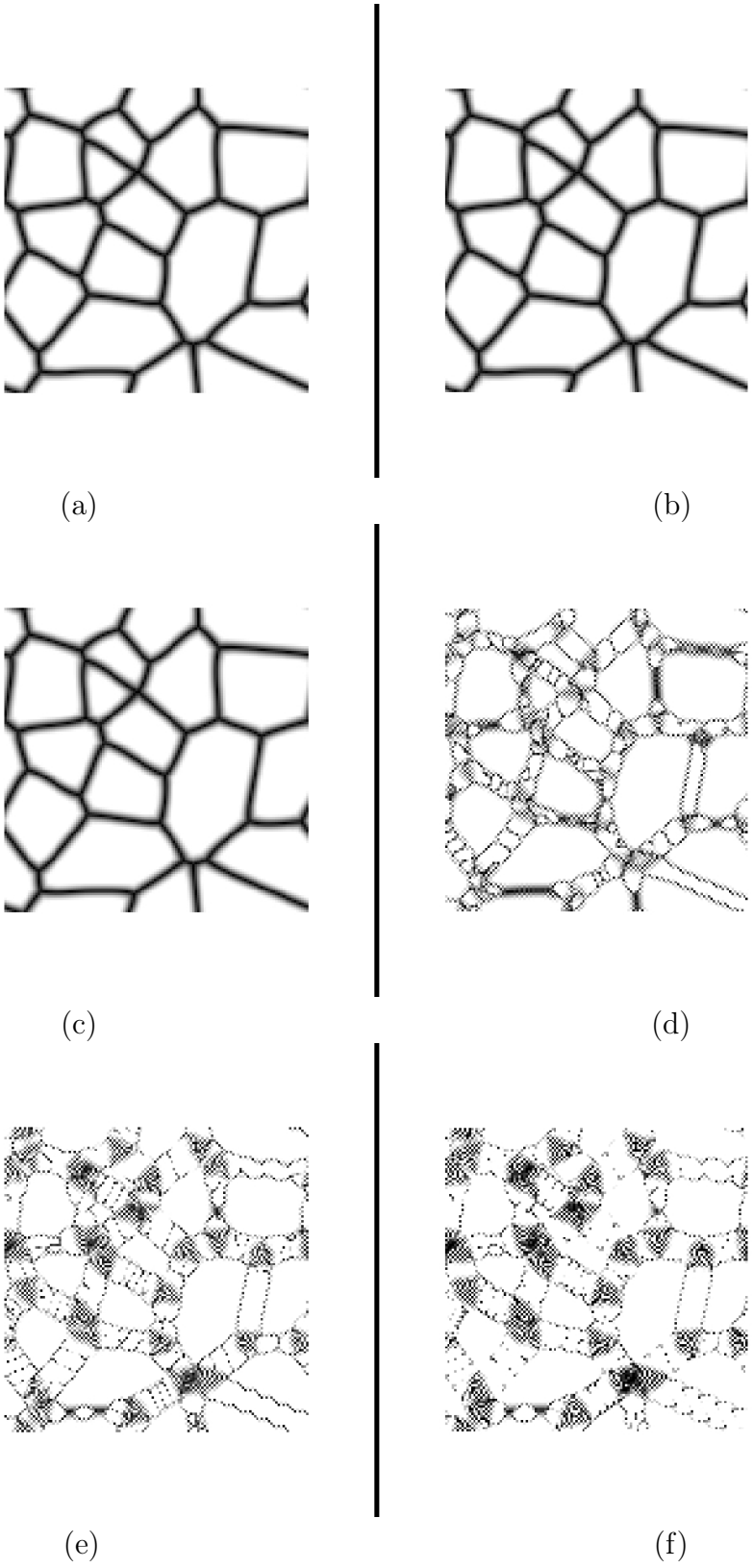

Figure 2.8: Evolution of GBs for timestep Δt chosen to be (a) 0.01 (b) 0.02 (c) 0.04 (d) 0.06 (e) 0.08 and (f) 0.10. The boundaries remain stable for Δt smaller than 0.06.

here. A lesser value satisfies numerical stability but we will need larger values of N (number of evolution timesteps) to move the boundary an indentical distance.

2.3.2 Effect of changing boundary width - isotropic shrinkage of an occluded grain

In the present section we explore the effect of changing the boundary width to grid stepsize ratio (that is $\lambda/\Delta x$) on the kinetics of a shrinking grain (in two dimensions). In other words we vary the number of points we use to represent the boundary. The motivation is we have an analytical solution that we can use, and we can compare our results to previous work by Moelans *et al.* [39, 42]to validate the interface field approach.

In the following figure (fig. 2.9) we show the variation of rate of change in grain area with the grain radius (normalised by the boundary thickness). To calulate the grain area we include all voxels having $\phi_1 = 1$ (where the circular occluded grain is indexed 1 and the surrounding grain indexed as 2). At the interface region ($0 \leq \phi_1, \phi_2 \leq 1$ for $0 \leq x \leq 1$) we sum up the quantity $\phi_1(x)$ over all interface points and add this to get a better estimate of grain area $A_1(t)$. Analytically, in the isotropic case the change in grain area with time is linear (see eq. 2.26) and should be independent of the grain radius $R_1(t)$. The grain radius $R_1(t)$ is estimated as the radius of the equivalent circle having an area $A_1(t)$.

$$A_1(t) - A_1(0) = 2\pi m\gamma t \tag{2.26}$$

$\frac{dA}{dt}$ remains independent of $\frac{R}{\lambda}$ till the grain shrinks to a radius R which is about the same order as the boundary thickness λ. After this point a sharp-interface approximation no longer holds true. Also for boundary thicknesses λ lesser than 4 times the grid stepsize $\triangle x$ the deviation is evident. We also show (in fig.2.10) the variation of the velocity (normalised by the mean curvature k) with the grain radius R (normalised by the boundary thickness λ). The mean curvature is computed as the divergence of the boundary normal ($k = \bigtriangledown.\hat{n}$)

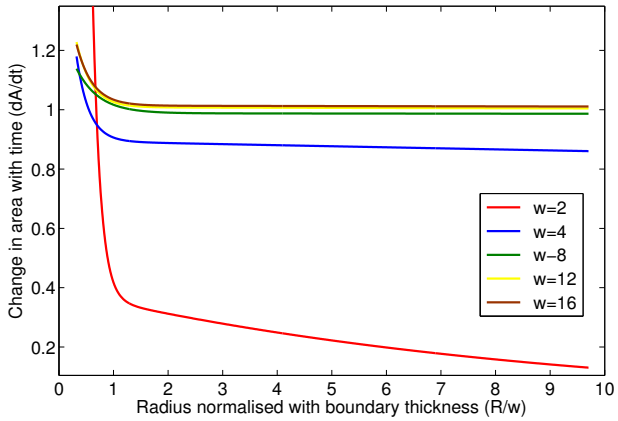

(a)

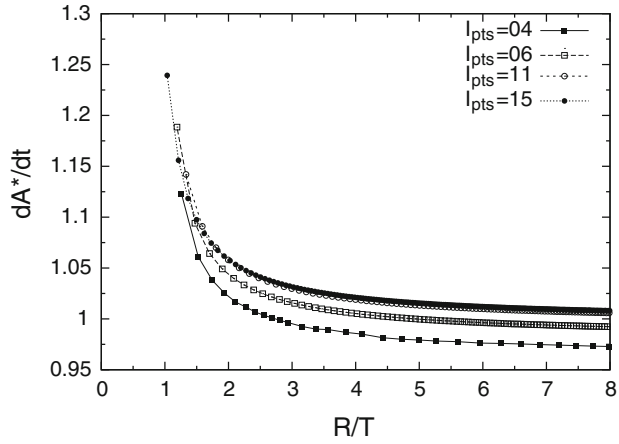

(b)

Figure 2.9: (a) Variation of rate of change of area with the grain radius. For a boundary width (normalised by the grid stepsize $\triangle x$) smaller than 4 we see a deviation from the expected variation (which is a straight line at unity for the isotropic case). (b) Figure reproduced from McKenna *et al. [39]*

and the boundary velocity is estimated as the change in grain radius with time ($v(t) = \frac{R_1(t)-R_1(t-N\triangle t)}{N\triangle t}$) averaged over 100 timesteps. In the isotropic case ($\mu = 1, \gamma = 1$) the expected variation is a straight line at unity. For $R \leq 4\lambda$ a large deviation is seen which suggests that in polycrystalline simulations we should use a grain radius $R > 4\lambda$.

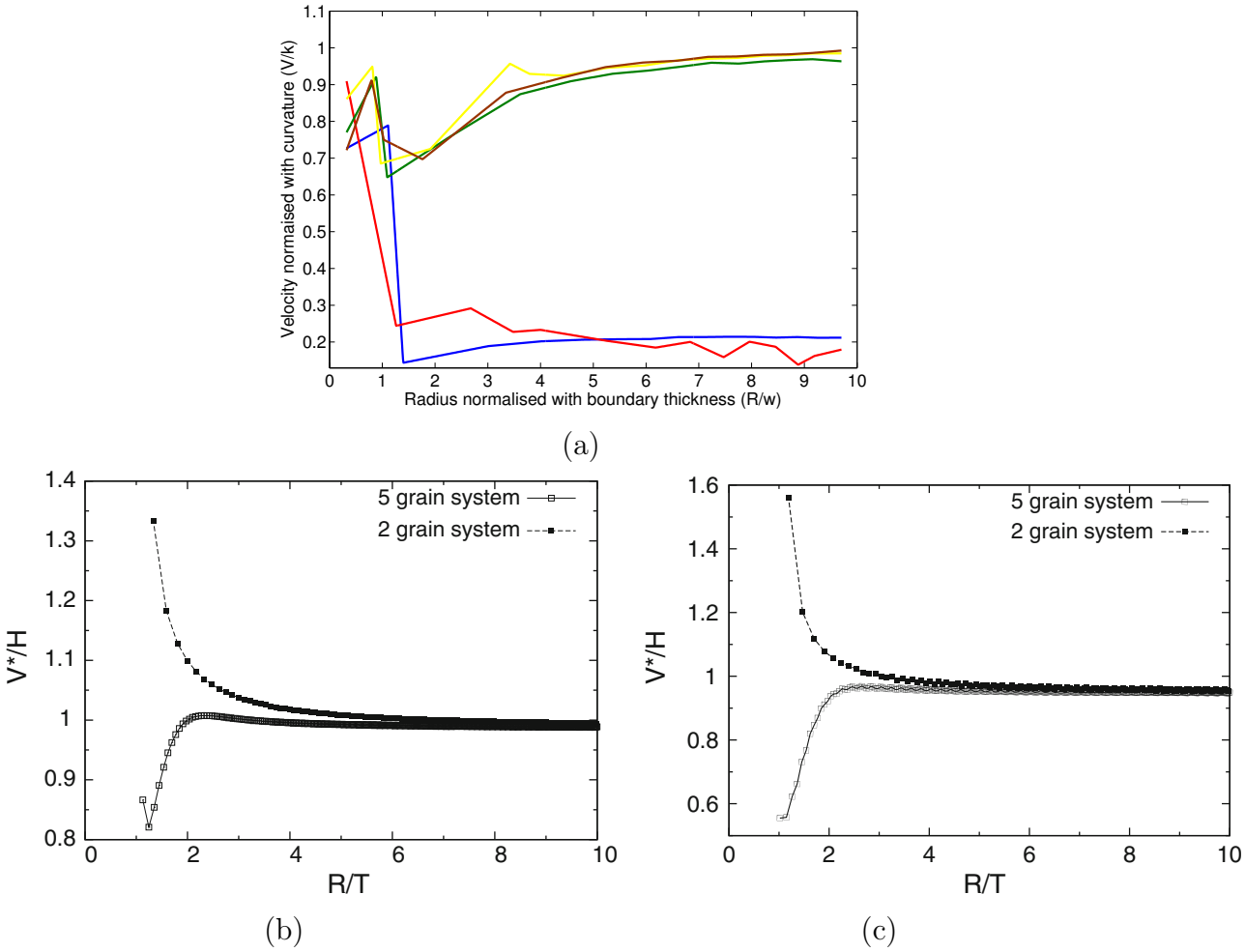

Figure 2.10: (a) Variation of boundary velocity (normalised by mean curvature) with the grain radius (normalised by boundary thickness). Figue reproduced from McKenna *et al.* [39]for an interface width of (b) 6 and (c) 11. Compare the profiles for the 2-grain systems in (b,c) to (a).

In fig. 2.11 we show the grain shape when $R_1(t) = 8\lambda$ for different values of the boundary thickness ($\lambda = 2, 4, 6, ...$ times $\triangle x$). For $\lambda < 4 \triangle x$ the grain does not maintain its circular shape while shrinking and develops facets. Since the boundary is resolved by insufficient points, lattice anisotropy effects result in preferential selection of certain crystal directions

($< 10 >$and $< 11 >$ directions for a square grid in two dimensions) and faceting. To minimize such effects the boundary should be reolved by at least 4 points.

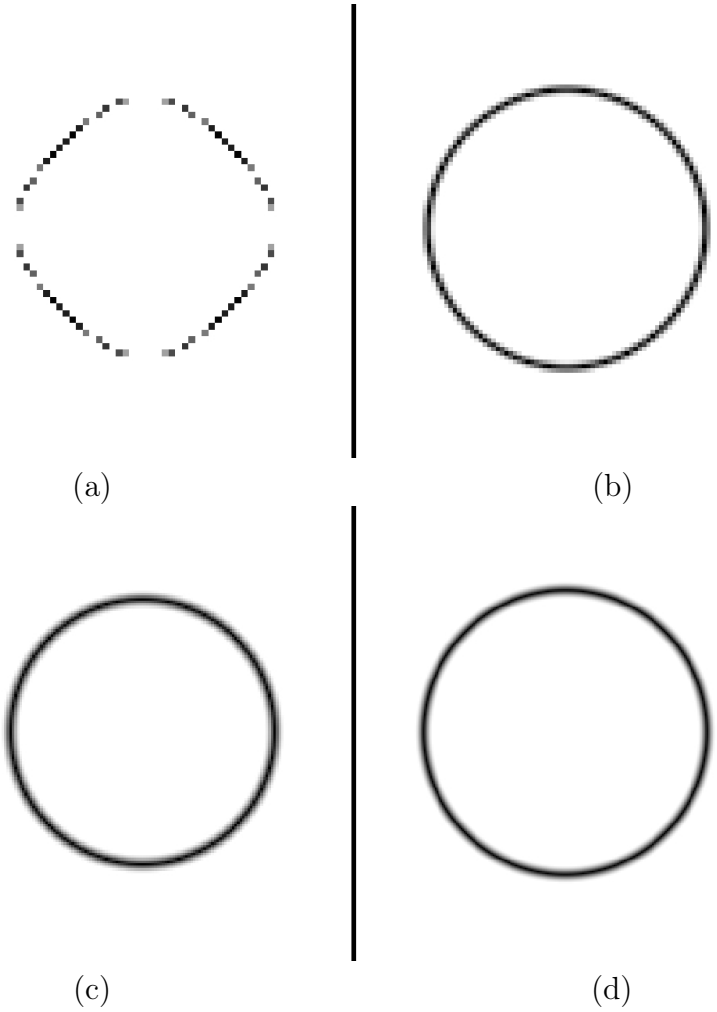

Figure 2.11: Grain shapes when $R = 8\lambda$, for $\frac{\lambda}{\triangle x}$ having a value of (a) 2 (b) 4 (c) 8 and (d) 12. See that the grain retains its circular shape while shrinking for $\lambda \geq 4 \triangle x$.

From these simulations we can choose the values of the model parameters as follows

1. The grid stepsize $\triangle x$ is taken to be 1, which would mean a timestep $\triangle t = 0.02$. A smaller stepsize will demand a corresponding smaller timestep for numerical stability (as in eq.2.23 $\triangle t \leq 0.02 \left(\triangle x\right)^2$).

2. The interface should contain at least four gridpoints, $\lambda \geq 4 \triangle x$ to avoid effects of lattice anisotropy. We choose a value of $\lambda = 8 \triangle x$. A larger value is not chosen to

reduce computational time.

3. The initial grain radius $R(0)$ in polycrystalline simulations should be at least 4 times the interface thickness λ, such that the model produces expected grain-growth kinetics. For a chosen $\lambda = 8 \triangle x$, this suggests an initial grain radius $R(0) = 32 \triangle x$. A finer resolution of the interface (that is when $\lambda > 8 \triangle x$) would increase this value, resulting in lesser number of grains which can be accomodated in the computational domain.

2.3.3 Effects of boundary width and boundary conditions (imposed at junctions) on steady-state dihedral angles

In fig. 2.13 we investigate the effect of different boundary conditions imposed at junctions on steady-state dihedral angles. The ratio of boundary energies $r = \frac{\gamma_{jk}}{2\gamma_{1j}}$ is varied and the dihedral angle θ is measured manually between line profiles of phase field ϕ_0 (phase fields ϕ_0, ϕ_1 at boundaries are ordered as $\phi_0 > \phi_1$) for the value $\phi_0 = 0.5$. Since at the triple-junction the contour line for $\phi_0 = 0.5$ deviates from the actual GB (as in fig. 2.6) points within the triple junction region are omitted, and boundaries are assumed to be sufficiently straight till they meet at the junction. In case-I energies associated with the interface fields $\psi_{01}, \psi_{02}, \psi_{12}$ at junctions (with the phase fields ordered as $\phi_0 > \varphi_1 > \varphi_2$) are taken to be unity, whereas in case-II anisotropic energies permeate along GBs using the energy-extension method (as in fig. 2.7). The uncertainty in measrement is seen to be approximately 4° and increases as θ decreases (or r increases). For case-I, dihedral angles are expected to be identical to 120°, in contrast to case-II, where these should vary with relative boundary energies γ_{ij}, and can be derived to be identical to $2cos^{-1}\left(\frac{\gamma_{jk,j,k\neq 1}}{2\gamma_{1j,j\neq 1}}\right)$ using eq.1.2. In fig. 2.12the intermediate grain structure is shown for a model 4-grain structure for case-I (junctions refered as *isotropic*) and case-II (junctions refered as *anisotropic*).

The effect of boundary width λ on the steady-state dihedral angle θ is also explored (see fig. 2.14). It is difficult to measure dihedral angles for widths $\lambda > 8 \triangle x$, more so for sharp

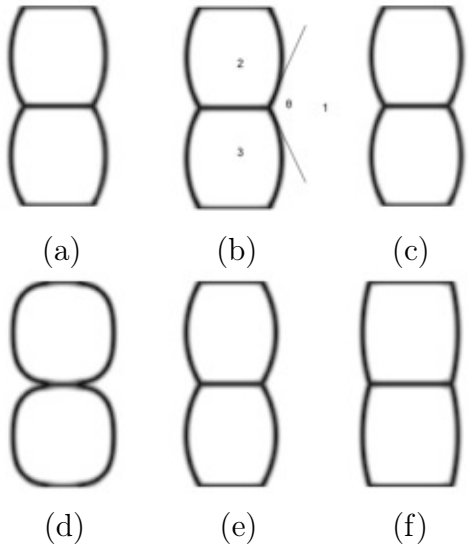

Figure 2.12: Intermediate grain structure for a model 4-grain structure evolved with a misorientation-based boundary energy, with the ratio of line energies defined as $r = \left(\frac{\gamma_{jk,j,k\neq 1}}{2\gamma_{1j,j\neq 1}}\right)$. In figs. (a-c) junctions are treated as *isotropic* (case-I) with the ratio of line energies varying as (a) $r = 0.5$, (b) $r = 1.0$ and (c) $r = 2.0$. In figs. (d-f) junstions are treated as *anisotropic* (case-II) with (d) $r = 0.25$ (fully wetting) , (e) $r = 0.50$ (isotropic) and (f) $r = 1.0$ (non-wetting). Note that in case-I dihedral angles are close to 120° irrespective of the ratio of line energies, whereas in case-II they vary with the ratio of boundary energies.

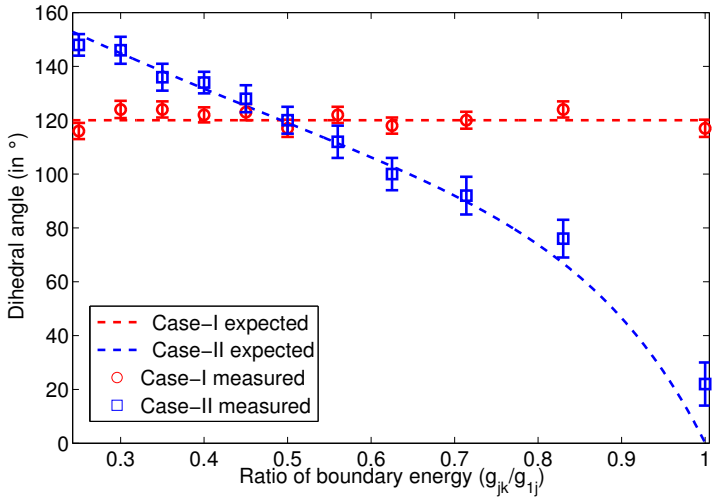

Figure 2.13: Variation of dihedral angle θ (as in fig. 2.12) with relative boundary energies $r = \left(\frac{\gamma_{jk}}{2\gamma_{1j}}\right)$. Note that for case-I a value of 120° is expected, compared to case-II where the expected dihedral angle is given by $\theta = 2cos^{-1}\left(\frac{\gamma_{jk}}{2\gamma_{1j}}\right)$. The dihedral angles are measured manually between line profiles of phase field ϕ_0 (phase fields ϕ_0, ϕ_1 at boundaries are ordered as $\phi_0 > \phi_1$) for the value $\phi_0 = 0.5$, and the measurement uncertainty is approximately 4°.

cusps and small values of θ (or large values of r). The deviation from the expected dihedral angle also increases as the boundary width decreases below $4 \triangle x$ as the boundary is resolved by insufficient number of points.

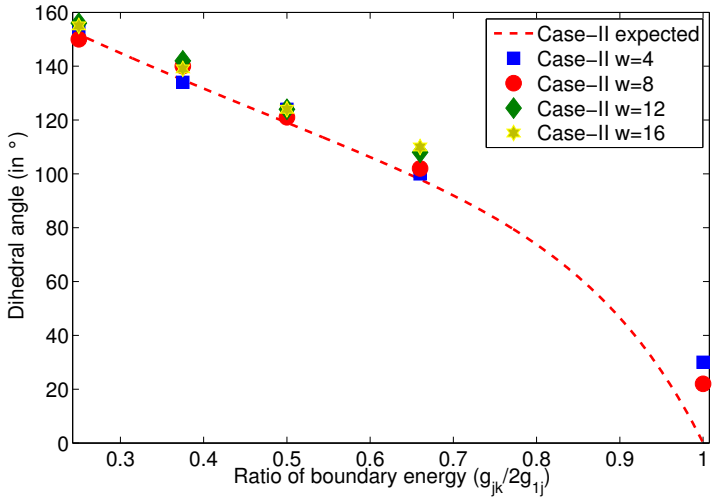

Figure 2.14: Variation of dihedral angles with relative boundary energies $r = \left(\frac{\gamma_{jk}}{2\gamma_{1j}}\right)$ for different boundary widths ($\frac{\lambda}{\triangle x} = 4, 8, ...$). when junctions are treated as anisotropic (Case-II).

Part II

- Results and discussion

2.4 Simulation parameters

From the simulations presented in Part-I we showed that the criteria for numerical stability and computational efficiency support the use of the following values for the model parameters (taking a grid stepsize $\triangle x = 1$)

1. timestep $\triangle t = 0.02$. This scales with $(\triangle x)^2$, so smaller gridsteps correspond to smaller timesteps.

2. boundary width $\lambda = 8 \triangle x$. Smaller widths suffer from effects of lattice anisotropy and larger widths need more computational resources with no additional benefits of increased resolution.

3. Initial grainsize $R = 4\lambda$. When the grain size shrinks to a size comparable to the boundary thickness, kinetics deviate from those dictated by curvature-driven growth. Hence a sharp-interface approximation of the diffused boundary holds true for $R \geq 4\lambda$. Larger grainsizes can be used but this will restrict the number of grains that can be accomodated in the computational doamin. Since we need a large number of boundaries for reliable statistics, we do not use an initial grainsize much larger than 4λ in the polycrystalline simulations.

2.5 Results and discussion

2.5.1 Steady state shrinkage of isolated grains

A 128-squared domain (in two dimensions) was used to look at the evolution of isolated grains shrinking with anisotropic boundary energy γ. The orientation of isolated grain is denoted by $< \frac{\theta_1}{2}, 0, 0 >$ with respect to the orientation of the surrounding grain, which can be denoted as $< -\frac{\theta_1}{2}, 0, 0 >$. In this case, the boundary normal in the crystal frame is constrained to lie in the plane of the paper, and the boundary energy can be expressed as

a function of the inclination θ that the boundary normal makes with a reference axis, say $< 100 >$ (as in eq.1.11). Grains are misoriented with respect to each other if they are rotated by varying amounts about the plane normal $< 001 >$. The value of δ was varied from 0 (isotropic) to 0.4 (strongly anisotropic) in increments of 0.1, and the symmetry of the energy function was assumed to be four-fold ($m' = 4$). The boundary mobility m was assumed to be isotropic. The deviation of steady-state grain shapes from the circular shape can be seen in fig. 2.15. It can be seen that grains become more faceted (see deviation from the circular shape denoted by the dotted line) as the strength of anisotropy increases.

Since the grain boundary energy is expressed as the sum of the surface energies of grains on either side of the boundary, as in eq.2.16, the boundary normal in the sample frame has to be rotated in the frame of reference of either grain. Hence, the inclination-based energy is implicitly dependent on the misorientation across the boundary (see fig.2.17(b)) . To investigate the effect of misorientation on inclination distributions the value of θ was varied at fixed intervals of 9°, and the anisotropy strength δ in eq.2.10 was fixed at 0.4. The effect of increasing misorientation across the boundary on grain shapes can be seen in fig. 2.16. The corresponding inclination distributions are shown in fig. 2.17(a). As the misorientation across the boundary increases, grains assume shapes which are increasingly less faceted (see fig. 2.16). The deviation from the circular shape (represented by the dotted line) decreases as the boundary misorientation increases. This is because the grain boundary energy (expressed as the sum of surface energy terms for grains on either side. where these surface energies depend on boundary inclination in the crystal frame of reference) becomes less anisotropic as misorientation increases.

In three dimensions, a 64-cubed domain was used to look at the shrinkage of an isolated grain with anisotropic boundary energy γ expressed as in eq.2.13, varying the anisotropy strength δ from 0 (isotropic) to 0.3 (strongly anisotropic). The boundary mobility is assumed to be isotropic ($m = 1$). The boundary velocity scales with the product of boundary energy and mobility (as $v = m\gamma k$), hence it has an anisotropic form as in fig.2.5 (*low-energy*

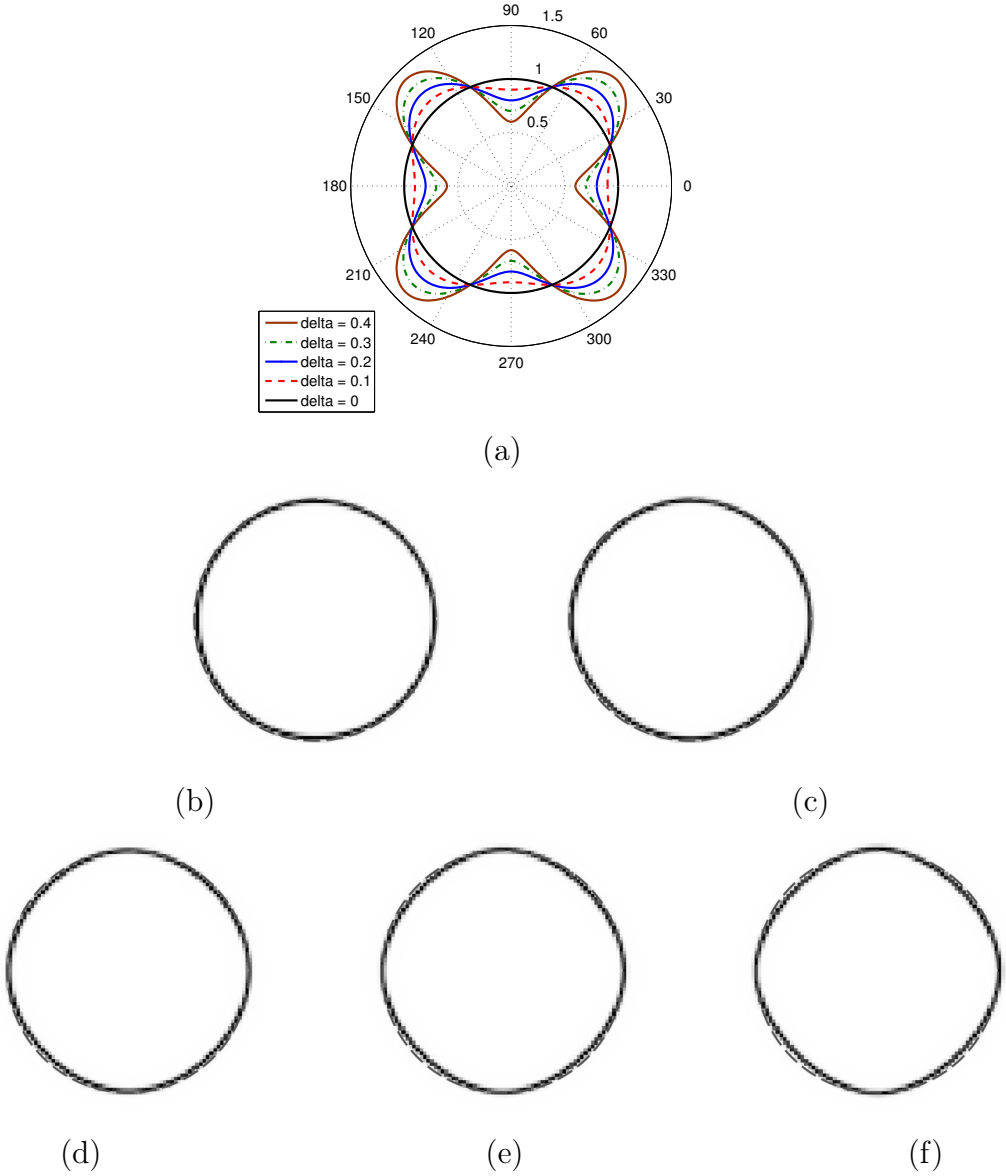

Figure 2.15: (a) Inclination-based boundary energy with a maximum value for inclinations at 45°; steady state kinetic shapes of shrinking grains at intermediate $t = 2000$ steps, with increasing strength of anisotropy δ (b) 0 (isotropic) (c) 0.1 (d) 0.2 (e) 0.3 (f) 0.4. Boundaries are color coded black. Note that grain shapes become faceted as the strength of anisotropy increases. A circular shape is also shown (dotted line) for comparison. Simulations are performed in two dimensions on a 128-squared domain.

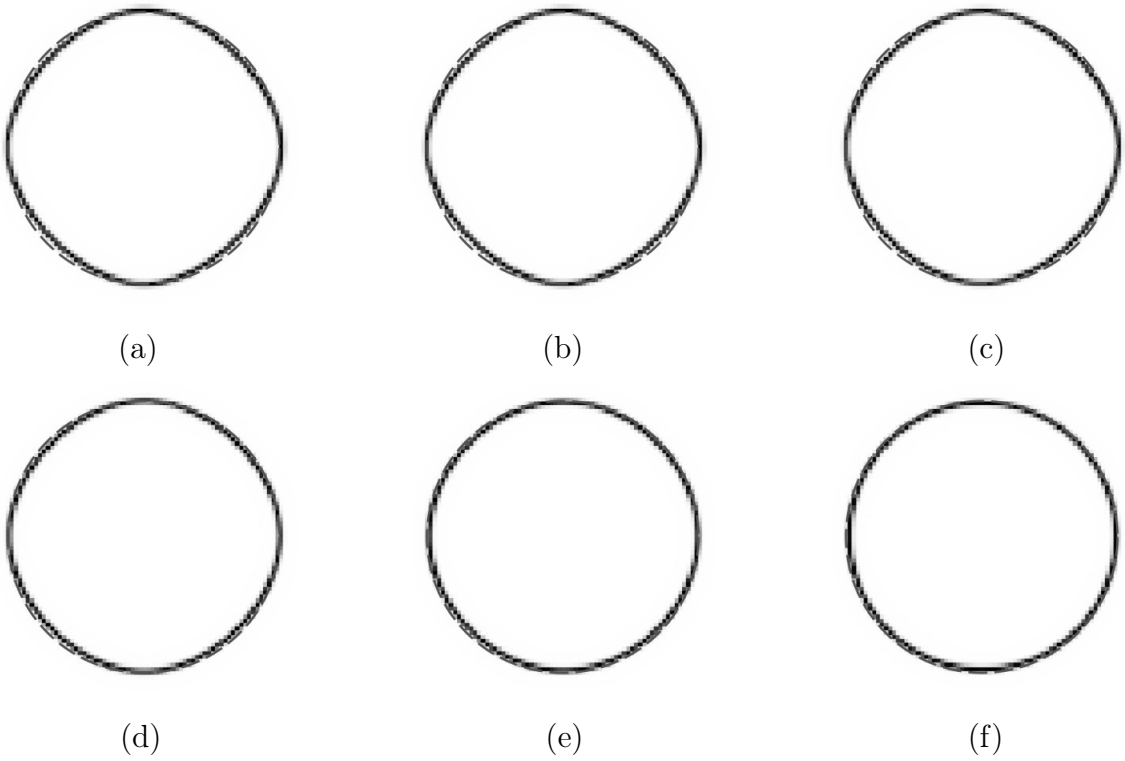

Figure 2.16: Kinetic shapes of shrinking grains with increasing misorientation across the boundary, the specific misorientations shown are (a) 0° (b) 9° (c) 18° (d) 27° (e) 36° and (f) 45°. A circular shape is also shown (dotted line) for comparison. Note that as the misorientation across the boundary increases, the steady-state grain shape becomes more circular. Simulations are performed in two dimensions on a 128-squared domain, and evolved for $t = 2000$ steps.

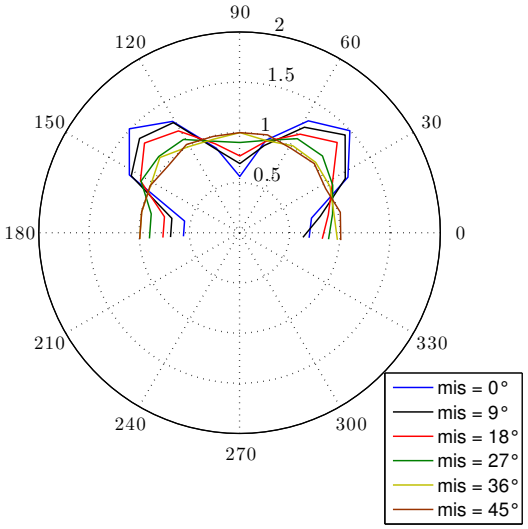

(a)

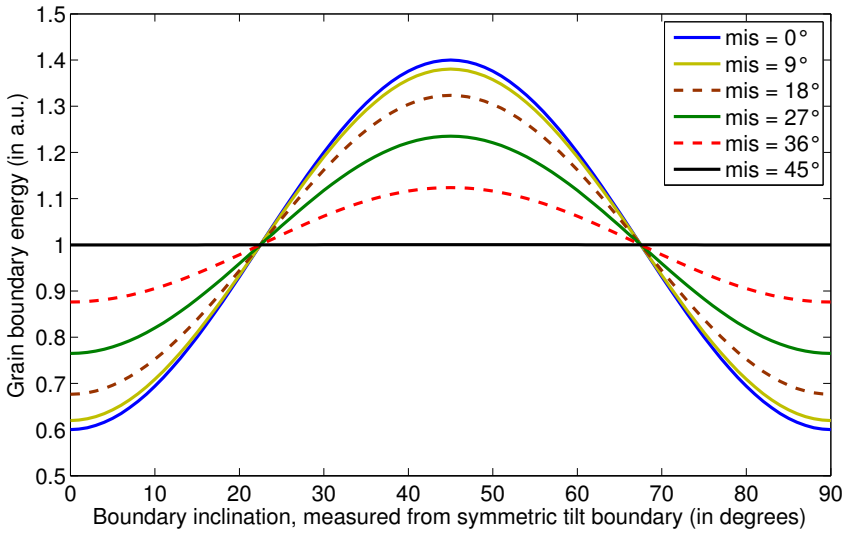

(b)

Figure 2.17: Inclination distributions (in a.u.) of isolated grains with varying misorientation, the boundary energy used has a form identical to fig.2.15 (a) with anisotropy strength $\delta = 0.4$. Simulations are performed in two dimensions. Note that the populations scale directly with interfacial energy (compare a(top) to b(bottom)), by contrast to the polycrystalline results shown later. Fig. b(bottom) shows the effect that boundary misorientation has on an inclination-based boundary energy, as the boundary energy is expressed as the mean of surface energy terms with respect to the grains on either side of the boundary (see eq.2.16). As boundary misorientation increases, the variation of an inclination-based boundary energy decreases (see fig.b (bottom), and inclination distributions become more uniform as in fig.a (top).

boundaries have *low velocity* and vice-versa). Shrinking from a spherical shape, the grain shapes at $t = 4000$ are shown in fig. 2.18 and the corresponding boundary populations are plotted in fig. 2.19 as inverse pole figures. As the strength of anisotropy increases, shrinking grains develop facets and boundary populations and energies scale with each other. Note that in this case, grains are shrinking and the grain volume is not conserved. If an additional constraint of constant volume is enforced, isolated grains are bounded by low-velocity interfaces and an inverse relation between boundary population and velocity is to be expected [13, 5].

Expected grain shapes can be derived in three dimensions using a procedure identical to Sekerka et al. [58]. For the particular anisotropic functions used in the present formulation (eq. 2.13 for three dimensions), the corresponding kinetic Wulff plots are shown below (see fig. 2.20). Parametric expressions for expected kinetic shapes were derived from reference [37]. As the strength of anisotropy increases, *ears* appear on the ξ-plot (in three dimensions), which have to be discarded, and the remaining convex body gives the expected kinetic shape [5, 6, 67]. These forms are bounded by low-velocity boundaries as they correspond to crystals *growing* under a condition of anisotropic boundary kinetics [67], in contrast to the present case, where grains are *shrinking.* Growth shapes are expected to be bounded by low-velocity boundaries, as they remain while high velocity boundaries *grow out* and disappear. Shrinking grains on the other hand, are bounded by fast moving boundaries which *shrink in* and eliminate slower boundaries.

In fig. 2.21(a) the expected variation of boundary population (in *multiples of random distribution MRD*) with boundary energy (in *a.u.*) is shown (the boundary energy γ has a form as in eq.2.13 with $\delta = 0.3$ and γ_{max} rescaled to 1.0) - for growing grains an inverse relation between boundary population and energy is seen in contrast to shrinking grains where these scale with each other. In fig. 2.21(b) this variation (extracted from the *two-grain* simulations) is plotted for the case of shrinking grains, for increasing values of the anisotropy strength δ. As the anisotropy strength increases, high velocity boundaries shrink

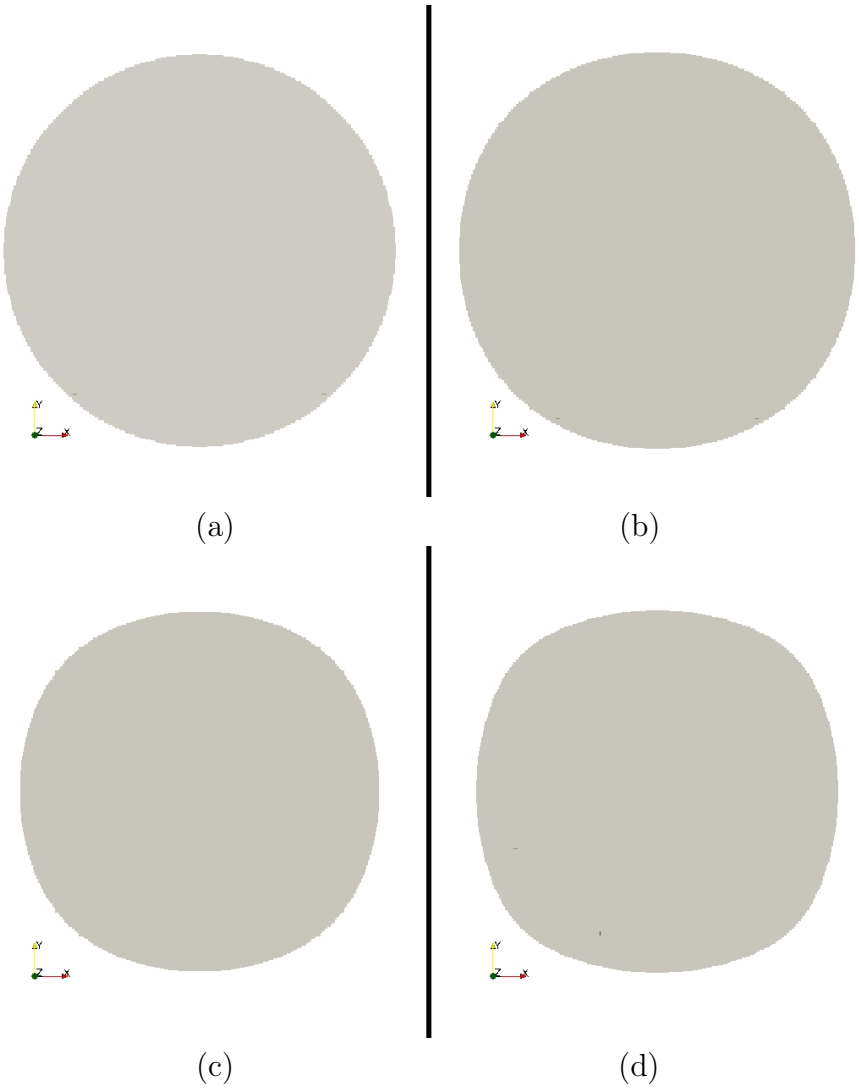

Figure 2.18: Grain shapes at $t = 4000$ for boundary energy varying as in eq.2.13 with increasing anisotropy strength δ varying as (a) 0 (b) 0.1 (c) 0.2 and (d) 0.3. As anisotropy increases grain shapes deviate from the spherical shape and develop facets.

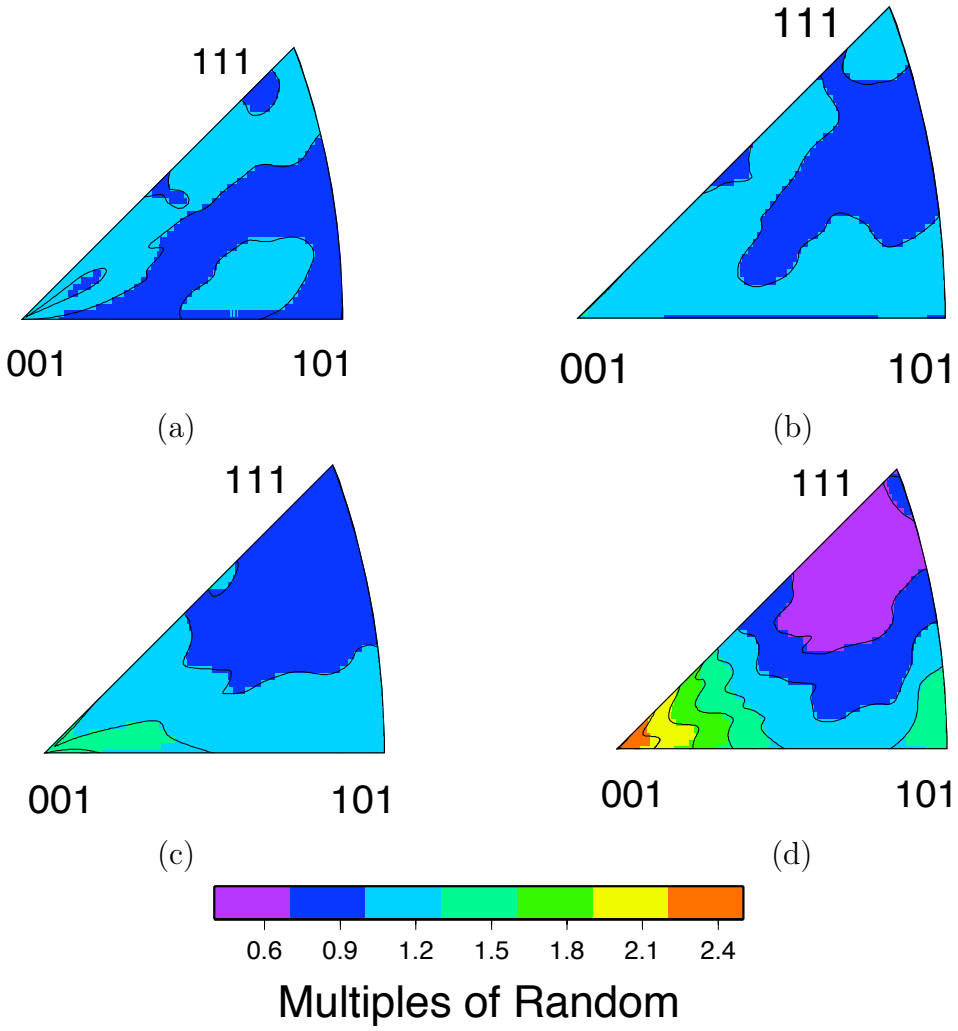

Figure 2.19: Inclination distributions are extracted at an intermediate timestep $t = 4000$ and plotted for (a) $\delta = 0$, (b) $\delta = 0.1$, (c) $\delta = 0.2$ and (d) $\delta = 0.3$. Simulations are performed in three dimensions on a 128-cubed domain. Comparing with fig. 2.5 we see that for *shrinking grains* populations and energies scale with each other.

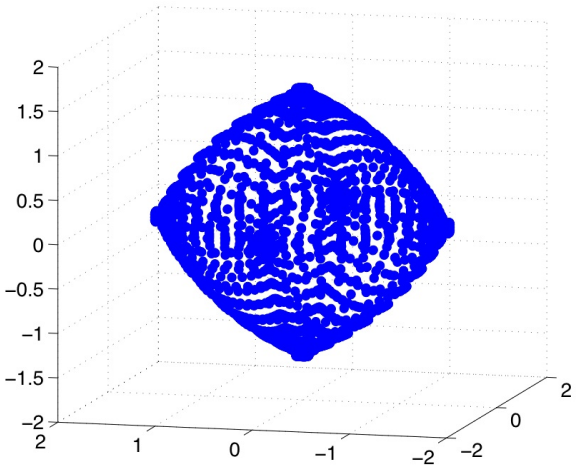

(a)

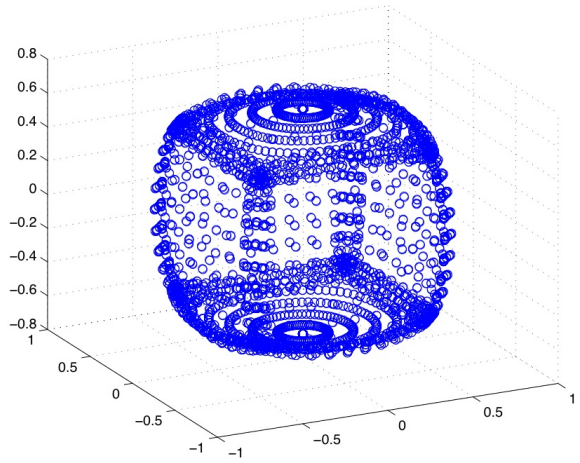

(b)

Figure 2.20: For an anisotropic function as in eq.2.13 with $\delta = 0.3$, expected kinetic shapes are shown when the isolated grain is (a) growing and (b) shrinking. Fig.(b) should be compared to intermediate shapes for shrinking grains, as seen in fig.2.18 (d). Note that *ears* or *flaps* appear, when the $1/\gamma$ plot (or the ξ plot in three dimensions) is concave (for inclinations at which the interfacial stiffness is negative, refer [58, 65]), which have to be discarded, and the remaining convex body gives the expected kinetic shape.

in and eliminate slow moving boundaries - hence a direct scaling is observed as expected.

2.5.2 Polycrystalline large-scale simulations in two and three dimensions

In the polycrystalline case, a 1500-squared grid in two dimensions was populated with voronoi grains (the average grain size is 32 voxels). The following set of simulations were performed to investigate the effect of varying boundary properties (energy and mobility), initial texture (random or otherwise) and constraints imposed at junctions (case-I or case-II) on grain boundary character. The initial microstructure is evolved for $N = 30000$ timesteps. Both number-weighted and area-weighted boundary distributions are extracted for $[1 - 2]$.

1. The boundary energy γ is anisotropic (as in eq.2.13 with $\delta = 0.3$), and is rescaled so that the minimum energy is 0.5 and the maximum energy is 1.5 (as in eq. 2.22,$0.5 \leq \gamma \leq 1.5$). The boundary mobililty is isotropic ($m = 1$). A random texture is assigned to the grains - the initial distribution of boundaries is sufficiently random. Boundary junctions are treated as isotropic (**case-I**), hence boundaries are constrained to meet at 120° (see section 2.5.2.1).

2. The boundary energy γ is anisotropic (as in eq.2.13 with $\delta = 0.3$) and rescaled ($0.5 \leq \gamma \leq 1.5$); the boundary mobililty is isotropic ($m = 1$). A random texture is assigned to the grains. Boundary junctions are treated as anisotropic (**case-II**), hence boundaries meet at angles dictated by the balance of anisotropic line energies (see section 2.5.2.1).

3. The boundary mobility m is anisotropic (as in eq.2.13 with $\delta = 0.3$) and is rescaled so that the minimum mobility is 0.01 and the maximum vaule is 1.0 ($0.01 \leq m \leq 1$). The boundary energy is isotropic ($\gamma = 1$). A random texture is assigned to the initial microstructure. Anisotropic boundary properties are allowed to percolate to junctions (case-II).

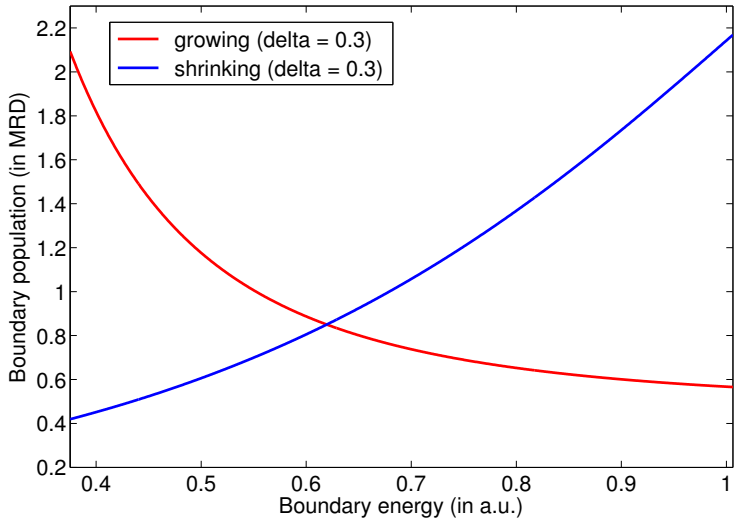

(a)

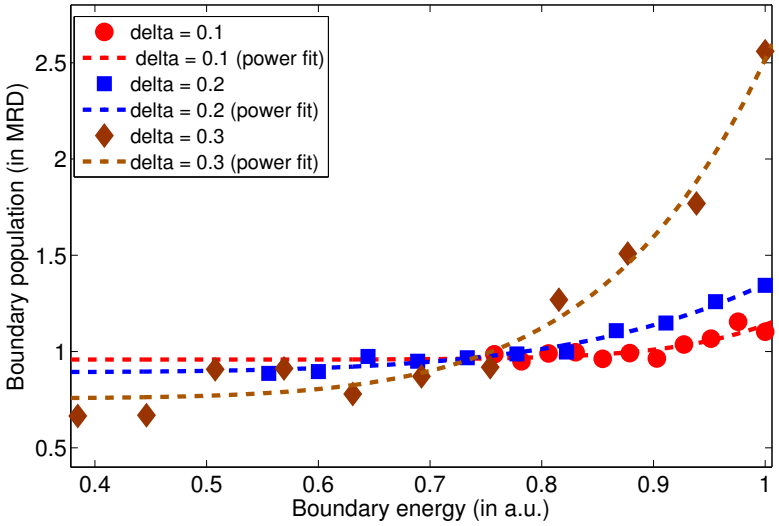

(b)

Figure 2.21: Variation of boundary population (in MRD) with boundary energy (in a.u.) for isolated grains. In (a) the expected variation is shown for growing and shrinking grains for $\delta = 0.3$ and in (b) the extracted variation is shown for shrinking grains for δ increasing from 0.1 to 0.3. Noth that for *shrinking grains* (which are bounded by *high-velocity* boundaries) populations and energies scale with each other.

4. Both boundary energy and mobility are anisotropic ($0.5 \leq \gamma \leq 1.5$, $0.01 \leq m \leq 1$). The initial texture is random and boundary junctions are treated as anisotropic (case-II).

5. A mild rolling texture is assigned to the initial microstructure. The boundary energy γ is anisotropic as in eq.2.13 and the boundary mobility m is isotropic ($0.5 \leq \gamma \leq 1.5$, $m = 1$).

6. A mild rolling texture is assigned to the initial microstructure. The boundary mobility m is anisotropic whereas the boundary energy γ is isotropic ($0.01 \leq m \leq 1$, $\gamma = 1$).

2.5.2.1 Effect of equilibrium constraints at junctions on grain boundary character

In case-I (*isotropic junctions*) equal energies are associated with interface fields in boundary junctions, and boundaries meet at an isotropic angle of 120°. In case-II (*anisotropic junctions*) anisotropic line energies permeate along GBs to junctions and hence boundaries are no longer constrained to meet at equal angles, instead they meet at angles dictated by the balance of these line energies. The boundary energy γ has a form as in eq. 2.13 with $\delta = 0.3$ and rescaled so that $0.5 \leq \gamma \leq 1.5$ (see fig. 2.5). Simulations are performed in two dimensions on a 1500^2-squared grid (populated with approximately 2200 randomly oriented grains), and the corresponding boundary populations are extracted at timesteps $t = 10000$, 20000 and 30000. In fig.2.22 we plot the extracted populations at $t = 30000$ as inverse pole figures (IPF) for cases-I and II. In case-I when boundaries are constrained to meet at equal angles, no inverse corelation shows up between boundary energy and population, in constrast to case-II, where anisotropic energies are extended to boundary junctions, and an inverse relation is seen between energy and population. For illustration purposes, a smaller 512^2-squared domain is evolved with identical initial texture and boundary energy but different equilibrium contraints imposed at the boundary junctions. The microstructure at $t = 30000$

steps is plotted in fig. 2.23a (case-I, isotropic junctions) and fig. 2.23b (case-II, anisotropic junctions).

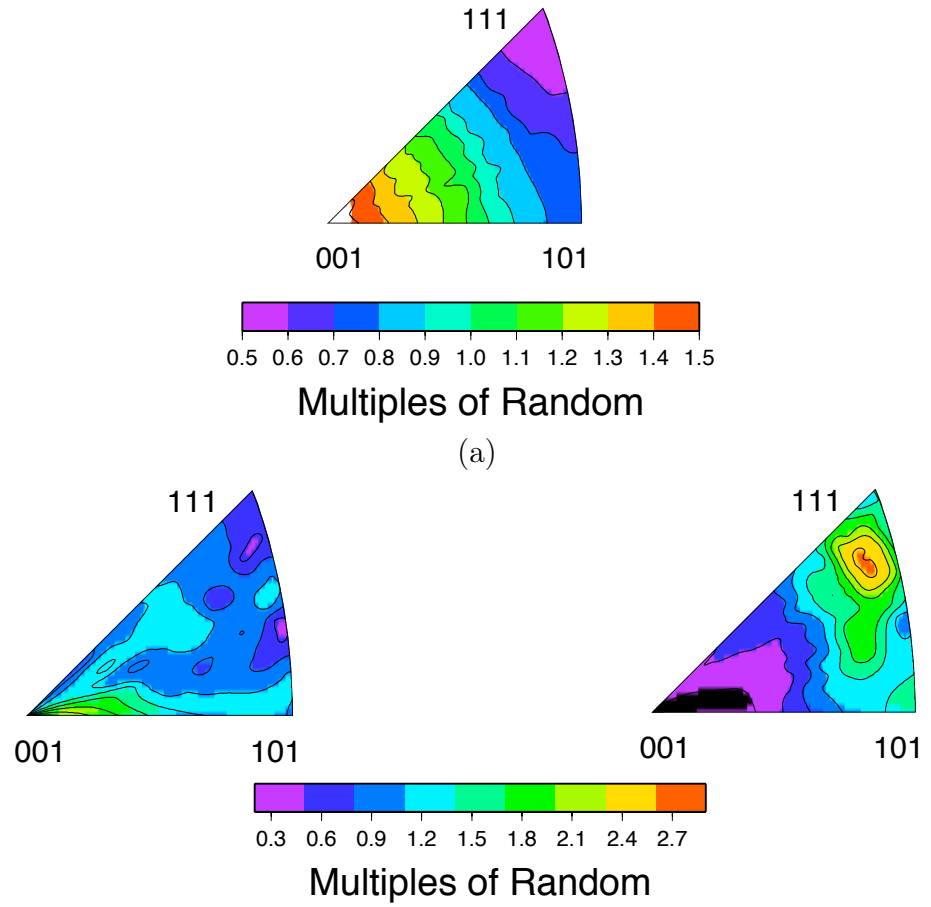

Figure 2.22: (a) Variation of boundary energy with boundary inclination (in a.u.), and the boundary population (in MRD) collected at $t = 30000$ for (b) isotropic junctions and (c) anisotropic junctions. Note that in case-II an inverse relation between boundary energy and population is evident. Simulations are performed in two dimensions on a 1500-squared grid, and the initial texture is random.

Holm *et al.* argued that during anisotropic grain growth boundaries rotate to achieve mechanical equilibria at boundary junctions and as a result low-energy boundaries lenghten at the expense of high-energy ones[23]. This leads to the observed anisotropy in boundary populations and the inverse relation between boundary energy and population. In the simulations presented here boundaries are *constrained* to meet at equal angles in case-I (*isotropic junctions)* in contrast to case-II (*anisotropic junctions*) where they are *free* to positions dic-

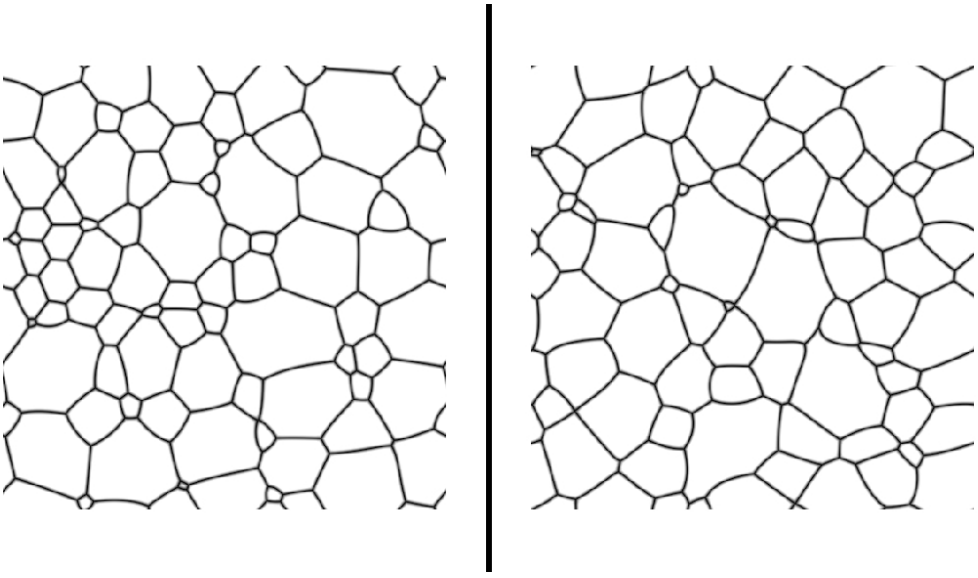

(a) (b)

Figure 2.23: Microstructure at $t = 30000$ steps when junctions are treated as (a) isotropic and (b) anisotropic. Note that in (a) dihedral angles are close to the isotropic value of 120° in contrast to (b) where angles deviate from 120°.

tated by the balance of anisotropic line energies. This helps to explain the strong inverse relation between boundary energy and distribution for *anisotropic junctions* (comparing fig. 2.22(a) to (c)) in contrast to *isotropic junctions* (compare fig.2.22(a) to (b)).

To illustrate this further, a model 5-grain structure (in two dimensions) is evolved with a boundary energy γ (as in fig.2.15) with a minimum value for inclinations at 0° and 90°. The isotropic evolution of the grain structure is similar to its evolution when junctions are treated as *isotropic* (compare fig. 2.24(b) to (c)) in contrast to its evolution when junctions are treated as *anisotropic* (see fig. 2.24(d)), where low-energy boundaries (at 0° and 90° inclinations) lengthen at the expense of high-energy boundaries. The observed *asymmetry* in fig. 2.24(b,c) compared to fig. 2.24(d) depends on the initial radius of the central (circular) grain with respect to the domain size. For example for a 128^2 squared domain, if the initial radius of the central grain changes from 44 voxels to 48 voxels, the intermediate grain shapes (assuming isotropic boundary energies) is shown in fig.2.25 - the thing to note is that boundaries meet at the isotropic value of 120°. For anisotropic junctions, irrespective

of initial grain radius, dihedral angles deviate from 120° and low-energy boundaries (those at 0° and 90° inclination for the present example) lengthen at the expense of high-energy boundaries, as in fig. 2.26.

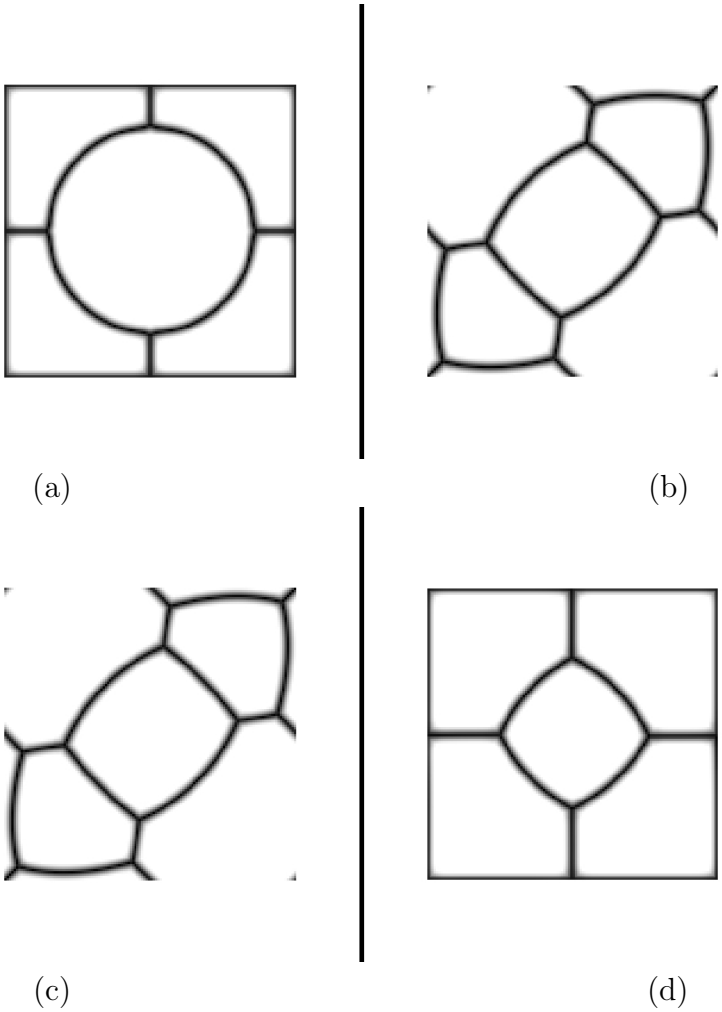

Figure 2.24: 5−grain structure at (a) $t = 0$, and at $t = 15000$ evolved with (b) isotropic boundary energy (c) anisotropic boundary energy γ with a minimum for 0°and 90° inclinations and junctions *constrained* to meet at equal angles (*isotropic junctions*) (d) anisotropic energy γ with a minimum for 0°and 90° inclinations and *free (anisotropic) junctions*. Note that in (d) low-energy boundaries lengthen with time.

In fig. 2.27 the variation of boundary population with boundary energy is shown for case-I *(isotropic junctions)* and case-II *(anisotropic junctions)* at $t = 10000$. The inverse relation between energy and population is evident for case-II in contrast to case-I.

In the following figure fig. 2.28 we explore the sensitivity of boundary distributions

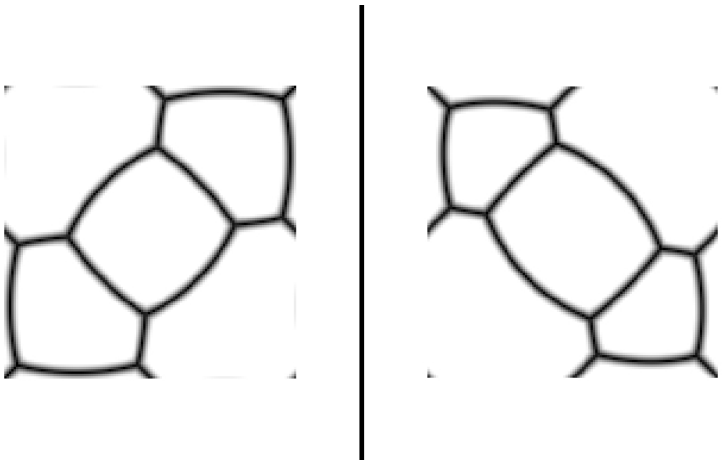

(a) (b)

Figure 2.25: Intermediate grain shapes for five-grain structure as in fig.2.24(a) evolved with isotropic boundary energies for an initial circular grain radius of (a) 44 voxels and (b) 48 voxels. The *asymmetry* shifts but boundaries still meet at the isotropic value of 120°.

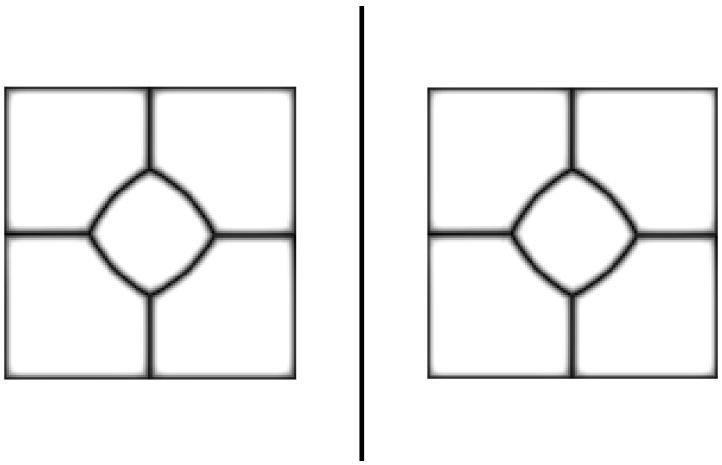

(a) (b)

Figure 2.26: Intermediate grain shapes for five-grain structure as in fig. 2.24(a) evolved with anisotropic energies (with a minimum for 0° and 90° inclinations) and these energies extended to boundary junctions (case-II), for an initial circular grain radius of (a) 44 voxels and (b) 48 voxels. Irrespective of the initial grain radius low-energy boundaries increase while high-energy boundaries decrease in length, and dihedral angles deviate from 120°.

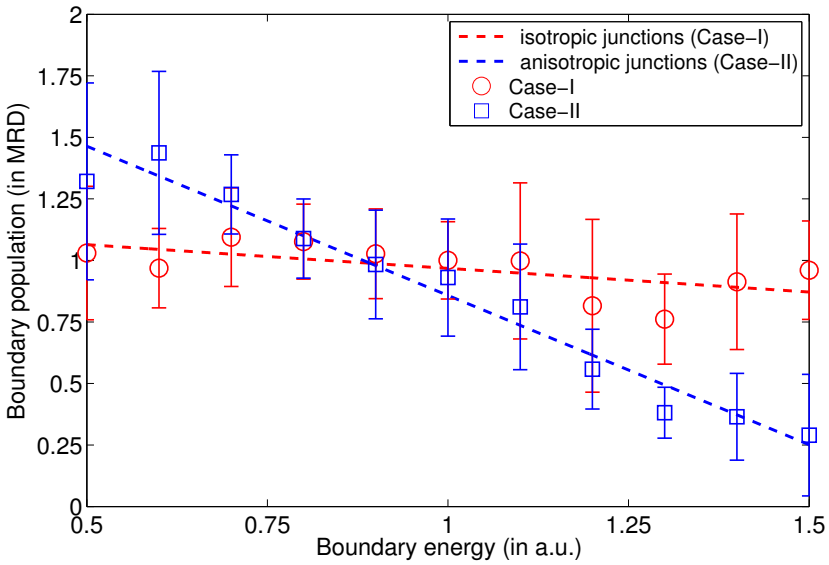

Figure 2.27: Boundary population (in MRD) plotted with boundary energy (in a.u.) for *isotropic junctions* (case-I) and *anisotropic junctions* (case-II). Simulations are performed in two dimensions on 1500-squared domain and populations are collected at $t = 10000$. Note that these scale inversely with each other (in case-II) when boundaries are not *constrained* to meet at equal angles (as in case-I).

to the number of timesteps t chosen for data collection and the number of grains (or the overall domain size) in the initial microstructure $g(0)$. A *sufficiently* large number of grains should be used so that the initial distribution of boundaries is *nearly* random, and the initial microstructure (with random texture) has to be evolved for a *sufficiently* large number of timesteps till *steady-state* has been achieved and thereafter no siginificant changes in distributions occur. It can be infered that $t = 10000$ is sufficiently long and $g = 1000$ is sufficiently large.

To test the effect of simulation parameters such as the timestep $\triangle t$ and the boundary width λ chosen on boundary distributions, we evolve an identical microstructure (1024^2 domain populated with approximately 1000 grains, grains are randomly oriented with each other) for $t = 10000$ steps, with identical initial texture. The boundary width is varied as $\lambda = 4, 8, 16$ points (keeping the timestep constant at $\triangle t = 0.02$) and the timestep is varied as $\triangle t = 0.01, 0.02, 0.04$ (at constant boundary width constant at $\lambda = 8$ points). It can be

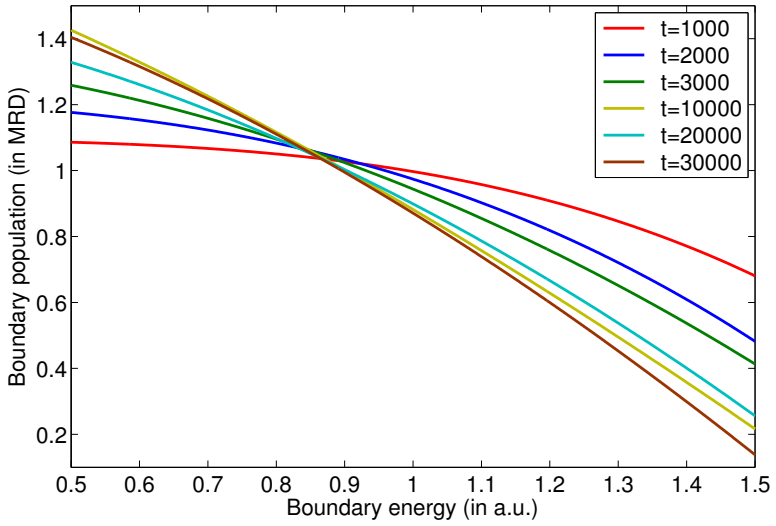

(a)

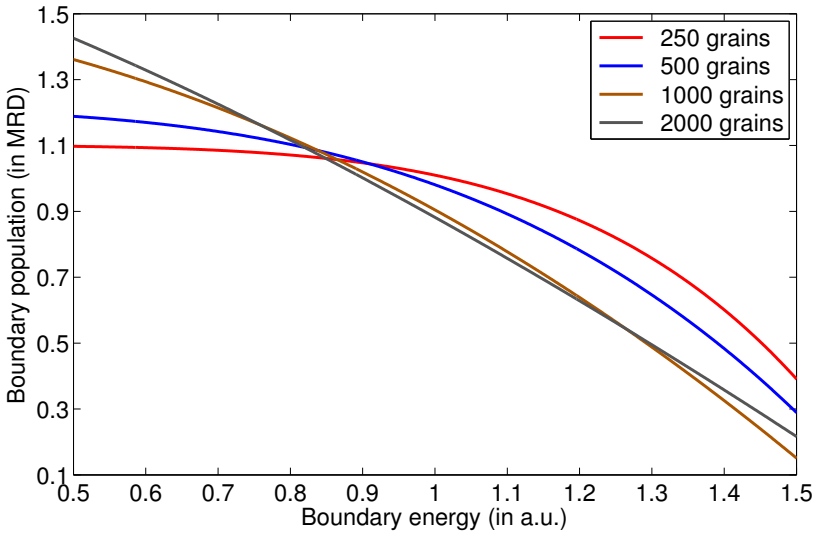

(b)

Figure 2.28: (a) Boundary distributions are extracted at different timesteps. Note that anisotropy in populations develops as arealy as $t = 1000$ timesteps but a steady-state in boundary distribution is observed after $t = 10000$ timsesteps (b) At $t = 10000$ boundary population are extracted for varying number of initial grains. Note that no significant strengthening in anisotropy of boundary population is observed for number of grains $g \geq 1000$.

observed in figs. 2.29,2.30 that boundary distributions are more sensitive to the boundary width chosen, compared to the value of timestep chosen if the total time evolved is kept fixed (where total time evolved is calculated as the product of evolution steps and the timestep $\triangle t$).

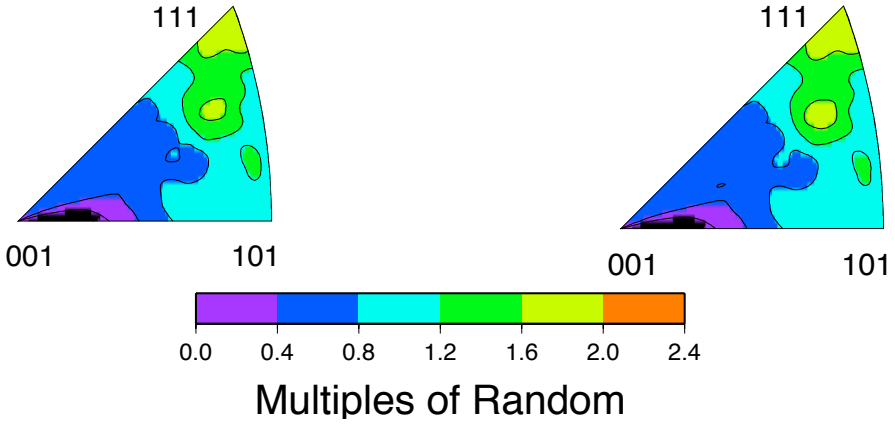

(a) (b)

Figure 2.29: Boundary distributions extracted from a 1024^2 domain populated with 1024 grains, with a boundary width of $\lambda = 8$ points, evolved for (a) 10000 steps and $\triangle t = 0.02$ and (b) 5000 steps and $\triangle t = 0.04$ with a boundary energy as in fig. 2.22(a). The distributions are similar, demonstrating the relative insensitivity to the timestep chosen.

Gruber *et al.* have proposed that low-energy boundaries increase both in number and in area [20] (in contrast to Holm's arguments that low-energy boundaries only increase in area) through a *critical-event* mechanism. To test this, we extract the number-weighted and area-weighted boundary distributions and have plotted them in fig.2.31. It can be seen that low-energy boundaries increase both in number and in area (the inverse relation is stronger in terms of area-weighted statistics than in terms of number-weighted distributions), or in other words, there are more and larger low-energy boundaries compared to high-energy ones. A steady state in distributions is attained at $t = 10000$.

In three dimensions a 160-cubed domain (with an initial grainsize of 16 voxels, which gives an initial microstructure of 1000 grains) was used. A random texture was assigned to the initial microstructre. The effect of different constraints imposed at boundary junctions on the development of boundary character was explored by evolving the initial microstrucutre

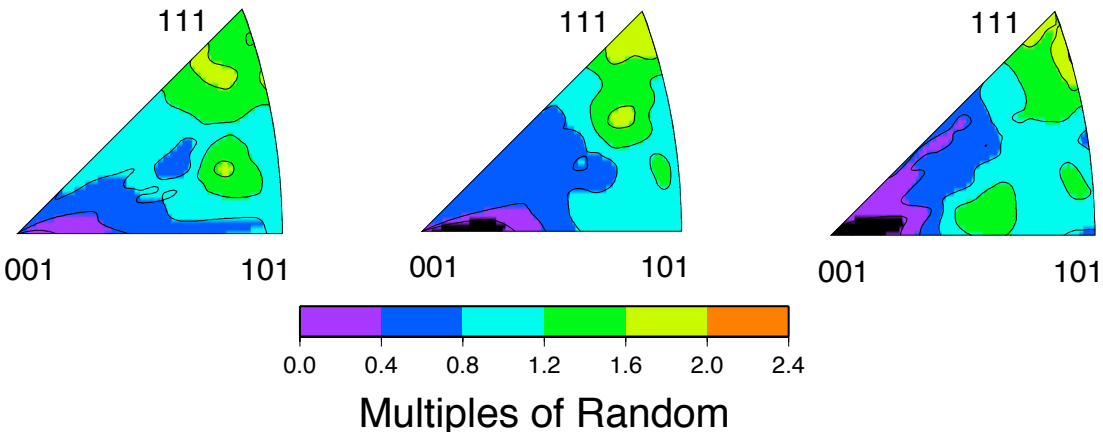

(a) (b) (c)

Figure 2.30: Boundary distributions extracted from a 1024^2 domain populated with 1024 grains, evolved for 10000 evolution steps with a boundary energy as in fig. 2.22(a), with a timestep $\triangle t = 0.02$ and a boundary width of (a) $\lambda = 4$ (b) $\lambda = 8$ and (c) $\lambda = 16$ points. The distributions are relatively sensitive to the value of the boundary width chosen.

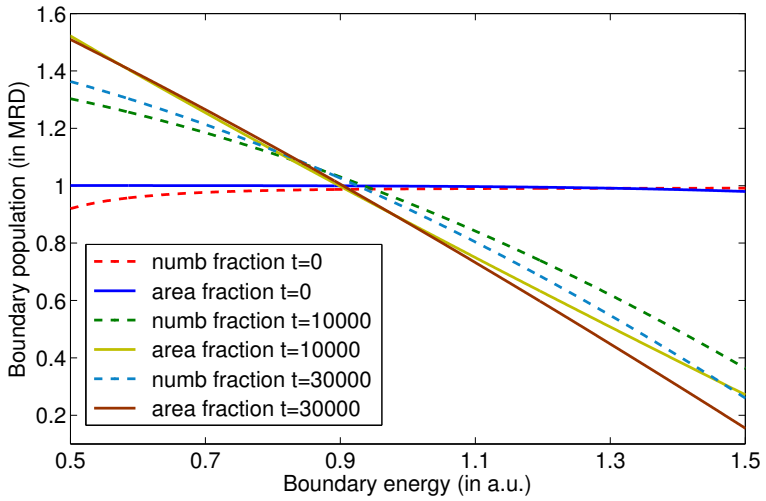

Figure 2.31: Number-weighted and area-weighted boundary distributions extracted from two-dimensional simulations (junctions are treated as *anisotropic*, case-II) at $t = 0$ (initial state) and at $t = 10000, 30000$ timesteps. Note that low-energy boundaries increase in number and in area as suggested by Gruber *et al. [20]*

for $t = 3000$ evolution steps, as in $[1-2]$ listed above. An evolution step is said to have elapsed when each voxel in the computational domain has been considered for updation. The timestep in the present simulation is chosen to be 0.02. In fig.2.32 the boundary populations are plotted as inverse polefigures at $t = 3000$ and compared to the anisotropy in boundary energy for cases-I and II. As in two dimensions we see a strong inverse corelation between population and energy in case-II. In fig. 2.33 the grain strucutre at $t = 3000$ for a smaller 64-cubed domain is shown for comparison - in case-I boundaries are *constrained* to meet at equal angles in contrast to case-II where they are *free* to meet at angles dictated by the balance of anisotropic line energies. In fig. 2.34 the variation of boundary population with boundary energy is shown at $t = 3000$.

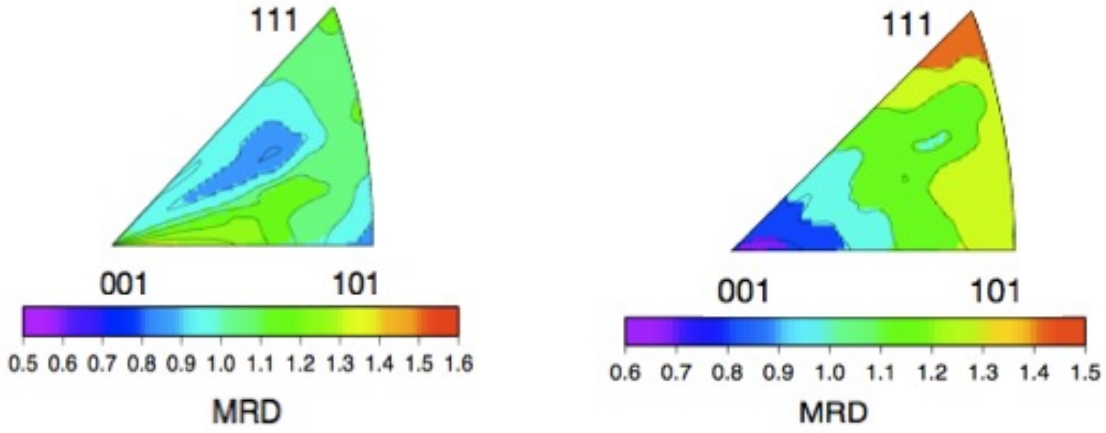

(a) (b)

Figure 2.32: Boundary population collected at $t = 3000$ for (a) isotropic junctions (case-I) and (b) anisotropic junctions (case-II), for a boundary energy varying as in fig.2.22(a). Note that in case-II the inverse relation between boundary energy and population is evident. Simulations are performed in three dimensions on a 160-cubed grid initially populated with 1000 grains with random texture.

2.5.2.2 Effect of anisotropic boundary mobility on grain boundary character

The boundary mobility m is varied as in eq. 2.13 and rescaled so that $0.01 \leq m \leq 1$ (see fig.2.35). Simulations are performed in two dimensions on a 1500-squared domain initially populated with approximately 2000 grains with random texture. The boundary energy

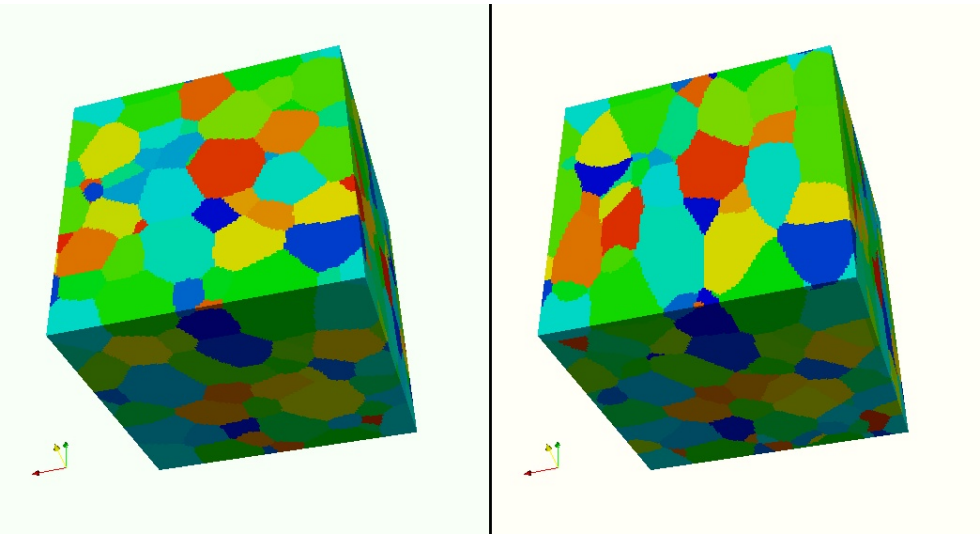

(a) (b)

Figure 2.33: Polycrystalline snapshots at intermediate timestep $t = 3000$ for (a) isotropic junctions (case-I), and for (b) anisotropic junctions (case-II). Simulations are performed in three dimensions on a 64-cubed domain and evolved with a boundary energy as in fig.2.22(a). Boundaries tend to be more faceted and dihedral angles deviate from 120° when anisotropic energies are extended to boundary junctions (compare (b) to (a)).

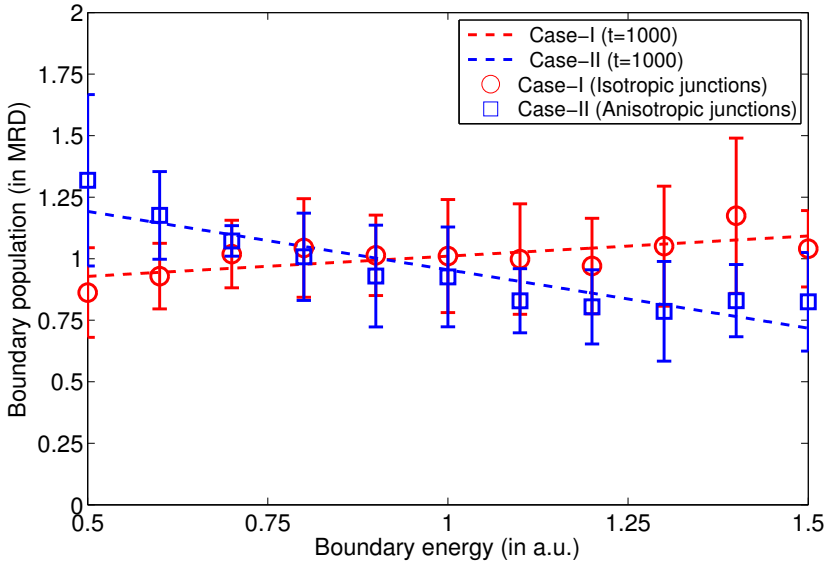

Figure 2.34: Boundary population (in MRD) plotted with boundary energy (in a.u.) for *isotropic junctions* (case-I) and *anisotropic junctions* (case-II). Simulations are performed in three dimensions on 160-cubed domain and populations are collected at $t = 3000$. Note that these scale inversely with each other (in case-II) when boundaries are not *constrained* to meet at equal angles (as in case-I).

γ is isotropic ($\gamma = 1$). Both boundary energies and mobilities permeate along GBs to junctions (*anisotropic junctions*). In fig. 2.36 (a) boundary populations are extracted at $t = 30000$ and plotted. Comparing with populations extracted from microstructures evolved with an anisotropic boundary energy (as in fig. 2.36 (b)) it is seen that boundary mobility has significantly lesser effect on the development of anisotropy in grain boundary character compared to boundary energy, when the initial texture is random [68]. For illustration purposes, a smaller 512^2- squared domain is evolved with identical initial (random) texture but with different boundary properties for $t = 30000$ timesteps. The microstructure is shown in fig.2.37(a) (anisotropic boundary energy and isotropic mobility, $0.5 \leq \gamma \leq 1.5, m = 1$) and fig. 2.37(b) (anisotropic boundary mobility and isotropic energy, $0.01 \leq m \leq 1, \gamma = 1$).

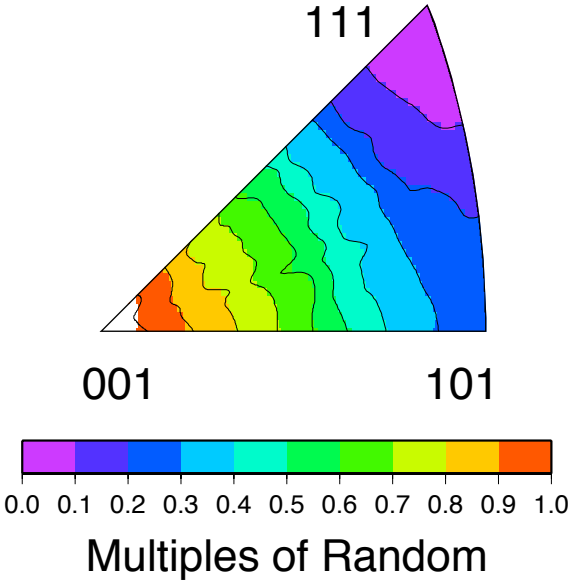

Figure 2.35: Variation of boundary mobility with inclination (in $a.u.$), in three dimensions as in eq.2.13 with $\delta = 0.3$ and rescaled to $0.01 \leq m \leq 1$.

Kazaryan *et al.* predicted that boundary mobility has limited influence on boundary distributions when the initial texture is random [68]. In the present work it has been hypothesized that equilibrium constriants at boundary junctions have a significantly greater influence on boundary character than anisotropic boundary kinetics. Further it has been shown above that an inverse relation between energy and population develops when bound-

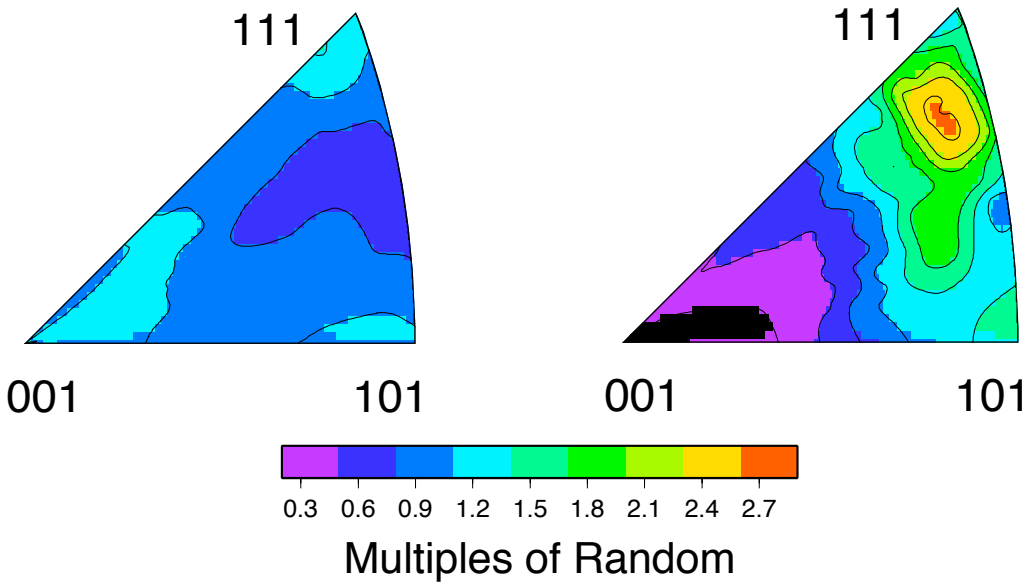

(a) (b)

Figure 2.36: Boundary population extracted from simulations in two dimensions at $t = 30000$ for boundary properties varying as (a) $0.01 \leq m \leq 1, \gamma = 1$ as in fig. 2.35 and (b) $0.5 \leq \gamma \leq 1.5, m = 1$ as in fig, 2.5. Note that anisotropy in boundary mobility does not result in an anisotropy in boundary population, in contrast to the strong inverse relation between boundary energy and population.

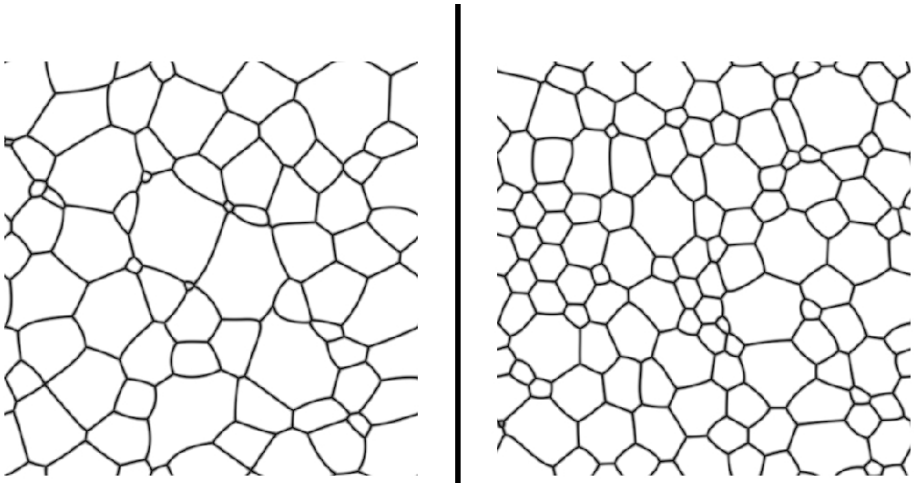

(a) (b)

Figure 2.37: Simulations are performed in two dimensions on a 512-squared domain and the initial microstructure is evolved for $t = 30000$ steps, with boundary properties varying as (a) $0.01 \leq m \leq 1, \gamma = 1$ as in fig. 2.35 and (b) $0.5 \leq \gamma \leq 1.5, m = 1$ as in fig, 2.5. Note that in (a) dihedral angles deviate from the isotropic value of 120°, in contrast to (b) where boundaries meet at equal angles.

aries are not constrained to meet at equal angles, but are free to rotate to positions dictated by the balance of anisotropic boundary energies. When the boundary energy is isotropic, boundaries meet at angles close to the isotropic value, irrespective of the anisotropy in boundary mobility. In this case no such inverse relation between boundary mobility and population is observed. Since the average mobility is less than unity, the kinetics of grain growth decreases, with no change in grain boundary character.

To demonstrate this a 4-grain structure is evolved with varying boundary properties - both boundary energy and mobility depend only on the pair of grains on either side. Boundary properties permeate along GBs to boundary junctions (*anisotropic* junctions*, case-II).* As seen in fig. 2.38 the steady-state dihedral angle θ (defined as in fig. 2.12) depends only on the ratio of boundary energies $r_\gamma = \frac{\gamma_{jk}}{2\gamma_{1j}}$ and not on the ratio of boundary mobilities $r_m = \frac{m_{jk}}{2m_{1j}}$. Hence an anisotropy in boundary mobilities does not result in a deviation of dihedral angles from values dictated by the balance of line energies (which gives $\theta = 2cos^{-1}\left(\frac{\gamma_{jk}}{2\gamma_{1j}}\right)$).

The expected and measured dihedral angles for varying boundary properties (as in fig. 2.38(a)-(i)) are shown in the table.2.1 below. Note that these only depend on the relative values of boundary energies r_γ and do not depend on boundary mobilities r_m.

Index in fig. 2.38	Boundary energy γ	Boundary mobility m	$\theta_{theo} = 2cos^{-1}\left(\frac{\gamma_{jk,j,k\neq1}}{2\gamma_{1j,j\neq1}}\right)$	θ_{meas}
a	$\gamma_{ij} = 1.0$	$m_{1j,j\neq1} = 0.5$	120°	118°
b	$\gamma_{ij} = 1.0$	$m_{1j,j\neq1} = 1.0$	120°	124°
c	$\gamma_{ij} = 1.0$	$m_{1j,j\neq1} = 2.0$	120°	122°
d	$\gamma_{1j,j\neq1} = 0.5$	$m_{1j,j\neq1} = 0.5$	0°	24°
e	$\gamma_{1j,j\neq1} = 0.5$	$m_{1j,j\neq1} = 1.0$	0°	22°
f	$\gamma_{1j,j\neq1} = 0.5$	$m_{1j,j\neq1} = 2.0$	0°	19°
g	$\gamma_{jk,j,k\neq1} = 0.5$	$m_{1j,j\neq1} = 0.5$	151°	153°
h	$\gamma_{jk,j,k\neq1} = 0.5$	$m_{1j,j\neq1} = 1.0$	151°	146°
i	$\gamma_{jk,j,k\neq1} = 0.5$	$m_{1j,j\neq1} = 2.0$	151°	145°

Table 2.1: Comparison of measured and theoretical dihedral angles for the four-grain structure, evolving under varying boundary conditions.

In fig. 2.39 the variation of boundary population with reduced boundary mobility $\mu = m\gamma$ is plotted at $t = 30000$. When only boundary mobility varies (with isotropic boundary

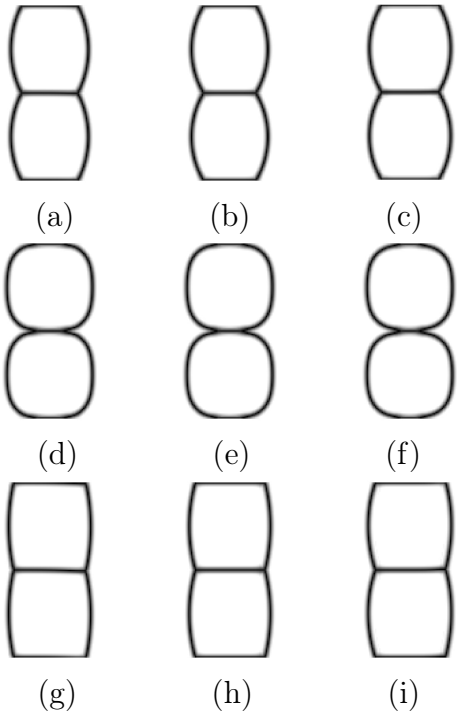

Figure 2.38: Evolution of four-grain structures (in two dimensions) with (a) $\gamma_{ij} = 1.0, m_{1j,j\neq1} = 0.5$ (b) $\gamma_{ij} = 1.0, m_{1j,j\neq1} = 1.0$ (c) $\gamma_{ij} = 1.0, m_{1j,j\neq1} = 2.0$ (d) $\gamma_{1j,j\neq1} = 0.5, m_{1j,j\neq1} = 0.5$ (e) $\gamma_{1j,j\neq1} = 0.5, m_{1j,j\neq1} = 1.0$ (f) $\gamma_{1j,j\neq1} = 0.5, m_{1j,j\neq1} = 2.0$ (g) $\gamma_{jk,j,k\neq1} = 0.5, m_{1j,j\neq1} = 0.5$ (h) $\gamma_{jk,j,k\neq1} = 0.5, m_{1j,j\neq1} = 1.0$ (i) $\gamma_{jk,j,k\neq1} = 0.5, m_{1j,j\neq1} = 2.0$. Note that steady-state dihedral angles are independent of boundary mobilities m_{ij} and vary only with boundary energies γ_{ij}.

energy) as $0.01 \leq m \leq 1, \gamma = 1$, no significant anisotropy in boundary character is observed. For an anisotropic boundary energy (with isotropic boundary mobility) as $0.5 \leq \gamma \leq 1.5, m = 1$, an inverse relation between reduced mobility μ and population is observed. When both boundary energy and mobility are anisotropic as $0.5 \leq \gamma \leq 1.5, 0.01 \leq m \leq 1$, a similar inverse relation is seen. Hence, anisotropy in grain boundary character develops primarily due to an anisotropy in boundary energy.

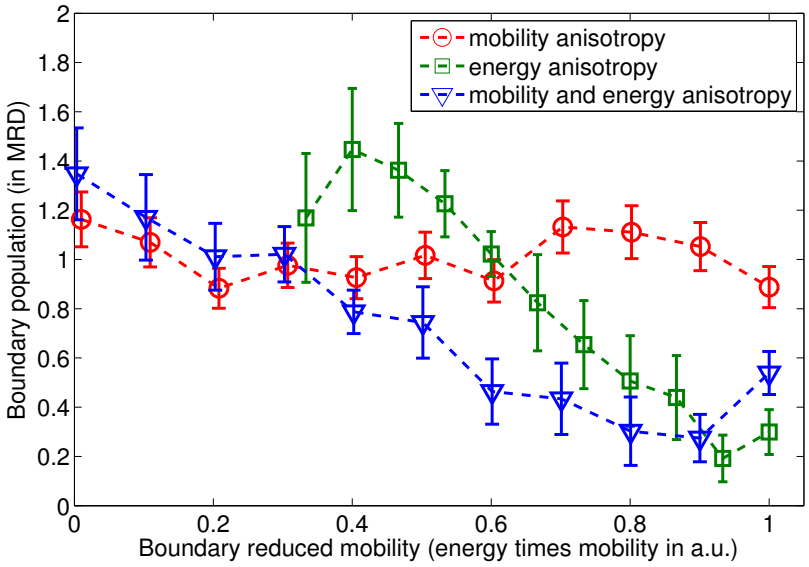

Figure 2.39: Variation of boundary population with reduced mobility extracted from two-dimensional simulations at $t = 30000$. An inverse relation is seen when the boundary energy is anisotropic, irrespective of the anisotropy in boundary mobility.

2.5.2.3 Effect of initial texture on development of anisotropic boundary character

Ma *et al.* have proposed that in the presence of an initial texture both boundary energy and mobility have an influence on boundary distributions [35, 20]. For the case the microstructure is strongly textured, it was shown that boundary energy strengthens texture in contrast to boundary mobility which decreases texture. To test the effect of initial texture on boundary character during anisotropic grain growth, the initial microstructure (1500-squared domain

in two dimensions, populated with approximately 2000 grains) is assigned a mild rolling texture so that the initial distribution of grain boundaries is not random. This is evolved with anisotropic boundary energy and isotropic mobility (as in fig. 2.5, $0.5 \leq \gamma \leq 1.5, m = 1$), and the initial distribution is compared to the boundary distribution at $t = 10000, 30000$. The initial anisotropy in distributions is strengthened so that low-energy boundary grow at the expense of higher energy ones (see fig.2.40). The variation of boundary population with energy is shown in fig.2.41 - it is to be noted that the initial texture in boundary plane distribution is strengthened and no steady-state is seen (as observed for the case of initial random texture at $t = 10000$).

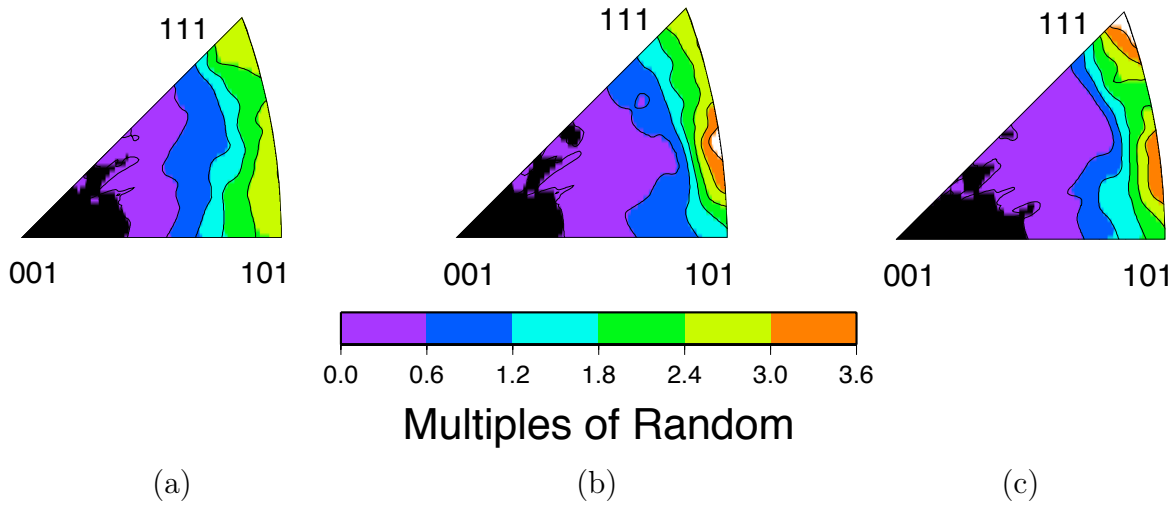

(a) (b) (c)

Figure 2.40: Boundary population extracted at (a) $t = 0$ (initial) (b) $t = 10000$ and (c) $t = 30000$. It can be noted that no *steady-state* exists, and the initial (boundary plane) texture is strengthened with time for an anisotropic boundary energy.

The initial microstructure (asigned with an initial rolling texture) is evolved with anisotropic boundary mobilities (and isotropic energy), as in fig. 2.35 ($0.01 \leq m \leq 1, \gamma = 1$) to explore the effect of anisotropic mobility on populations in the presence of texture. In fig.2.42 the boundary populations are plotted at $t = 0$ (initial), and at subsequent timesteps $t = 10000, 30000$. The variation of boundary population with mobility is shown in fig. 2.43- it is to be noted that the initial texture in boundary plane distribution decreases with time and no steady-state is observed.

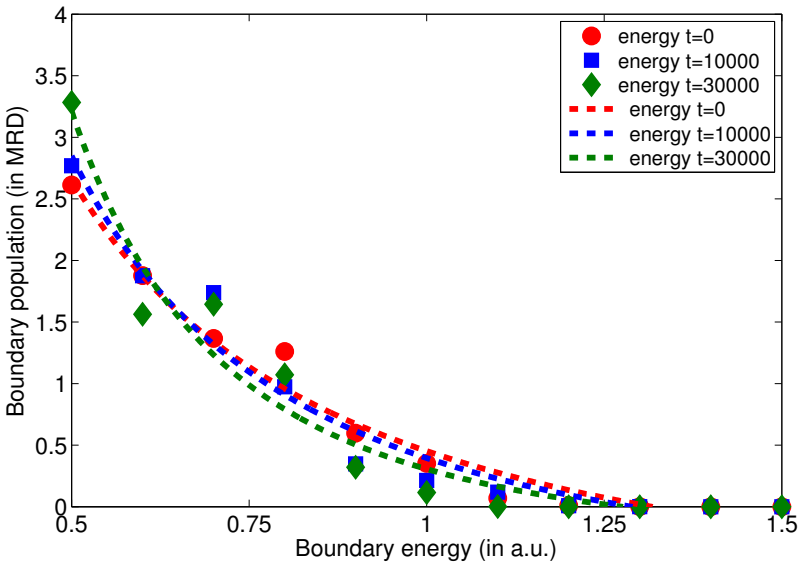

Figure 2.41: Boundary population plotted with boundary energy for timesteps $t = 0, 10000, 30000$. The initial anisotropy in boundary population (color coded red) grows with time (compare red to green).

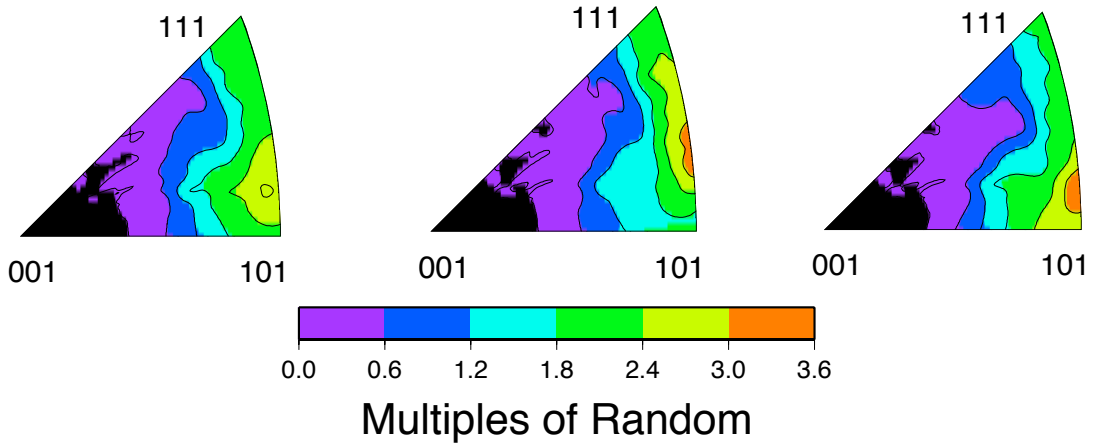

(a) (b) (c)

Figure 2.42: Boundary population extracted at (a) $t = 0$ (initial) (b) $t = 10000$ and (c) $t = 30000$. It can be noted that no *steady-state* exists, and the initial (boundary plane) texture decreases with time when the boundary mobility is anisotropic.

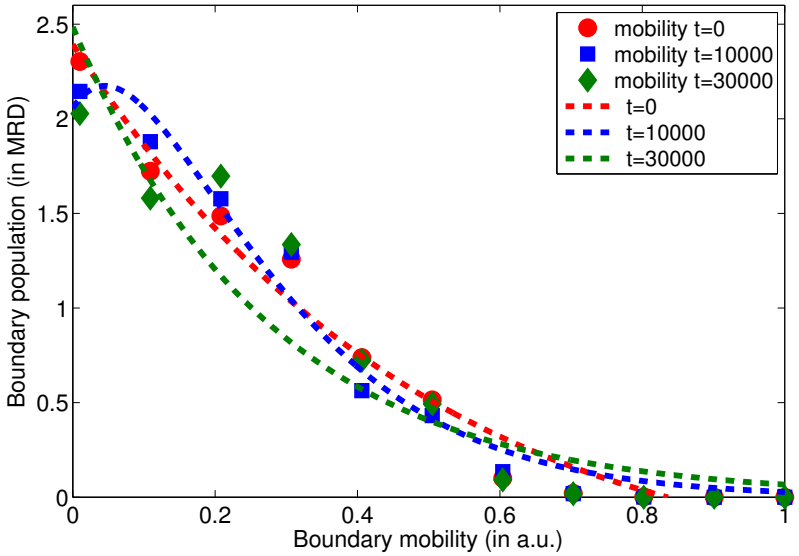

Figure 2.43: Boundary population plotted with boundary mobility for timesteps $t = 0, 10000, 30000$. The initial anisotropy in boundary population (color coded red) weakens with time (compare red to green).

2.6 Conclusion

The following conclusions can be derived from the present chapter

1. For an anisotropic boundary energy, the evolution of isolated grains is different from the evolution of polycrystalline systems, due to the presence of boundary junctions. For isolated shrinking grains, populations scale with boundary energy, in contrast to microstructure evolution in polycrystalline systems, where different equilibrium conditions at junctions result in significantly different boundary populations. An inverse relation between boundary energies and populations is obtained in the polycrystalline case, when boundaries are *free* to rotate, and dihedral angles deviate from the isotropic value of 120° to values dictated by mechanical equilibrium conditions at these junctions. A similar deviation in the distribution of dihedral angles from the isotropic value of 120° have been observed experimentally in anisotropic systems by Dillon *et al. [12]*.

2. When the initial texture in polycrystalline syatems is random, an anisotropy in bound-

ary mobility does not result in a corresponding anisotropy in boundary populations, in contrast to the inverse relation between boundary energy and population. Hence, a higher incidence of low-energy grain boundary planes in polycrystals can be viewed as a natural consequence of satisfying mechanical equilibrium conditions at triple junctions, which have a significantly greater effect on the development of anisotropic boundary character compared to the effect of kinetic factors (as boundary mobility). This is in contrast to the evolution of isolated grains where grain shapes and boundary distributions depend on the anisotropy in kinetic factors (as boundary velocity, which scales with boundary energy and mobility).

3. Low-energy boundaries grow at the expense of high-energy ones, both in number and in area. This is in contrast to Holm 's [23] arguments that low-energy boundaries increase in area and not in number. The anisotropy in boundary character cannot be explained solely through a *boundary-lengthening* mechanism. The *number-weighted* and *area-weighted* anisotropy in boundary population support a *critical-event* mechanism propsed by Gruber *et al.* [20] which predicts an increase of the number and the area of low-energy boundaries in polycrystalline systems.

4. The initial texture has a siginificant effect on the distribution of boundary populations during anisotropic grain growth. A non-random texture constrains the strength in anisotropy (in boundary populations) that can be achieved due to an anisotropy in boundary energy (and mobility). When the initial texture is random, a strong inverse relation is seen between boundary energy and population and a steady-state in distributions exists. In the case of a non-random initial texture, neither a strong correlation (between boundary energy and population) nor a steady-state in distributions is observed.

Chapter 3

Deriving anisotropic boundary energies and populations for face-centred cubic metals

3.1 Introduction

In the present chapter, we derive the variation of grain boundary energy for fcc metals (like nickel and aluminum) in the five-parameter grain boundary space. Recently energies for such systems were estimated through use of simulations [49] and experiments [32]. Since these energies were estimated for only a limited number of GB types (certain CSL boundary types in the method described by Olmsted et al.), an interpolative method is needed to estimate energy of a grain boundary (GB) of arbitrary type. Such a method needs the selection of a proper metric to estimate closeness between any two arbitrary GB types. An informative review of metrics with associated advantages and disadvantages by Cahn et al. can be refered to [7]. In the present chapter we describe the use of two such metrics [44, 48] and compare the interpolated energies to those observed experimentally in nickel [32]. A series of simulations are performed incorporating these interpolated energies in the interface-field

framework discussed in the present work, and the anisotropy in boundary populations is correlated to the anisotropy in interpolated energies.

3.2 Methodology and results

Li *et al.* derived grain boundary energies for nickel using orientation imaging of nickel and serial sectioning techniques [32]. These energies were reconstructed using a capillarity vector method described in reference [43]. To derive the aforementioned energies, a large number of grain boundaries were collected using orientation-mapping on serial-sectioned nickel and binned in the five-parameter grain boundary space [32]. The discretization interval is 8.2° for all five dimensions (of the boundary space), and there are about $644,200$ cells (or grain boundary types, not all of them being distinct from each other) in the grain-boundary space. Details for the data collection and energy reconstruction are not provided here. The variation of boundary energies with the boundary plane normal for specific Σ boundaries is plotted in fig. 3.1.

In a recent paper, Olmsted et al. calculated energies of a set of CSL grain boundary types for face-centred metals (as nickel and aluminium) [49]. Since the number of GB types with known energies is sparse, an interpolation procedure is necessary to derive energy of a boundary having arbitrary misorientation and inclination. This requires the use of an appropriate metric to estimate the distance between GB types, and to subsequently assign the energy of its closest neighbor (whose energy is known) to an arbitrary boundary type.

3.2.1 Representation of grain boundaries (in (A,B) form)

Since grain boundaries in three dimensions have five degrees of freedom (the first three related to misorientation across the boundary and the last two related to the boundary plane normal in the crystal reference frame), a five dimensional energy matrix needs to be constructed, where the value of cell $[c_1, c_2, c_3, c_4, c_5]$ corresponds to the energy of a grain boundary having

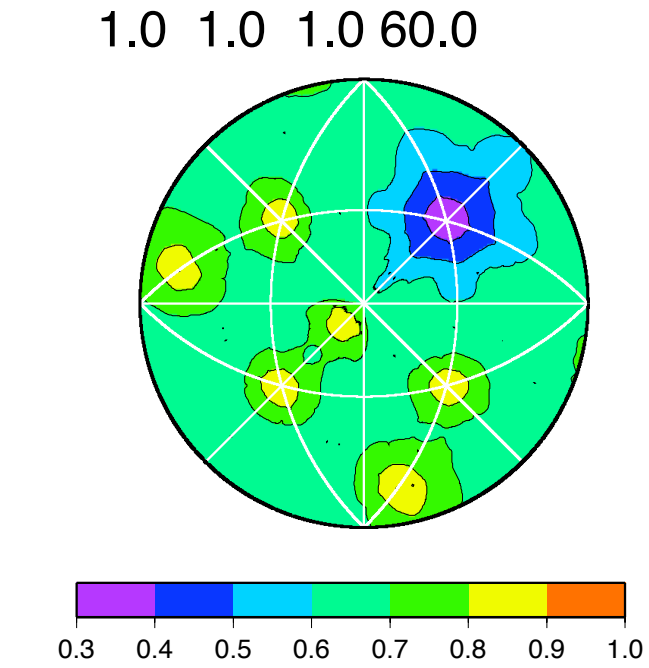

(a)

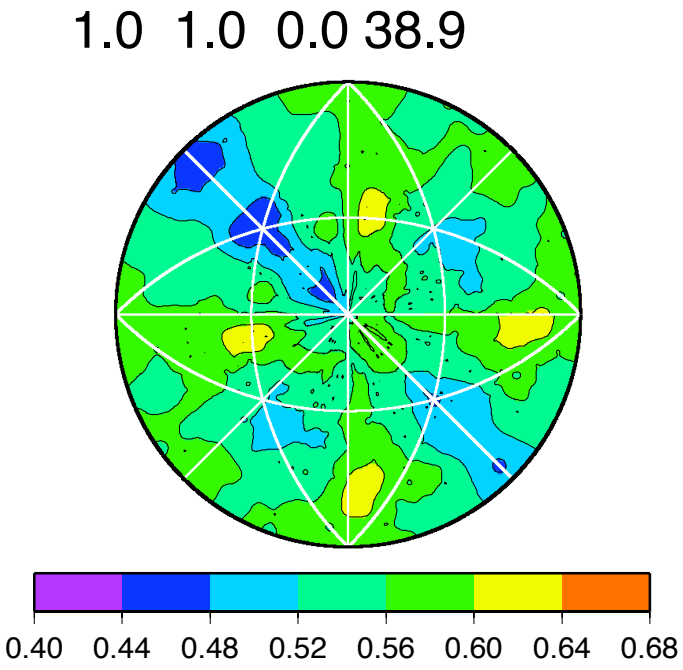

(b)

Figure 3.1: Reconstructed grain boundary energies for nickel for specific misorientations, redrawn from [32] for (a) $60^\circ < 111 >$ and (b) $38.9^\circ < 110 >$. Energies are plotted in arbitrary units (a.u.).

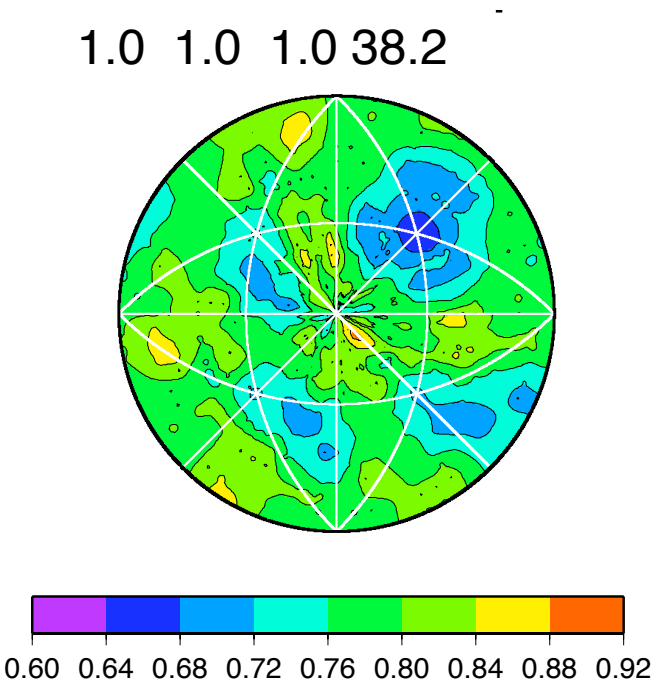

(a)

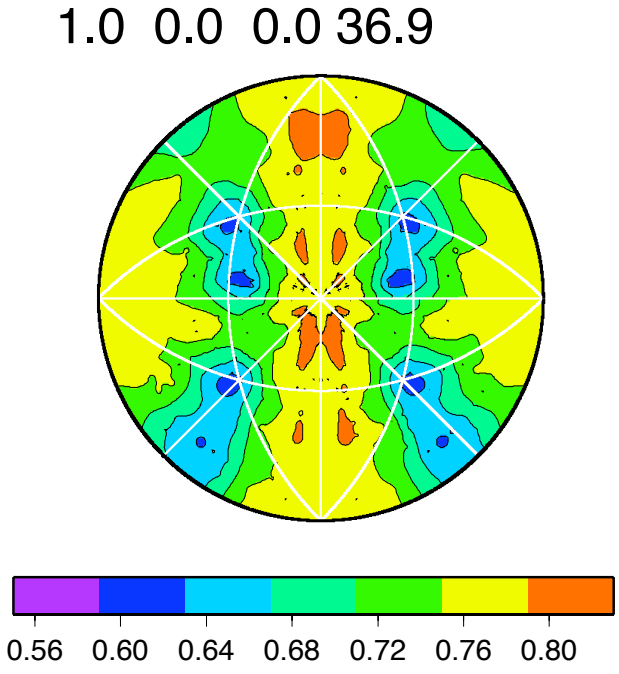

(b)

Figure 3.2: Reconstructed grain boundary energies for nickel for specific misorientations, redrawn from [32] for (a) 38.2° < 111 > and (b) 36.9° < 100 >. Energies are plotted in arbitrary units (a.u.).

a misorientation specified by indices $[c_1, c_2, c_3]$ and a plane normal specified by indices $[c_4, c_5]$. The boundary space is discretized to CD bins for each dimension in misorientation space and $(CD_2, 4CD_2)$ bins in inclination space, so that

$$0 \leq c_1, c_2, c_3 \leq CD \tag{3.1}$$

$$0 \leq c_4 \leq CD_2, 0 \leq c_5 \leq 4CD_2 \tag{3.2}$$

Olmsted et al. calculated absolute energies (in J/m^2) of 388 distinct grain boundary types for face-centred cubic metals (as aluminum and nickel)[49]. In the aforementioned work, a series of molecular-static simulations were performed on bicrystal geometries, where the grain boundary misorientations are limited to CSL types (Σ boundaries) and the boundary normals are rational. At least 72 different Σ boundary types were considered. Embedded-atom potentials were used for reasons of good agreement between experimental and simulated energies of specific GBs. The variation of boundary energies with the boundary plane normal for specific Σ boundaries is plotted in figs. 3.3,3.4. There are 9 bins in each dimension ($CD = 9, CD_2 = 9$). Comparing these with those extracted from orientation mapping observations [32] (as in fig. 3.1), qualitative differences are evident. Only boundary types equivalent to one of the 388 boundaries have been assigned an energy, and the energies of other boundary types are unknown. Details for procedure to fill up the 5-parameter space with energies for the 388 GB types are given in Appendix E - it should be noted that the energy space is sparse as the 388 types (and their crystallographic equivalents) correspond to only a few boundary types. Hence, a method to estimate the energy for an arbitrary boundary type using appropriate metrics is discussed in the present chapter.

We use an alternate representation of grain orientations proposed by Olmsted [48, 49]. The motivation is that the list of GB types with known energies are expressed in Olmsted's representation. A reference configuration is chosen (such as say the lattice vectors of a face-

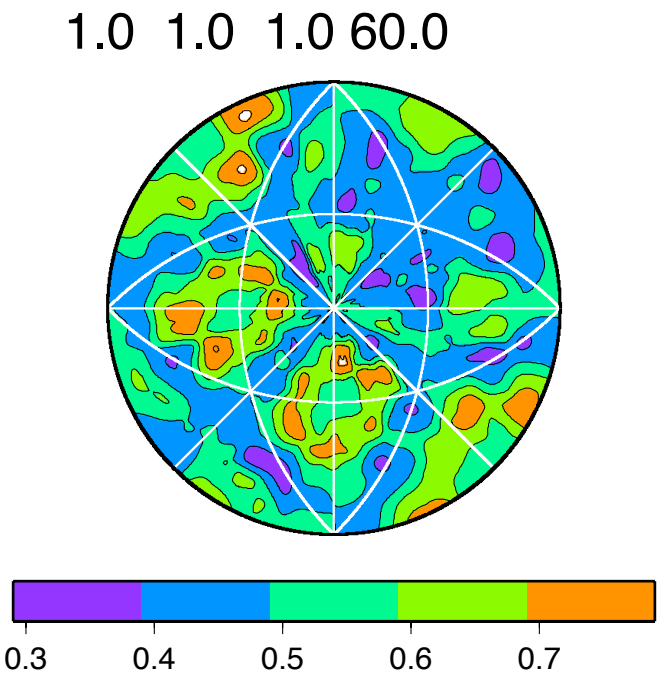

(a)

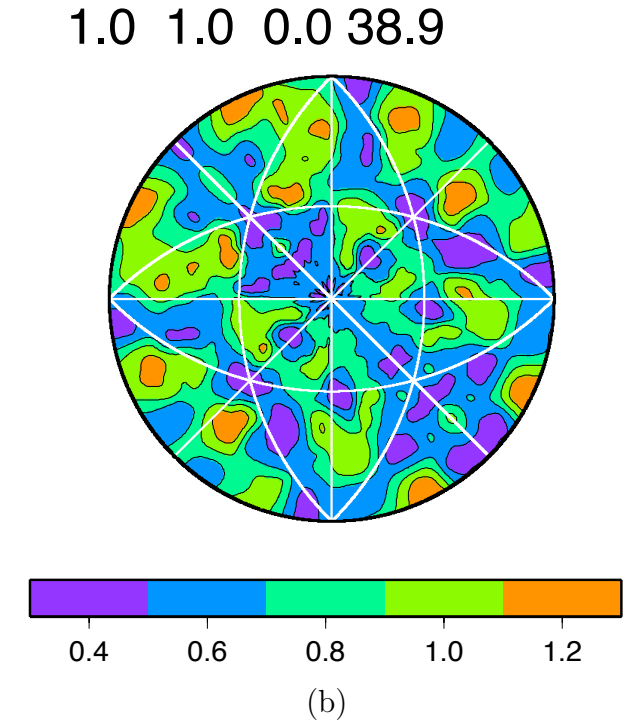

(b)

Figure 3.3: Grain boundary energies for nickel for specific misorientations (a) $60^\circ < 111 >$ and (b) $38.9^\circ < 110 >$ extracted from molecular-static simulations, redrawn from [49]. Energies are expressed in $\frac{J}{m^2}$.

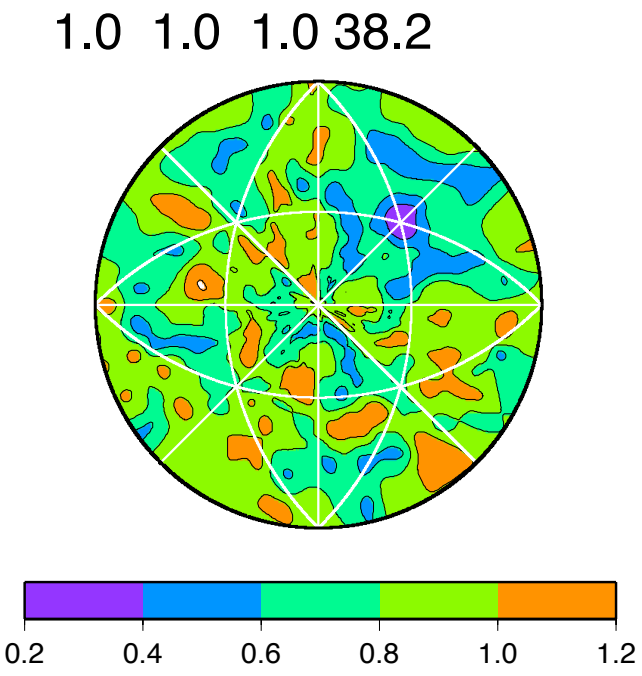

(a)

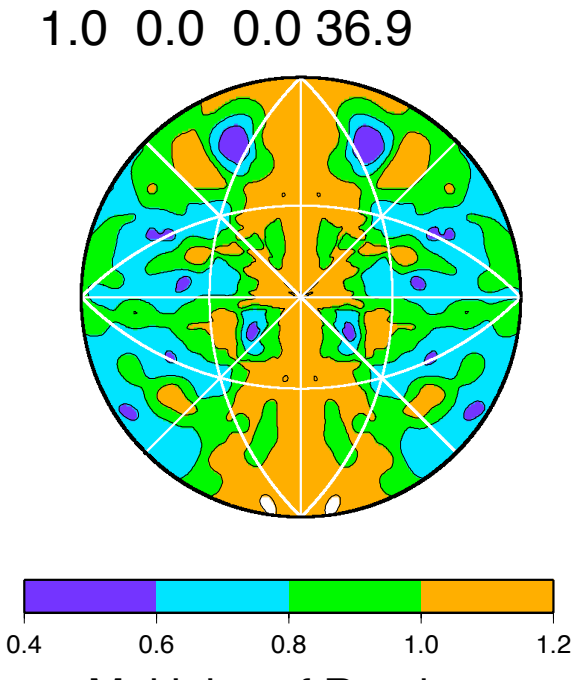

(b)

Figure 3.4: Grain boundary energies for nickel for specific misorientations (a) 38.2° < 111 > and (b) 36.9° < 100 > extracted from molecular-static simulations, redrawn from [49]. Energies are expressed in $\frac{J}{m^2}$.

centred cube) - the metric is defined such that any parametrization of GBs is independent of the particular reference configuration chosen. The plane $z = 0$ is chosen such that it lies along the plane of the grain boundary itself - thus grain A can be defined as the crystal in the region $z < 0$ and grain B as the crystal in $z > 0$. Thus rotation matrices could be calculated which rotate the reference configuration to grain A (and grain B) - these would be denoted (as in [48]) by A and B respectively, and the boundary is represented as (A, B). Note that such a representation for a grain orientation is the inverse of the Bunge representation usually used in texture studies. Such a boundary would have six degrees of freedom (three from each rotation matrix), one of which is redundant. This is because any rotation Z of the grains about $z = 0$, would change the rotation matrices A and B without altering the boundary. This is expressed as $(\mathbf{ZA}, \mathbf{ZB}) = \boldsymbol{(A, B)}$. Also, application of crystal symmetries on the grains $\mathbf{(T_A}$ and $\mathbf{T_B)}$ should not change the boundary, which can be expressed as $(\mathbf{AT_A}, \mathbf{BT_B}) = (\mathbf{A}, \mathbf{B})$.

For each GB type $[c_1, c_2, c_3, c_4, c_5]$ the corresponding (A, B) representation can be found in the following manner. The indices of the grain boundary normal $[n_x.n_y.n_z]$ is calculated as

$$n_x = sin\theta cos\varphi \tag{3.3}$$

$$n_y = sin\theta sin\varphi \tag{3.4}$$

$$n_z = cos\theta \tag{3.5}$$

where, the angles (θ, φ) depend on indices (c_4, c_5) as in

$$\theta = cos^{-1}\left(\frac{c_4}{CD_2}\right) \tag{3.6}$$

$$\varphi = \frac{\pi c_5}{2CD_2} \tag{3.7}$$

The corresponding limits for θ (angle that the normal makes with the [001] axis) and φ (angle between the projection of the boundary normal on the xy plane and the [100] axis) are

$$0 \leq \theta \leq \frac{\pi}{2}, 0 \leq \varphi \leq 2\pi$$

The rotation matrix which transforms $[n_x, n_y, n_z]$ to [001] can be arbitrary fixed as matrix A. Other solutions are possible, but any member can be used as these belong to an *equivalence class* [48]. Note this is an active rotation hence it is the inverse of its corresponding Bunge representation $A' = A^T$. The other rotation matrix B is calculated as $g_B = g_A \triangle g_{AB}$. The disorientation matrix can be determined as

$$\triangle g_{AB} = \begin{bmatrix} cos\phi_1 cos\phi_2 - sin\phi_1 sin\phi_2 cos\Phi & sin\phi_1 cos\phi_2 + cos\phi_1 sin\phi_2 cos\Phi & sin\phi_2 sin\Phi \\ -cos\phi_1 sin\phi_2 - sin\phi_1 cos\phi_2 cos\Phi & -sin\phi_1 sin\phi_2 + cos\phi_1 cos\phi_2 cos\Phi & cos\phi_2 sin\Phi \\ sin\phi_1 sin\Phi & -cos\phi_1 sin\Phi & cos\Phi \end{bmatrix} \tag{3.8}$$

where, the angles (ϕ_1, Φ, ϕ_2) are related to the misorientation indices $[c_1, c_2, c_3]$

$$c_1 = 2 * CD * \phi_1/\pi \tag{3.9}$$

$$c_2 = CD * cos\Phi \tag{3.10}$$

$$c_3 = 2 * CD * \phi_2/\pi \tag{3.11}$$

For each of the 388 boundary types (whose energies are known, refer [49]) the corresponding (C, D) representation is used. Cubic symmetry operators $(O_i, 1 \leq i \leq 24)$ are then applied to each orientation matrix (as in $g_A O_A$) as these are crystallographically equivalent

orientations. One of the advantages of using this representation is the ease of determining the boundary normal, which is simply the first row of the orientation matrix, for example the $\hat{n_A}$ is (here $i = 1, j = 1$)

$$n_{xA} = g_A O_A(i, j) \tag{3.12}$$

$$n_{yA} = g_A O_A(i, j+1) \tag{3.13}$$

$$n_{zA} = g_A O_A(i, j+2) \tag{3.14}$$

Now an appropriate metric needs to be chosen to calculate the distance between an arbitrary boundary type (A, B) and each of the 388 boundary types (and their crystallographic equivalents) whose energies are known, represented as (C, D). The energy of its closest boundary $(C, D)_{d=d_{min}}$ is then assigned to boundary$(\mathbf{A}, \mathbf{B})$.

3.2.2 Interpolated energies using Morawiec's metric

A metric devised by Morawiec [43] is used to calculate distance between two grain boundary types. The metric accounts for closeness both in misorientation and inclination space. Equal weights are assigned to distances in misorientation and inclination space. It is to be noted that this uniform weightage is arbitrary, and unequal weights might be assigned for distances in misorientation and inclination space [7], which will result in different interpolated energies. This arbitrariness of combining distances to obtain a net distance (in boundary space) is a serious disadvantage of using this metric.

Suppose one wishes to determine the closeness of two arbitrary boundary types (specified by (g, n) and (g', n'), a representation used by Morawiec) - where g and n denote boundary misorientation and plane normal in crystal reference frame respectively. The distance in boundary space can be expressed as eq.3.15.

$$\chi^2 = 5 - tr(g^T g') - n.n' - (g^T n).(g'^T n') \tag{3.15}$$

here $tr(g)$ represents the trace of the $3X3$ rotation matrix g, which is simply the sum of the diagonal elements

$$tr(g) = \sum_{i=1}^{3} g[i,i] \tag{3.16}$$

and $n.n'$ the dot product of the two boundary normals

$$n.n' = \sum_{i=1}^{3} n_i n'_i \tag{3.17}$$

where n_i denotes the ith component of boundary normal n .

In terms of the (A, B) representation the misorientation for boundaries (A, B) and (C, D) is given by $\triangle g_{AB}$ and $\triangle g_{CD}$ respectively

$$\triangle g_{AB} = (g_A O_A)^T g_B O_B \tag{3.18}$$

$$\triangle g_{CD} = (g_C O_C)^T g_D O_D \tag{3.19}$$

here for each symmetry operator O_{gi}, $1 \leq i \leq 24$ - all crystallographically equivalent boundaries have equal energies.

The corresponding distances in misorientation space $\chi^2_{\triangle g}$ and inclination space χ^2_n and the net distance χ^2 in boundary space can be expressed as

$$\chi^2_{\triangle g} = 3 - tr\left((\triangle g_{AB})^T \triangle g_{CD}\right) \tag{3.20}$$

$$\chi^2_n = 2 - n_A.n_C - n_B.n_D \tag{3.21}$$

$$\chi^2 = \chi^2_{\triangle g} + \chi^2_n \tag{3.22}$$

For each boundary of arbitrary type (A, B) the distance to each of the 388 boundaries (represented as (C, D)) is calculated. An energy value corresponding to its closest (C, D) boundary is assigned to (A, B). Mathematically this can be expressed as eq. 3.23.

$$\gamma_{(A,B),i} = \gamma_{(C,D),j}, \chi^2_{i,j} = min[\chi^2_{i,k}, 1 \leq k \leq N] \tag{3.23}$$

where N denotes the number of boundary types with known energies. This process is repeated for each arbitrary GB type in boundary space - since the boundary space is discretized into (CD, CD, CD) bins in misorientation space and $(CD_2, 4CD_2)$ bins in inclination space, this corresponds to $4.CD^3.CD_2^2$ boundary types, not all of which are distinct GB types. In figs. 3.5,3.6 the interpolated energies for specific values of misorientation are shown, for $CD = 9, CD_2 = 9$.

3.2.3 Interpolated energies using Olmsted's metric

Morawiec's metric [43] suffers from an inherent arbitrariness - as separate distances are calculated in misorientation space and inclination space, corresponding weights have to be chosen to combine them to derive a distance χ^2 in boundary space. This is expressed below for convenience

$$\chi^2 = 5 - tr(g^T g') - n.n' - (g^T n).(g'^T n') \tag{3.24}$$

where, $tr(g)$ denotes the trace of rotation matrix g and $n.n'$ the dot product of boundary normals n and n'. In eq. 3.24 equal weights have been assigned to distances in inclination and misorientation space. One can choose unequal weights for these distances, and expect different interpolated energies.

Recently Olmsted proposed an alternate metric based on his representation of grain boundaries described in a companion paper [48, 49]. The distance between boundary types (A, B) and (C, D) is simply expressed as in eq. 3.25

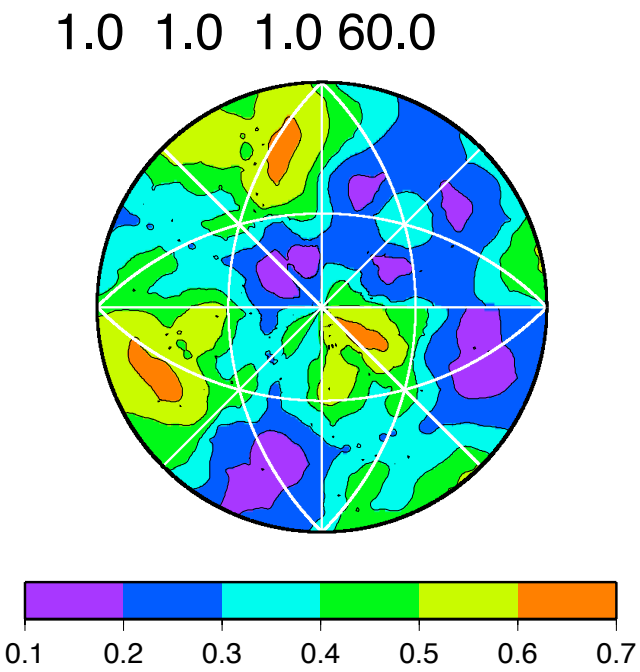

(a)

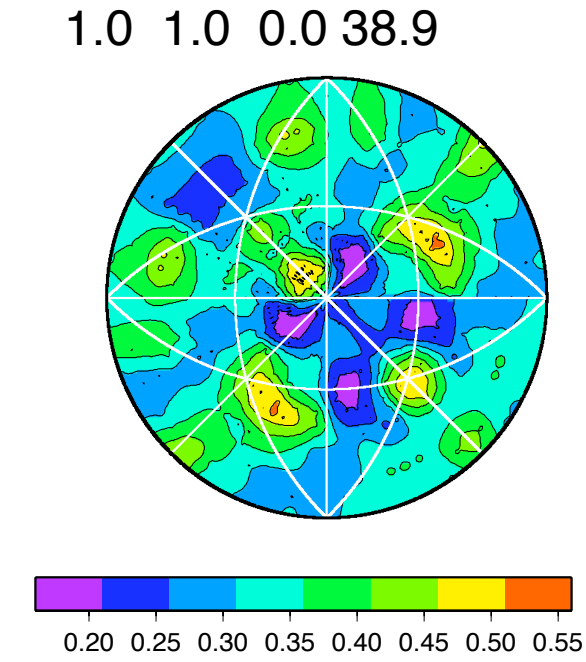

(b)

Figure 3.5: Interpolated energies for specific misorientations in nickel, using Morawiec's distance metric for (a) $60^\circ < 111 >$ and (b) $38.9 < 100 >$. Energies are expressed in $\frac{J}{m^2}$.

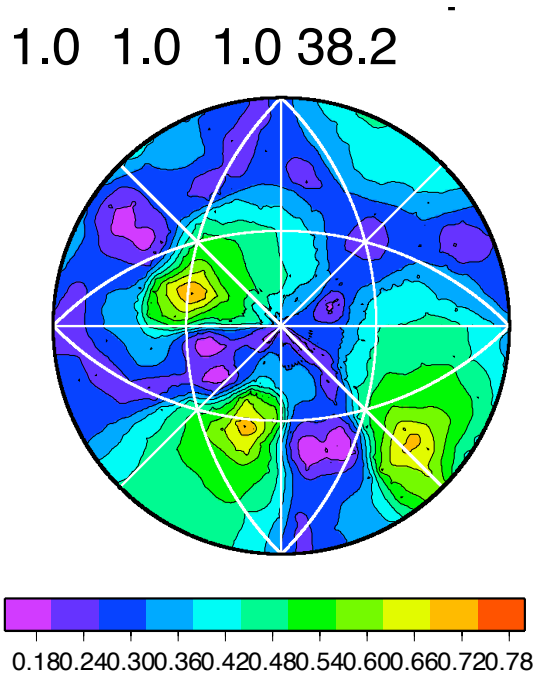

(a)

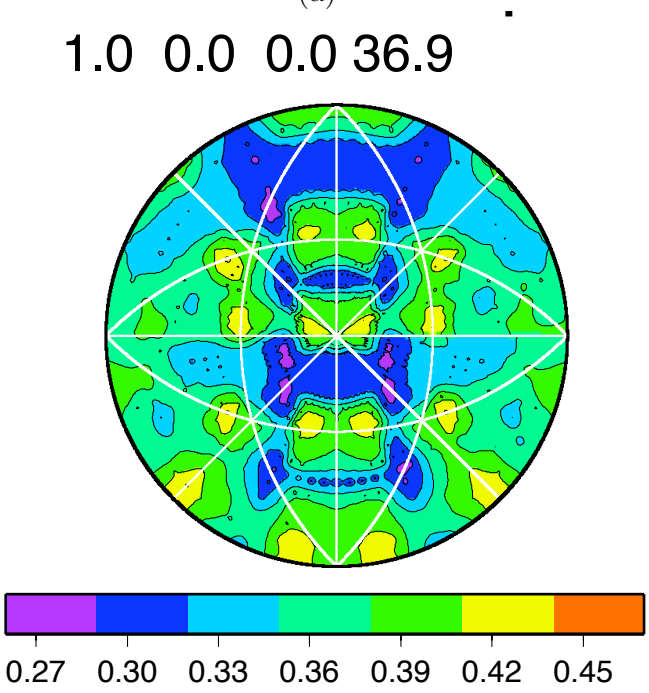

(b)

Figure 3.6: Interpolated energies for specific misorientations in nickel, using Morawiec's distance metric for (a) $38.2^{\circ} < 111 >$ and (b) $36.9 < 100 >$. Energies are expressed in $\frac{J}{m^2}$. Comparing these (and fig. 3.5) with figs.3.1,3.2 significant qualitative differences can be observed, both in terms of the range and distribution of boundary energies.

$$d = \sqrt{2}\sqrt{3 - tr((\mathbf{g_A O_A})^{\mathbf{T}}\,\mathbf{g_C O_C}) + 3 - tr((\mathbf{g_B O_B})^{\mathbf{T}}\,\mathbf{g_D O_D})} \tag{3.25}$$

here, each of the symmetry operators O_{gi} ($g = A$, B, C or D) should vary independently for $1 \leq i \leq 24$.

Since in this representation of grain buondaries, a rotation about $z = 0$ does not change the boundary, a minimization routine should be used (refer Appendix B in **(author?)** [48]). The distance d can be modified to

$$\begin{aligned} a &= 6 - [F_1(A,C) + F_1(B,D)] && (3.26)\\ b &= F_2(A,C) + F_2(B,D) && (3.27)\\ c &= F_3(A,C) + F_3(B,D) && (3.28)\\ d &= a - \sqrt{b^2 + c^2} && (3.29) \end{aligned}$$

here $F_i(A,C)$ is given by

$$\begin{aligned} F_1(A,C) &= (g_A O_A)^T_{i3}(g_C O_C)_{3i} && (3.30)\\ F_2(A,C) &= (g_A O_A)^T_{i1}(g_C O_C)_{1i} + (g_A O_A)^T_{i2}(g_C O_C)_{2i} && (3.31)\\ F_3(A,C) &= (g_A O_A)^T_{i2}(g_C O_C)_{1i} - (g_A O_A)^T_{i1}(g_C O_C)_{2i} && (3.32) \end{aligned}$$

In his paper, Olmsted showed that this definition of distance was able to capture differences in boundary plane inclination (at a constant misorientation). The particular case of $\Sigma 3$ misorientation was chosen for illustration where coherent $< 111 >$ planes exhibited a significantly lower energy with respect to other boundary inclinations [48].

The distance between boundary of arbitrary type$(\mathbf{A}, \mathbf{B})$ (for which we need to determine a boundary energy) and boundary $(\mathbf{C}, \mathbf{D})$ (here $(\mathbf{C}, \mathbf{D})$ belongs to the set of boundaries for

which energies were determined through molecular-static simulations [49], $N = 388$ in the expression below) can be calculated using eqs.3.25,3.29. The energy of its closest boundary is then assigned to boundary $(\mathbf{A}, \mathbf{B})$.

$$\gamma_{(\mathbf{A},\mathbf{B})} = \gamma_{(\mathbf{C},\mathbf{D})_\mathbf{k}}, \chi_k = min\left\{\chi_j, 1 \leq j \leq N\right\} \tag{3.33}$$

$$\chi_j = min(d_{(A,B),(C,D)O_{gi}}, 1 \leq i \leq 24) \tag{3.34}$$

$$d_{(A,B),(C,D)O_{gi}} = a - \sqrt{b^2 + c^2} \tag{3.35}$$

as before, each of the symmetry operators $O_{gi}(g = A, B, C, D)$ should vary independently for $1 \leq i \leq 24$. This process is repeated for each arbitrary GB type in boundary space - since the boundary space is discretized into (CD, CD, CD) bins in misorientation space and $(CD_2, 4CD_2)$ bins in inclination space, this corresponds to $4.CD^3.CD_2^2$ boundary types, not all of which are distinct GB types. In figs. 3.7,3.8 the interpolated energies for specific values of misorientation are shown, for $CD = 9, CD_2 = 9$ (9 bins in each dimension).

3.2.4 Correlating boundary populations with interpolated energies

A set of simulations are performed in three dimensions on a 160-cubed domain (initially populated with 1000 grains and assigned a random texture), with interpolated energies derived using Olmsted's metric. Details for incorporating interpolated energies in the interface-field framework can seen in Appendix C. Boundary populations are extracted at an intermediate timestep $t = 3000$ and are plotted in figs. 3.9-3.12. The anisotropy in these distributions should be compared to the anisotropy in interpolated energies (interpolated energies for specific misorientations are redrawn for comparison). An inverse relation between boundary energy and population seems to develop, see the peaks at $< 111 >$ for 60° and 38.2° disorientations for instance. These distributions (extracted from simulations) are compared to those extracted using experimental techniques (orientation mapping of two-dimensional sections

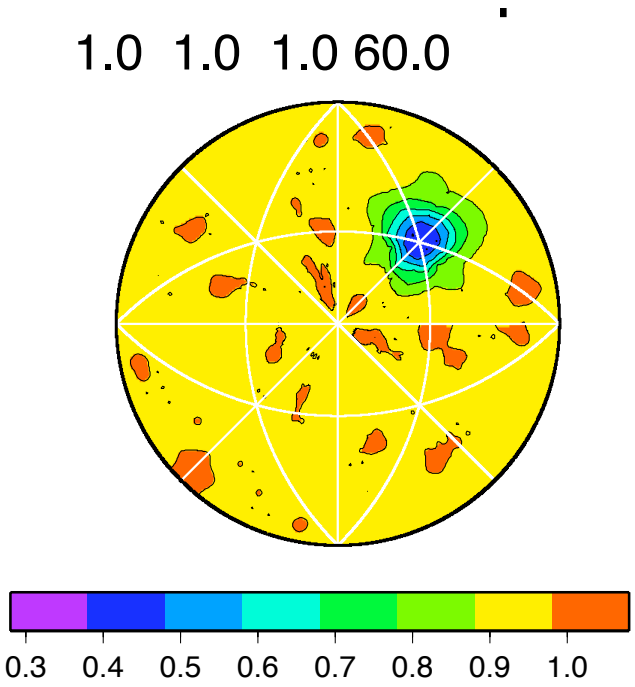

(a)

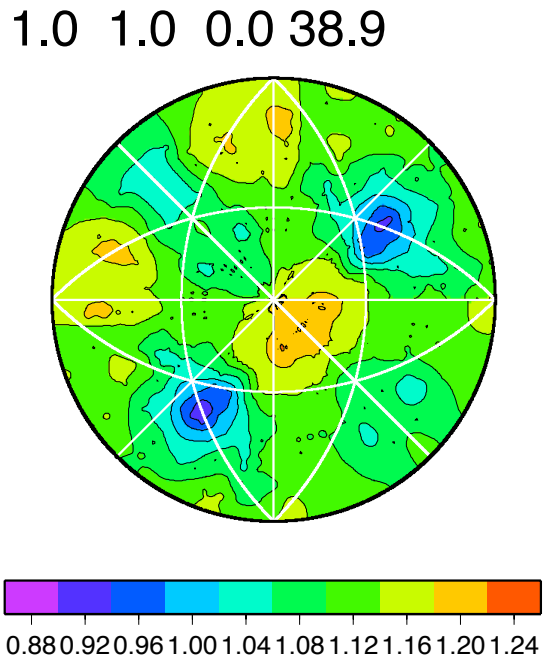

(b)

Figure 3.7: Interpolated energies for specific misorientations in nickel, using Olmsted's distance metric for misorientations (a) $60^\circ < 111 >$ and (b) $38.9^\circ < 110 >$. Energies are expressed in $\frac{J}{m^2}$.

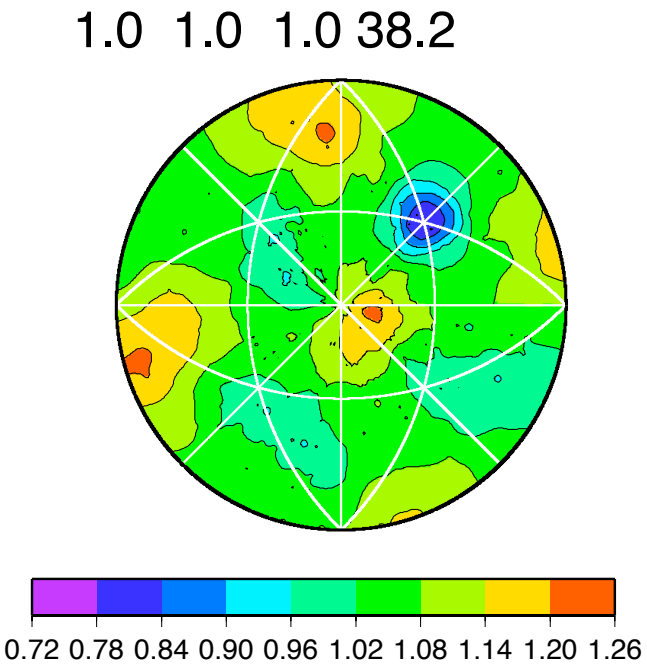

(a)

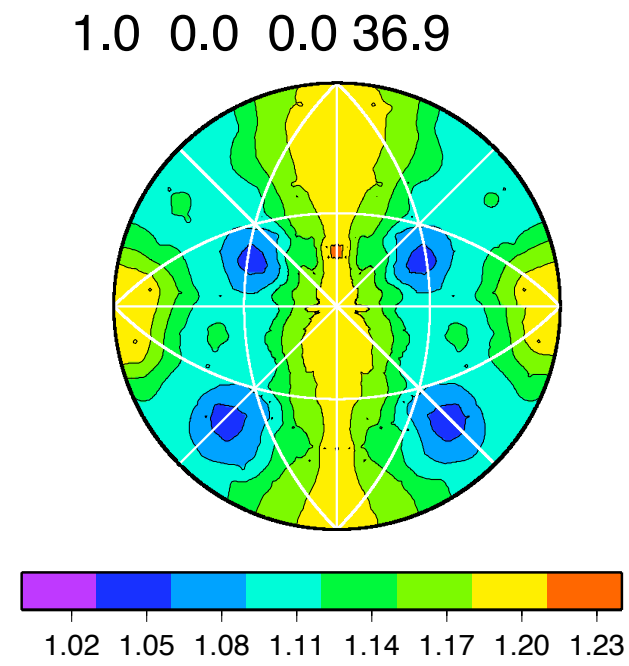

(b)

Figure 3.8: Interpolated energies for specific misorientations in nickel, using Olmsted's distance metric for misorientations (a) $38.2^\circ < 111 >$ and (b) $36.9^\circ < 100 >$. Energies are expressed in $\frac{J}{m^2}$. Comparing these (and fig. 3.7) with figs.3.1, 3.2 it can be observed that they are qualitatively similar.

of nickel [32]), see figs. 3.13,3.14 - these are qualitatively similar to each other. In fig. 3.15 the variation of boundary population (over all misorientations) is plotted with boundary energy to demonstrate that the inverse relation holds true across all boundary types. There is significant scatter due to insufficient statistics, which is expected to scale down as larger number of grains are evolved for longer times.

3.3 Conclusion

Interpolated energies obtained through the use of Olmsted's distance function better correlate with the boundary energies extracted through orientation mapping of nickel. An inverse relation between interpolated energies and populations is observed that supports the notion that low-energy boundaries increase (in area and in number) at the expense of high-energy ones. These distributions (extracted from three-dimensional simulations) show a direct scaling with distributions collected using experimental methods (orientation mapping), demonstrating the capability of the present method to model the development of anisotropic boundary character in real materials. The inverse relation between boundary energy and population at a fixed misorientation is not strictly one-to-one. A similar observation was noted by Gruber (*PhD thesis, 2007*), and can be attributed to the effect of torque terms present when the boundary energy is inclination-dependent, which are avoided in the present formulation. Also certain GB types (such as the $\Sigma 3$) show much lower intensities than experimentally observed - this is because these boundaries correspond to annealing twins, and are not a direct consequence of grain growth. Hence, in fcc metals as nickel, the physical phenomena of grain growth cannot completely account for the significantly high population of certain boundary types.

The present method also provides a formulation to model anisotropic boundary migration in other fcc materials (as aluminium) as the grain boundary energies in different face-centred cubic metals vary with boundary type in a relative fashion [49]. These interpolated energies

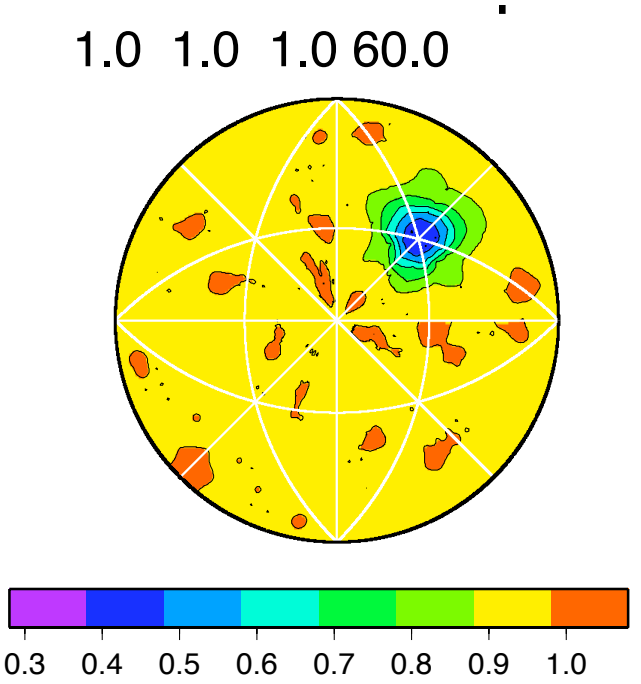

(a)

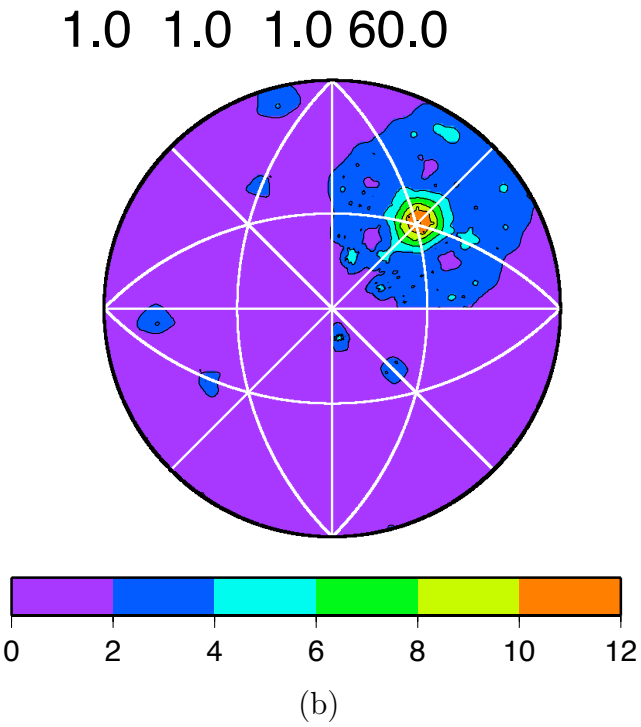

(b)

Figure 3.9: Boundary energies (a) plotted with boundary population (b) for misorientation $60^\circ < 111 >$. Simulations are performed on a 160-cubed domain and evolved for $t = 3000$ steps. Populations are expressed in Multiples of Random Distribution (MRD) and energies in $\frac{J}{m^2}$.

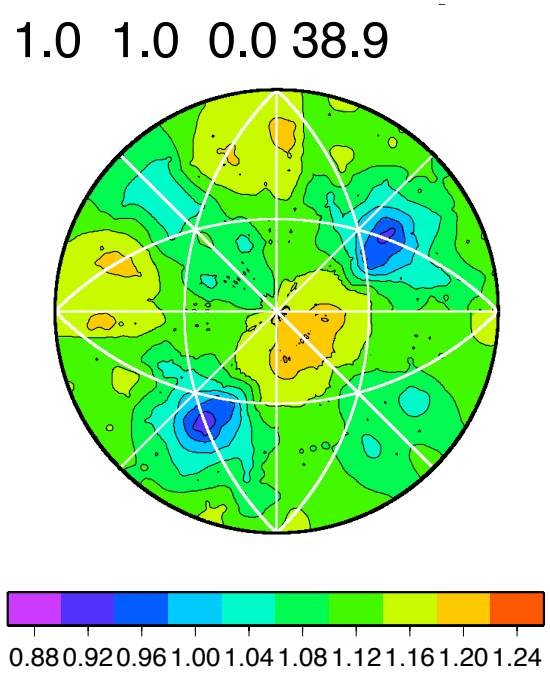

(a)

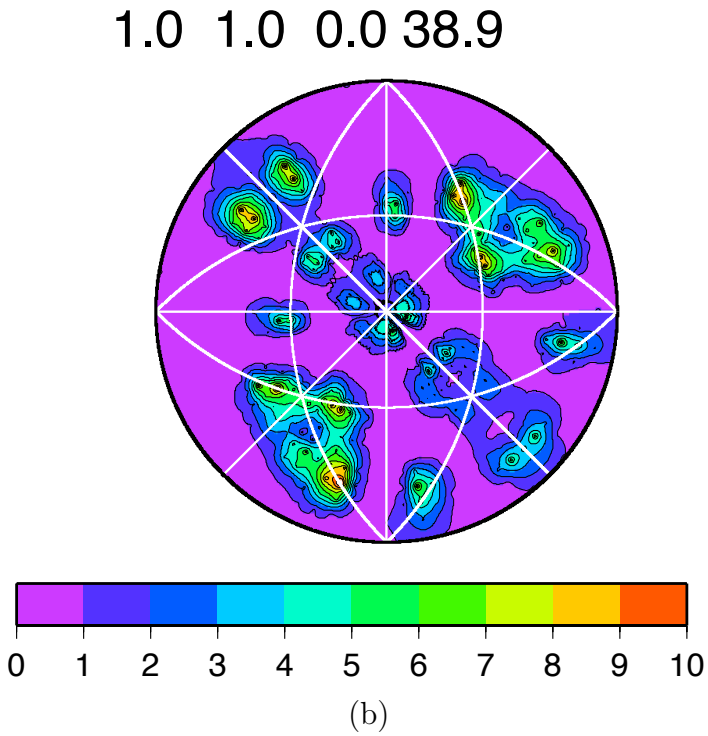

(b)

Figure 3.10: Boundary energies (a) plotted with boundary population (b) for misorientation $38.9° < 110 >$. Simulations are performed on a 160-cubed domain and evolved for $t = 3000$ steps. Populations are expressed in Multiples of Random Distribution (MRD) and energies in $\frac{J}{m^2}$.

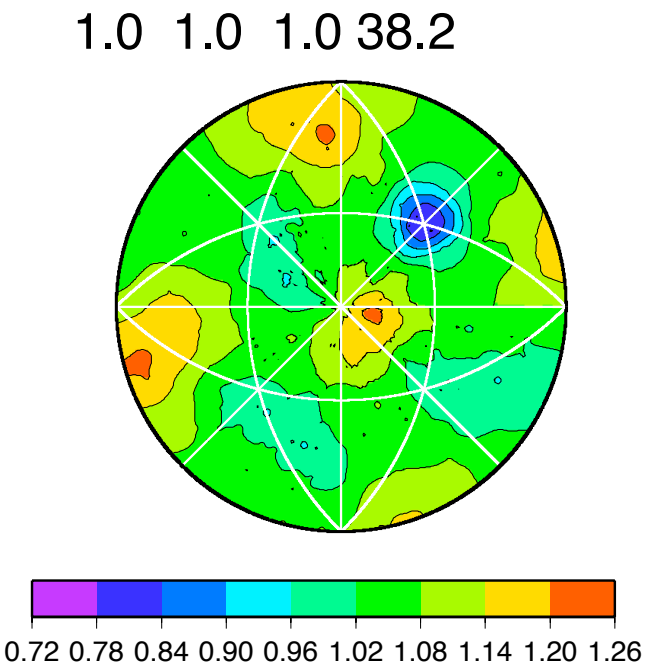

(a)

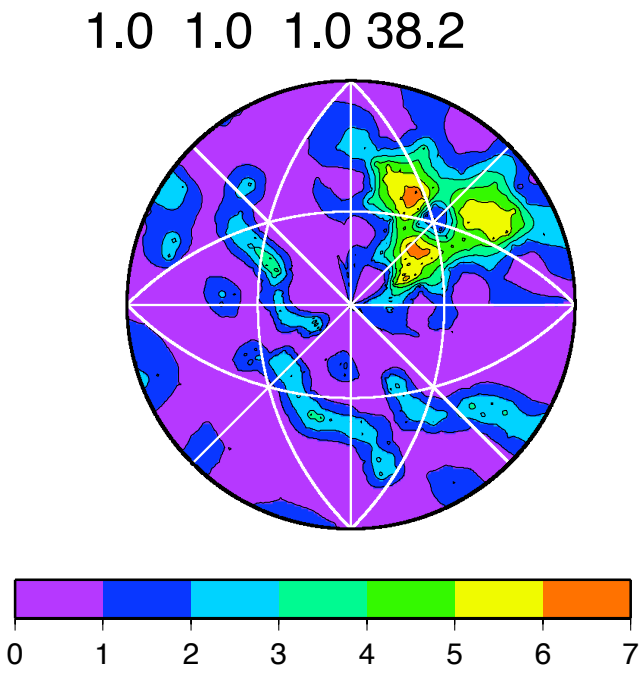

(b)

Figure 3.11: Boundary energies (a) plotted with boundary population (b) for misorientation $38.2^\circ < 111 >$. Simulations are performed on a 160-cubed domain and evolved for $t = 3000$ steps. Populations are expressed in Multiples of Random Distribution (MRD) and energies in $\frac{J}{m^2}$.

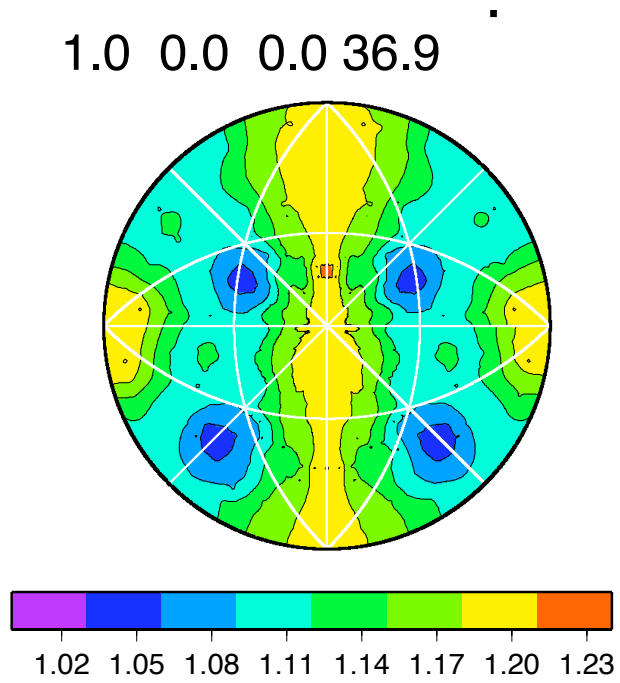

(a)

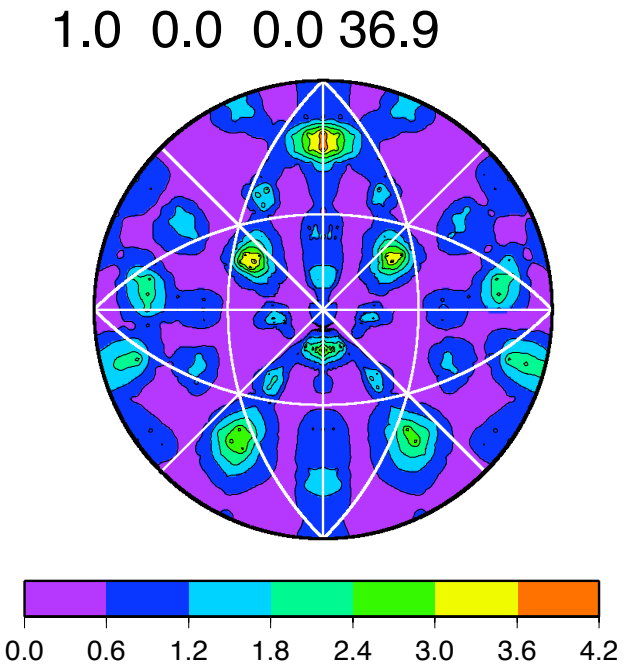

(b)

Figure 3.12: Boundary energies (a) plotted with boundary population (b) for misorientation $36.9° < 100 >$. Simulations are performed on a 160-cubed domain and evolved for $t = 3000$ steps. Populations are expressed in Multiples of Random Distribution (MRD) and energies in $\frac{J}{m^2}$. Note that low-energy boundaries are more populated than higher energy ones, such that energy and population are inversely related.

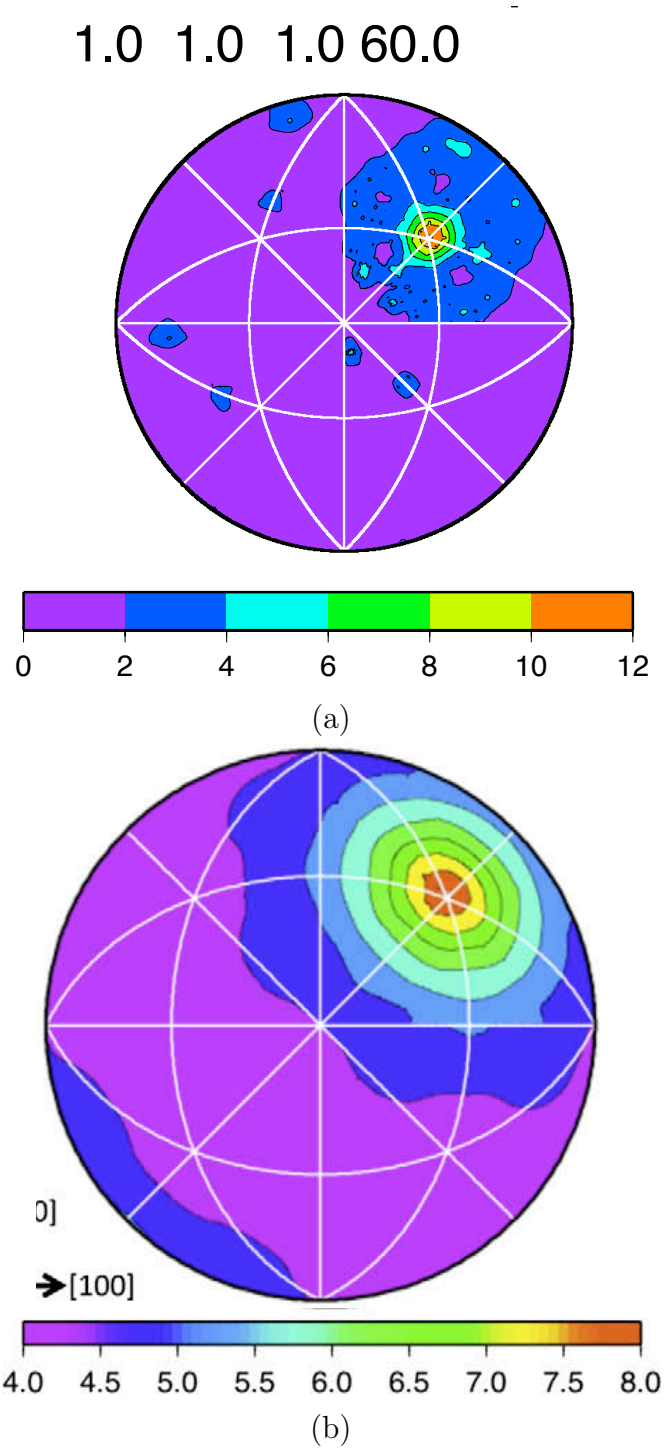

Figure 3.13: (a) Boundary populations at misorientation $60^\circ < 111 >$ from simulations performed in three dimensions on a 160-cubed domain evolved for $t = 3000$ with interpolated energies derived using Olmsted's metric (as in fig. 3.7). These should be compared with boundary populations at these misorientations (plotted in (b)) collected using orientation mapping of plane sections of nickel (reproduced from [32]). Populations are plotted in MRD. Note that (b) is expressed as the natural logarithm of the population, hence the peak at $< 111 >$ is much stronger in (b) compared to (a).

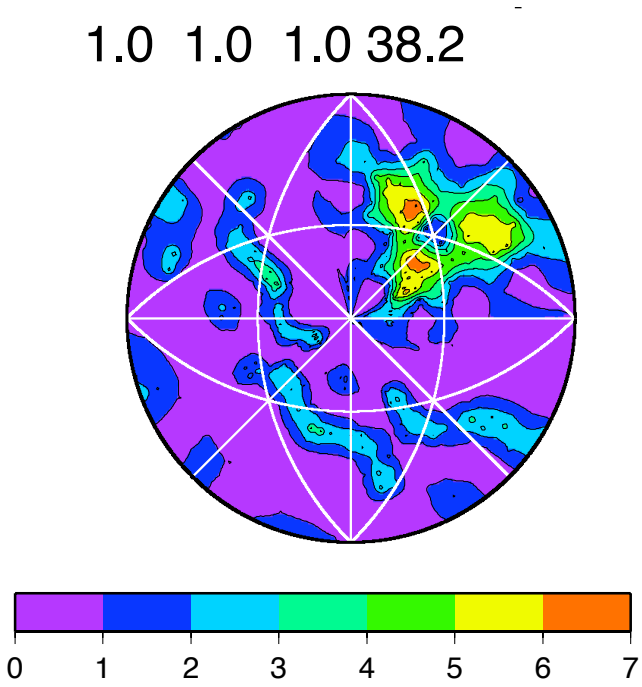

(a)

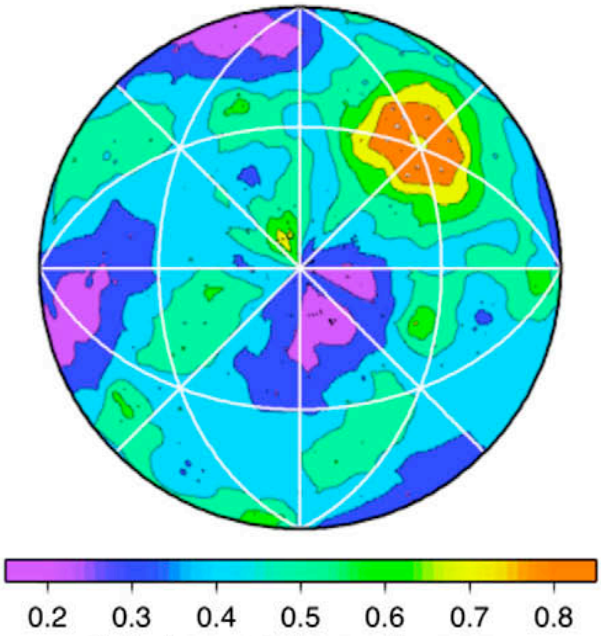

(b)

Figure 3.14: (a) Boundary populations at misorientations $38.2^\circ < 111 >$ from simulations performed in three dimensions on a 160-cubed domain evolved for $t = 3000$ with interpolated energies derived using Olmsted's metric (as in figs. 3.8). These should be compared with boundary populations at these misorientations (as in (b)) collected using orientation mapping of plane sections of nickel (reproduced from [32]). Populations are plotted in MRD.

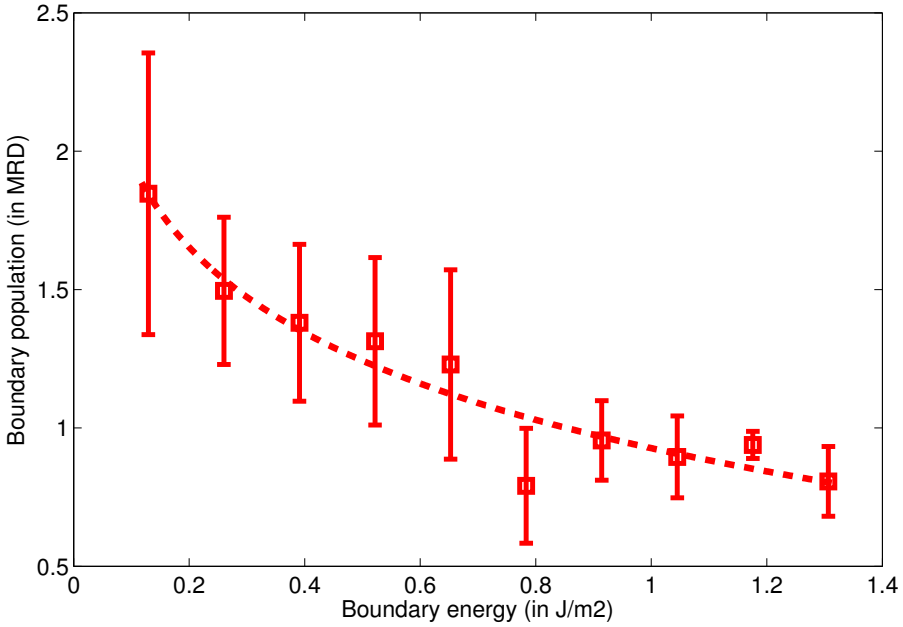

Figure 3.15: Variation of boundary population (expressed in MRD) with boundary energy (expressed in $\frac{J}{m^2}$). Note that on an average (across all boundary types) there are more (and longer) low-energy boundaries than high-energy ones though there is significant scatter due to insufficient statistics.

can be directly used in the interface-field framework to predict boundary motion and microstructure evolution in real materials. Initial texture and grain structure (flat boundaries have low boundary velocities and persist during grain growth) have a significant influence on the development of anisotropic boundary character. Assuming that one has information about the initial texture and microstructure, the interpolated energies can be used in simulations to better predict the development of anisotropic boundary character in such materials.

Chapter 4

Future work

As mentioned before, the present phase-field formulation does not account for the grain boundary torques which are non-zero for an inclination-based anisotropy. Hence a possible direction to venture is to reformulate the governing equations of motion, so as to incorporate a complete five-parameter description of anisotropic boundary properties in the present framework. To this end, the governing equations are reformulated as described in the adjoining Appendix A. Note that inclination dependence in three dimensions is more complicated than in two dimensions, and both cases have to be treated accordingly. Techniques for numerical implementation are described briefly in Appendix B. In Appendix D, details for the energy extension procedure, which extends anisotropic energies along grain boundaries to boundary junctions, are given (thanks to a private commuciation with Seth Wilson).

The present formulation can be adapted to study microtructure evolution in real material systems which exhibit significant anisotropy in boundary populations (as nickel [32] or magnesia [57]). Experimental techniques as orientation mapping (combined with serial sectioning) and tomography make it possible to extract orientation information from such metallic and ceramic specimens. Instead of using a simplistic description of anisotropy (as the four-fold anisotropy function in two dimensions (eq.2.10) or the cubic harmonics (eq.2.13) in three dimensions), one can use an interpolation technique to determine the energy of

an arbitrary grain-boundary type, given that energies of certain boundary types have been derived experimentally (Li et al. [32]) or estimated through simulations (Olmsted et al. [49]). This has been discussed in some detail in Chapter 3. Details for using interpolated boundary energies in the present framework are described in Appendix C. Also suitable parameters to compare extracted distributions (from simulations) and distributions collected from experimental observations have to be chosen to determine quantitatively how close these distributions are over the entire range of grain boundary types.

Starting from an initial state (a microstructural repesentation of nickel, or of an intermetallic such as Cu-Nb, prior to annealing), one can use the aforementioned interpolated boundary energies and compare the motion of boundaries as predicted by simulations to those observed experimentally, after annealing and subsequent grain growth. So that time scales (between experimental observations and model predictions) match, a series of simulations needs to be performed, with increasing magnitude of boundary anisotropy, and the corresponding grain maps compared to experimental observations. Possible parameters of comparison include but are not limited to misorientation between corresponding points or cells and extracted grain boundary character distributions. Time scales and anisotropy strengths match when the difference between experimental and simulated domains is a minimum, as in

$$t_{sim} = t_{real}, \varepsilon_{sim} = \varepsilon_{real}, \tilde{\Delta g}(t_{sim}, \varepsilon_{sim}) \leq \tilde{\Delta g}(t, \varepsilon) \forall t, \varepsilon \tag{4.1}$$

where, Δg is the misorientation difference between simulated and experimental domains, collected for corresponding cells (or points), and averaged over the entire domain Ω.

$$\tilde{\Delta g} = \frac{\sum \Delta g(x_i)}{N}, 1 \leq i \leq N \tag{4.2}$$

where the domain Ω can be divided into N discrete cells.

It is predicted that an optimal combination of the different boundary energy descriptors

should result in better estimation of grain boundary populations in anisotropic systems. Large-scale simulations made possible through parallelization of the code should result in generation of statistically reliable data. The present model hence provides a framework to predict evolution of grain boundary character distributions in real materials, both in two and three dimensions, and hence makes it feasible to derive correlations between boundary properties and populations for such systems.

Appendix A

Time-dependent Ginzburz Landau (TDGL) equations with an inclination dependent anisotropy

As stated previously, the gradient and potential energy terms are expressed as (identical to Steinbach et al. [63])

$$f_{jk}^{gr} = -\frac{\varepsilon_{jk}}{2}\nabla\phi_j.\nabla\phi_k \tag{4.3}$$

$$f_{jk}^{pot} = \gamma_{jk}\left|\phi_j\right|\left|\phi_k\right| \tag{4.4}$$

Let us consider the case of two dimensions for simplicity, where the anisotropic functions for the gradient and potential energy prefactors (ε and γ respectively) vary with the inclination angle (θ) with a reference axis (x axis).

$$\varepsilon_{jk} = \varepsilon(\theta) \tag{4.5}$$

$$\gamma_{jk} = \gamma(\theta) \tag{4.6}$$

Both the prefactors should have a similar variation with inclination, to ensure that the

interface width (w) stays constant irrespective of the variation of boundary energy with inclination [34]. Hereafter $\varepsilon_{jk}(\theta)$ and $\gamma_{jk}(\theta)$ are represented by ε and γ for simplicity.

The TDGL governing equation for deriving changes in field variables can be expressed as

$$\tau_{jk}\dot{q}_{jk} = \left(\nabla\frac{\partial}{\partial\nabla\phi_j} - \frac{\partial}{\partial\phi_j}\right)\left(f_{jk}^{gr} + f_{jk}^{pot}\right) = (a) + (b) - (c) - (d) \tag{4.7}$$

where, term (a) $\left(\nabla\frac{\partial}{\partial\nabla\phi_j}f_{jk}^{gr}\right)$ is evaluated as below. Note that instead of providing a complete derivation, intermediate key terms are calculated and consequent expressions are shown.

$$\nabla\frac{\partial}{\partial\nabla\phi_j}f_{jk}^{gr} = -\frac{1}{2}\frac{\partial}{\partial x_i}\left(\varepsilon\nabla\phi_k + \nabla\phi_j.\nabla\phi_k\frac{\partial\varepsilon}{\partial(\partial_{x_i}\phi_j)}\right) \tag{4.8}$$

Here, the gradient operator ∇ denotes differentiation over all reference axes (x and y in two dimensions) as in $\nabla = \left(\frac{\partial}{\partial x}, \frac{\partial}{\partial y}\right) = \partial_{x_i}$.

The inclination angle θ depends on the gradients of the field variable in x and y directions (ϕ_{jx} and ϕ_{jy} respectively). Hereafter the subscripts x and y will denote differentiation with respect to x and y respectively.

$$tan\theta = \frac{\phi_{jy}}{\phi_{jx}} \tag{4.9}$$

Intermediate terms which emerge during treatment of term (a) (eq.4.8) are shown below

$$\partial_{x_i}\varepsilon = \left(\frac{\varepsilon_\theta}{\phi_{jx}^2 + \phi_{jy}^2}\right)(\phi_{jx}\phi_{jyy} - \phi_{jy}\phi_{jxx})$$

$$\partial_{x_i}\nabla\phi_k = \nabla^2\phi_k = \triangle\phi_k$$

$$\partial_{x_i}(\nabla\phi_j.\nabla\phi_k) = \nabla^2\phi_j\nabla\phi_k + \nabla^2\phi_k\nabla\phi_j = \triangle\phi_j\nabla\phi_k + \triangle\phi_k\nabla\phi_j$$

$$\frac{\partial\theta}{\partial(\partial_{x_i}\phi_j)} = \frac{\phi_{jx} - \phi_{jy}}{\phi_{jx}^2 + \phi_{jy}^2}$$

the variation of the potential energy f_{jk}^{pot} with the field variable ϕ_j (term (d) in eq.4.7) is evaluated as below

$$\frac{\partial}{\partial\phi_j} f_{jk}^{pot} = \gamma\,|\phi_k| + |\phi_j|\,|\phi_k|\,\gamma_\theta \frac{\partial\theta}{\partial\phi_j} \tag{4.10}$$

where $\frac{\partial\theta}{\partial\phi_j} = \left(\frac{\phi_{jyy}\left(\frac{\phi_{jx}}{\phi_{jy}}\right) - \phi_{jxx}\left(\frac{\phi_{jy}}{\phi_{jx}}\right)}{\phi_{jx}^2+\phi_{jy}^2}\right)$; similarly, term (b) $\left(\nabla\frac{\partial}{\partial\nabla\phi_j} f_{jk}^{pot}\right)$ can be expressed as

$$\nabla\frac{\partial}{\partial\nabla\phi_j}\left(\gamma\,|\phi_j|\,|\phi_k|\right) = |\phi_j|\,|\phi_k|\,\nabla\frac{\partial}{\partial\nabla\phi_j}\gamma \tag{4.11}$$

since, $\nabla\frac{\partial}{\partial\nabla\phi_j}|\phi_j|\,|\phi_k| = 0$ and $\left(\frac{\partial\theta}{\partial(\partial_{x_i}\phi_j)} = \frac{\phi_{jx}-\phi_{jy}}{\phi_{jx}^2+\phi_{jy}^2}\right)$

$$\nabla\frac{\partial}{\partial\nabla\phi_j} f_{jk}^{pot} = |\phi_j|\,|\phi_k|\,\nabla\left(\gamma_\theta\frac{\phi_{jx} - \phi_{jy}}{\phi_{jx}^2 + \phi_{jy}^2}\right) \tag{4.12}$$

The primary term of interest in the above expression $\nabla\theta$ can be derived to be

$$\nabla\theta = \partial_{x_i}\theta = \frac{\phi_{jx}\phi_{jyy} - \phi_{jy}\phi_{jxx}}{\phi_{jx}^2 + \phi_{jy}^2}$$

Eventually, term (c) $\left(\frac{\partial}{\partial\phi_j}\left(\frac{\varepsilon}{2}\nabla\phi_j\nabla\phi_k\right)\right)$, the variation of gradient energy f_{jk}^{gr} with field variable ϕ_j is evaluated to be

$$\frac{\partial}{\partial\phi_j} f_{jk}^{gr} = \frac{\nabla\phi_j\nabla\phi_k}{2}\varepsilon_\theta\frac{\partial\theta}{\partial\phi_j} \tag{4.13}$$

since, $\frac{\partial}{\partial\phi_j}\left(\nabla\phi_j\nabla\phi_k\right)$is identical to zero.

The term of interest $\frac{\partial\theta}{\partial\phi_j}$ is derived to be

$$\frac{\partial\theta}{\partial\phi_j} = \frac{\phi_{jyy}\left(\frac{\phi_{jx}}{\phi_{jy}}\right) - \phi_{jxx}\left(\frac{\phi_{jy}}{\phi_{jx}}\right)}{\phi_{jx}^2 + \phi_{jy}^2}$$

Hence, terms (a) - (d) in eq.4.7 are derived in terms of derivatives of field variables ϕ_j and ϕ_k along reference x and y axes

$$\begin{aligned}
\nabla\frac{\partial}{\partial\nabla\phi_j}f_{jk}^{gr} &= -\frac{1}{2}\left(\varepsilon\triangle\phi_k + \frac{\varepsilon_\theta\nabla\phi_k}{\phi_{jx}^2+\phi_{jy}^2}\left(\phi_{jyy}\phi_{jx} - \phi_{jxx}\phi_{jy}\right)\right) \\
&\quad -\frac{1}{2}\left(\varepsilon_{\theta\theta}\nabla\phi_j.\nabla\phi_k\frac{\phi_{jx}-\phi_{jy}}{\left(\phi_{jx}^2+\phi_{jy}^2\right)^2}\left(\phi_{jyy}\phi_{jx} - \phi_{jxx}\phi_{jy}\right)\right) \\
&\quad -\frac{1}{2}\left(\varepsilon_\theta\nabla\phi_j.\nabla\phi_k\frac{\left(\phi_{jxx}-\phi_{jyy}\right)\left(\phi_{jx}^2+\phi_{jy}^2\right) - 2\left(\phi_{jx}-\phi_{jy}\right)\left(\phi_{jx}\phi_{jxx}+\phi_{jy}\phi_{jyy}\right)}{\left(\phi_{jx}^2+\phi_{jy}^2\right)^2}\right) \\
&\quad -\frac{1}{2}\left(\varepsilon_\theta\frac{\left(\phi_{jx}-\phi_{jy}\right)\left(\triangle\phi_{\mathbf{k}}\nabla\phi_j + \triangle\phi_j\nabla\phi_k\right)}{\phi_{jx}^2+\phi_{jy}^2}\right)
\end{aligned}$$

$$\begin{aligned}
\nabla\frac{\partial}{\partial\nabla\phi_j}f_{jk}^{pot} &= \frac{|\phi_j|\,|\phi_k|\,\gamma_\theta}{\left(\phi_{jx}^2+\phi_{jy}^2\right)^2}\left(\left(\phi_{jxx}-\phi_{jyy}\right)\left(\phi_{jx}^2+\phi_{jy}^2\right) - 2\left(\phi_{jx}-\phi_{jy}\right)\left(\phi_{jx}\phi_{jxx}+\phi_{jy}\phi_{jyy}\right)\right) \\
&\quad + |\phi_j|\,|\phi_k|\,\gamma_{\theta\theta}\frac{\left(\phi_{jx}-\phi_{jy}\right)\left(\phi_{jx}\phi_{jyy}-\phi_{jy}\phi_{jxx}\right)}{\left(\phi_{jx}^2+\phi_{jy}^2\right)^2}
\end{aligned}$$

$$\frac{\partial}{\partial\phi_j}f_{jk}^{gr} = -\frac{\varepsilon_\theta\nabla\phi_j.\nabla\phi_k}{2}\left(\frac{\phi_{jx}\left(\frac{\phi_{jyy}}{\phi_{jy}}\right) - \phi_{jy}\left(\frac{\phi_{jxx}}{\phi_{jx}}\right)}{\phi_{jx}^2+\phi_{jy}^2}\right)$$

$$\frac{\partial}{\partial\phi_j}f_{jk}^{pot} = \gamma\,|\phi_k| + \gamma_\theta\,|\phi_j|\,|\phi_k|\left(\frac{\phi_{jx}\left(\frac{\phi_{jyy}}{\phi_{jy}}\right) - \phi_{jy}\left(\frac{\phi_{jxx}}{\phi_{jx}}\right)}{\phi_{jx}^2+\phi_{jy}^2}\right)$$

For three dimensions, the anisotropic function depends both on θ and φ, which denote

the angle that the interface normal n makes with the reference z axis, and the angle that the projection of the normal on the plane of the paper n' makes with the reference x axis respectively [27]. Henceforth, $\varepsilon_{jk}(\theta, \Phi)$ and $\gamma_{jk}(\theta, \varphi)$ are represented by ε and γ respectively.

$$\varepsilon_{jk} = \varepsilon(\theta, \varphi) \tag{4.14}$$

$$\gamma_{jk} = \gamma(\theta, \varphi) \tag{4.15}$$

here, θ and φ can be expressed as

$$cos\varphi = \phi_{jz} \tag{4.16}$$

$$tan\theta = \frac{\phi_{jy}}{\phi_{jx}} \tag{4.17}$$

the terms ϕ_{jx}, ϕ_{jy} and ϕ_{jz} are the gradients of field variable ϕ_j along the x, y and z reference axes respectively. For each of the terms (a)-(d) in eq.4.7, certain intermediate terms are evaluated here.

For term (a) $\left(\nabla \frac{\partial}{\partial \nabla \phi_j} f_{jk}^{gr}\right)$, some of these terms are

$$\partial_{x_i} \varphi = -\frac{\phi_{jzz}}{\sqrt{1 - \phi_{jz}^2}}$$

$$\partial_{x_i} \theta = \frac{\phi_{jyy}\phi_{jx} - \phi_{jxx}\phi_{jy}}{\phi_{jx}^2 + \phi_{jy}^2}$$

$$\partial_{x_i} \varepsilon = -\frac{\varepsilon_\varphi \phi_{jzz}}{\sqrt{1 - \phi_{jz}^2}} + \frac{\varepsilon_\theta}{\phi_{jx}^2 + \phi_{jy}^2} \left(\phi_{jyy}\phi_{jx} - \phi_{jxx}\phi_{jy}\right)$$

$$\frac{\partial}{\partial \nabla \phi_j}\varepsilon = -\frac{\varepsilon_\varphi}{\sqrt{1-\phi_{jz}^2}} + \varepsilon_\theta \frac{\phi_{jx}-\phi_{jy}}{\phi_{jx}^2+\phi_{jy}^2}$$

$$\frac{\partial}{\partial_{x_i}}\varepsilon_\varphi = -\frac{\varepsilon_{\varphi\varphi}\phi_{jzz}}{\sqrt{1-\phi_{jz}^2}} + \frac{\varepsilon_{\theta\varphi}}{\phi_{jx}^2+\phi_{jy}^2}\left(\phi_{jyy}\phi_{jx}-\phi_{jxx}\phi_{jy}\right)$$

$$\frac{\partial}{\partial_{x_i}}\varepsilon_\theta = -\frac{\varepsilon_{\theta\varphi}\phi_{jzz}}{\sqrt{1-\phi_{jz}^2}} + \frac{\varepsilon_{\theta\theta}}{\phi_{jx}^2+\phi_{jy}^2}\left(\phi_{jyy}\phi_{jx}-\phi_{jxx}\phi_{jy}\right)$$

Treatment of term (b) $\left(\nabla \frac{\partial}{\partial \nabla \phi_j} f_{jk}^{pot}\right)$ yields the following derivative

$$\frac{\partial}{\partial \nabla \phi_j}\gamma = \gamma_\theta \frac{\partial}{\partial \nabla \phi_j}\theta + \gamma_\varphi \frac{\partial}{\partial \nabla \phi_j}\varphi \tag{4.18}$$

where,

$$\frac{\partial}{\partial \nabla \phi_j}\varphi = -\frac{1}{\sqrt{1-\phi_{jz}^2}}$$

$$\frac{\partial}{\partial \nabla \phi_j}\theta = \frac{\phi_{jx}-\phi_{jy}}{\phi_{jx}^2+\phi_{jy}^2}$$

Hence,

$$\left(\nabla \frac{\partial}{\partial \nabla \phi_j}\gamma\right) = -\frac{1}{\sqrt{1-\phi_{jz}^2}}\left(\gamma_{\varphi\varphi}\partial_{x_i}\varphi + \gamma_{\theta\varphi}\partial_{x_i}\theta\right) - \gamma_\varphi \partial_{x_i}\left(\frac{1}{\sqrt{1-\phi_{jz}^2}}\right)$$

$$+\frac{\phi_{jx}-\phi_{jy}}{\phi_{jx}^2+\phi_{jy}^2}\left(\gamma_{\theta\varphi}\partial_{x_i}\varphi+\gamma_{\theta\theta}\partial_{x_i}\theta\right)+\gamma_\theta\partial_{x_i}\left(\frac{\phi_{jx}-\phi_{jy}}{\phi_{jx}^2+\phi_{jy}^2}\right)$$

since,$\nabla\frac{\partial}{\partial\nabla\phi_j}\left|\phi_j\right|\left|\phi_k\right|$ is identical to zero, term (b) reduces to

$$\nabla\frac{\partial}{\partial\nabla\phi_j}f_{jk}^{pot}=\left|\phi_j\right|\left|\phi_k\right|\left(\nabla\frac{\partial}{\partial\nabla\phi_j}\gamma\right) \tag{4.19}$$

term (c) $\left(\frac{\partial}{\partial\phi_j}f_{jk}^{gr}\right)$ can be evaluated to be

$$\frac{\partial}{\partial\phi_j}f_{jk}^{gr}=\nabla\phi_j\nabla\phi_k\left(\varepsilon_\varphi\frac{\partial}{\partial\phi_j}\varphi+\varepsilon_\theta\frac{\partial}{\partial\phi_j}\theta\right) \tag{4.20}$$

similarly, for the variation of the potential energy f_{jk}^{pot} with ϕ_j (term (d))

$$\frac{\partial}{\partial\phi_j}\gamma=\gamma_\theta\frac{\partial}{\partial\phi_j}\theta+\gamma_\varphi\frac{\partial}{\partial\phi_j}\varphi \tag{4.21}$$

where,

$$\frac{\partial}{\partial\phi_j}\varphi=-\frac{\phi_{jzz}}{\phi_{jz}\sqrt{1-\phi_{jz}^2}}$$

$$\frac{\partial}{\partial\phi_j}\theta=\frac{-\left(\frac{\phi_{jxx}}{\phi_{jx}}\right)\phi_{jy}+\left(\frac{\phi_{jyy}}{\phi_{jy}}\right)\phi_{jx}}{\phi_{jx}^2+\phi_{jy}^2}$$

Hence, term (d) reduces to

$$\frac{\partial}{\partial\phi_j}f_{jk}^{pot}=\gamma\left|\phi_k\right|+\left|\phi_j\right|\left|\phi_k\right|\left(\gamma_\theta\frac{\partial}{\partial\phi_j}\theta+\gamma_\varphi\frac{\partial}{\partial\phi_j}\varphi\right) \tag{4.22}$$

It should be noted that an alternate (and more elegant) reformulation based on the capillarity vector ξ is possible [72, 73].

Appendix B

Numerical implementation

As explained in the previous appendix (Appendix A), the variation of the free-energy functional can be described completely in terms of the phase-field variables and their derivatives. At any given instant t, the derivatives at position x_i can be determined using relevant phase-field values within a stencil of appropiate length on uniform (cartesian) grids. The length of the stencil needed increases with the order of the approximation. Note that in the present work, we use centered derivatives, hence for locations near domain boundaries, use of a ghost layer (of adequate thickness) with periodic boundary conditions is requisite.

Expressions for first (and higher) centered derivatives are given below. It is to be noted that although these are defined for a particular reference axis (x in this case), corresponding definitions along other reference axes (y and z) can be derived. The discretization interval h chosen in this case is unity. The order of the error terms are also worthy of mention.

$$\phi_{jx,x_i} = \left(-\frac{\phi_{j,x_{i-1}}}{2} + \frac{\phi_{j,x_{i+1}}}{2} \right) \frac{1}{h} + O\left(h^2\right) \tag{4.23}$$

$$\phi_{jx,x_i} = \left(\frac{\phi_{j,x_{i-2}}}{12} - \frac{2\phi_{j,x_{i-1}}}{3} + \frac{2\phi_{j,x_{i+1}}}{3} - \frac{\phi_{j,x_{i+2}}}{12} \right) \frac{1}{h} + O\left(h^4\right) \tag{4.24}$$

$$\phi_{jxx,x_i} = \left(\phi_{j,x_{i-1}} - 2\phi_{j,x_i} + \phi_{j,x_{i+1}} \right) \frac{1}{h^2} + O\left(h^2\right) \tag{4.25}$$

$$\phi_{jxx,x_i} = \left(\frac{\phi_{j,x_{i-3}}}{90} - \frac{3\phi_{j,x_{i-2}}}{20} + \frac{3\phi_{j,x_{i-1}}}{2} - \frac{49\phi_{j,x_i}}{18} + \frac{3\phi_{j,x_{i+1}}}{2} - \frac{3\phi_{j,x_{i+2}}}{20} + \frac{\phi_{j,x_{i+3}}}{90} \right) \frac{1}{h^2} + O\left(h^5\right) \tag{4.26}$$

In the present formulation, we use second-order approximations for the first derivative (eq.4.23) and fifth-order approximations for the second derivative (eq.4.26). The gradient

$(\nabla\phi_j)$ and laplacian $(\triangle\phi_j)$ can then be defined as follows

$$\nabla\phi_j = \phi_{jx}\hat{x} + \phi_{jy}\hat{y} + \phi_{jz}\hat{z} \tag{4.27}$$

$$\triangle\phi_j = \phi_{jxx} + \phi_{jyy} + \phi_{jzz} \tag{4.28}$$

Near grid edges a perodic boundary condition (PBC) is used, and grid values (of an appropiate width depending on the length of the stencil required) on the opposite end are used (as in fig. 2.4).

To determine boundary inclination (θ for two dimensions and (θ, φ) for three dimensions), weighted essentially non-oscillatory (WENO) schemes are used to approximate gradients along reference x, y (and z) axes. A brief formulation has been extracted from Shu's paper (refer [59]). Details for numerical implementation can be found in [60]. The motivation for using this particular scheme is its non-oscillatory behavior near discontinuities (in the present framework, this could be due to sharp corners along grain boundaries or due to faceted grain shapes, where there is a sudden change or jump in the inclination of the boundary normal [13]). First derivatives are expressed as

$$\phi_{jx,x_i} \approx \frac{1}{h}\left(\phi_{j,i+1/2} - \phi_{j,i-1/2}\right) \tag{4.29}$$

where the fifth-order WENO approximation is represented as the summation of weighted third-order derivatives on adjacent stencils as

$$\phi_{j,i+1/2} = w_1\phi^{(1)}_{j,i+1/2} + w_2\phi^{(2)}_{j,i+1/2} + w_3\phi^{(3)}_{j,i+1/2} \tag{4.30}$$

where,

$$\phi^{(1)}_{j,i+1/2} = \frac{1}{3}\phi_{j,i-2} - \frac{7}{6}\phi_{j,i-1} + \frac{11}{6}\phi_{j,i}$$

$$\phi^{(2)}_{j,i+1/2} = -\frac{1}{6}\phi_{j,i-1} + \frac{5}{6}\phi_{j,i} + \frac{1}{3}\phi_{j,i+1}$$

$$\phi^{(3)}_{j,i+1/2} = \frac{1}{3}\phi_{j,i} + \frac{5}{6}\phi_{j,i+1} - \frac{1}{6}\phi_{j,i+2}$$

The non-linear weights w_i are given by

$$w_i = \frac{\tilde{w_i}}{\sum_{k=1}^{3} \tilde{w_k}}$$

$$\tilde{w_k} = \frac{\lambda_k}{(\epsilon + \beta_k)^2}$$

with $\lambda_1 = \frac{1}{10}$, $\lambda_2 = \frac{3}{5}$, $\lambda_3 = \frac{3}{10}$, $\epsilon = 10^{-6}$ and

$$\beta_1 = \frac{13}{12}\left(\phi_{j,i-2} - 2\phi_{j,i-1} + \phi_{j,i}\right)^2 + \frac{1}{4}\left(\phi_{j,i-2} - 4\phi_{j,i-1} + 3\phi_{j,i}\right)^2$$

$$\beta_2 = \frac{13}{12}\left(\phi_{j,i-1} - 2\phi_{j,i-1} + \phi_{j,i+1}\right)^2 + \frac{1}{4}\left(\phi_{j,i-1} - \phi_{j,i+1}\right)^2$$

$$\beta_3 = \frac{13}{12}\left(\phi_{j,i} - 2\phi_{j,i+1} + \phi_{j,i+2}\right)^2 + \frac{1}{4}\left(3\phi_{j,i} - 4\phi_{j,i+1} + \phi_{j,i+2}\right)^2$$

The terms (a-d) in eq.4.7 in Appendix A can then be calculated for a location (x, y, z) at time t. A forward difference technique is used to update phase-field values $\phi_{j(x,y,z)}(t + dt)$ based on previous values $\phi_{j(x,y,z)}(t)$ using the TDGL equation.

$$\phi_j(t + dt) = \phi_j(t) + \frac{2}{N} * M * \frac{\delta F}{\delta \phi_j} dt \tag{4.31}$$

where, N, M and F denote the number of non-zero fields at (x, y, z) (at time t), the value of mobility and the free energy functional respectively.

Appendix C

Incorporating interpolated energies in the interface-field method

The energy of a grain boundary of arbitrary misorientation and plane normal is calculated using the predetermined values in the five-dimensional energy matrix. The corresponding misorientation indices $[c_1, c_2, c_3]$ are determined using eq.3.9. Since the grain boundary energy can be discontinuous in misorientation space, but should be continuous in inclination space, the following methodology is adopted. This is to ensure that for a curved boundary, which has constant misorientation throughout its length, the energy varies with inclination in a continuous fashion, and does not suffer from discontinuities in energy as the boundary inclination passes through a cell boundary in the inclination space.

As in fig.4.1, the variation of GB energy with inclination is linear and continuous in both dimensions (of the inclination space), at a constant misorientation. The boundary inclination is denoted by $[l_4, l_5]$, where $[l_4, l_5]$ are not restricted to integer values and assume exact (fractional) values determined as

$$l_4 = CD_2 * \hat{n}_z \tag{4.32}$$

$$l_5 = 2 * CD_2 * tan^{-1}\left(\frac{\hat{n}_y}{\hat{n}_x}\right)/\pi \tag{4.33}$$

where, $[n_x, n_y, n_z]$ denote the normal indices in the crystal reference frame.

The weights (w, w') are determined to be

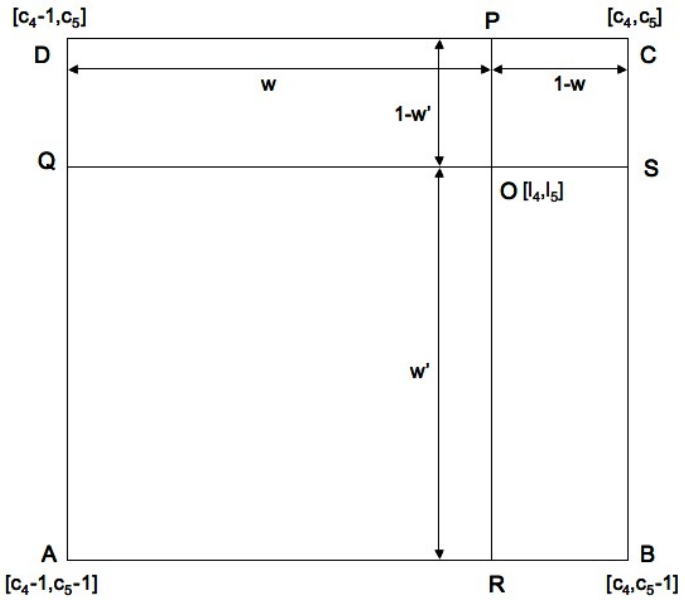

Figure 4.1: Bilinear interpolation for variation of boundary energy with inclination at constant misorientation.

$$w = l_4 - (c_4 - 1) \tag{4.34}$$

$$w' = l_5 - (c_5 - 1) \tag{4.35}$$

and the boundary energies at points P, Q, R and S to be

$$\gamma_p(c_1, c_2, c_3) = w\gamma_C(c_1, c_2, c_3) + (1 - w)\gamma_D(c_1, c_2, c_3) \tag{4.36}$$

$$\gamma_Q(c_1, c_2, c_3) = w'\gamma_D(c_1, c_2, c_3) + (1 - w')\gamma_A(c_1, c_2, c_3) \tag{4.37}$$

$$\gamma_R(c_1, c_2, c_3) = w\gamma_B(c_1, c_2, c_3) + (1 - w)\gamma_A(c_1, c_2, c_3) \tag{4.38}$$

$$\gamma_S(c_1, c_2, c_3) = w'\gamma_C(c_1, c_2, c_3) + (1 - w')\gamma_B(c_1, c_2, c_3) \tag{4.39}$$

The grain boundary energy at intermediate inclination $O[l_4, l_5]$ is calculated to be

$$\gamma_O(c_1, c_2, c_3) = \frac{w\gamma_S(c_1, c_2, c_3) + (1-w)\gamma_Q(c_1, c_2, c_3) + w'\gamma_P(c_1, c_2, c_3) + (1-w')\gamma_R(c_1, c_2, c_3)}{2} \tag{4.40}$$

In the figure below (fig. 4.2), the continuity of boundary energies in inclination space (at a constant arbitrary misorientation) is shown. Arbitrary values of energy are chosen for the corners in inclination space (points $A - D$ in preceding fig. 4.1).

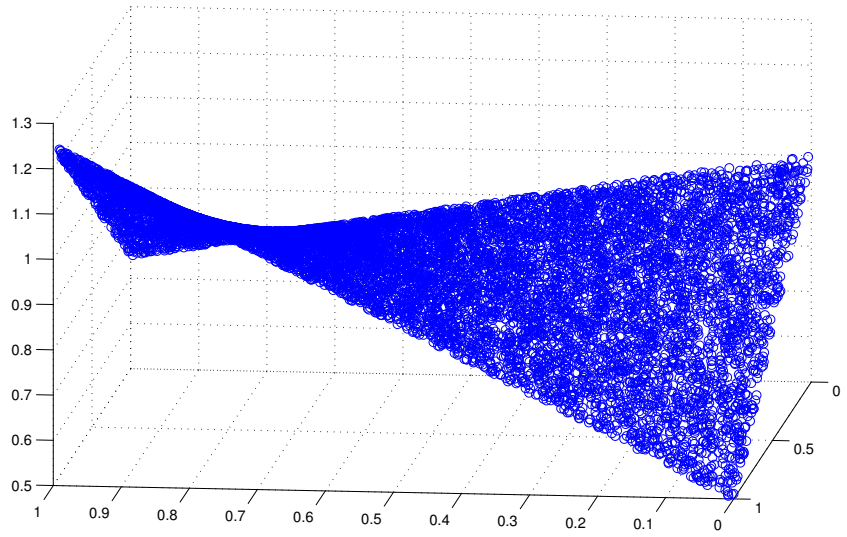

Figure 4.2: Boundary energies in inclination space at arbitrary misorientation. Note that energy values (along the vertical axis) are in a.u.

Appendix D

Junction Extension

As stated before, it is difficult to compute boundary normals accurately in a junction region, where there are three or more non-zero phase fields, even with the WENO formalism [59]. Values of the boundary energy computed using these normals are inaccurate, and methods

that depend on these values are unstable.

Junction extension is a numerical procedure that permits us to sidestep this difficulty. It does so by replacing inaccurate values by the value that is computed at the closest relevant grain boundary point, i.e. a point at which there are only two non-zero phase fields. Values computed along grain boundaries are *extended* into all relevant junction regions.

The extension procedure for any single boundary is simple to visualize, and is depicted schematically in fig.2.7. During an initial grid traversal, the boundary inclination is computed at any point where there are only two non-zero phase fields, and the corresponding boundary energy is stored. These values are then permitted to percolate through any adjacent multi-junction region, as follows. Iterate through all the junction points. If the boundary energy at the current point is zero, and if any of the adjacent values are non-zero, compute and store the average of all neighboring non-zero values. Repeat, until all junction values are non-zero.

There are several challenges that must be overcome to implement a fast and memory-efficient version of this algorithm. It is unreasonable, for instance, to search the entire grid for junction points at each loop iteration, by determining how many non-zero phases are stored at the current grid point. Instead, during the first grid traversal, when energies are computed and stored along the boundaries, we choose to store a linked list of those grid coordinates that correspond to all junction points. Iteration then requires simply traversing this list, and the phase field update may be completed by traversing this list as well. The computational time required for junction extension decreases as the average grain size increases.

A complication also arises from the need to identify relevant boundaries, given the set of non-zero phase fields $\{\phi_i\}$ at any point. If there are N nonzero phases, there are potentially $\frac{N(N-1)}{2}$ relevant boundaries. In the initial microstructure, or during grain collapse, N can become rather large; a considerable amount of memory can be required to store all of these junction energies. In addition, it is not necessary that any given pair of phase fields (a, b) corresponds to a boundary region in which we have computed the energy e_{ab}. During topo-

logical changes, boundaries are created and destroyed, but the corresponding phase fields are present and non-zero at junctions both before and after the transformation takes place. For these reasons, no matter how many non-zero phases are in fact present, we only extend values associated with the three interface fields $\psi_{01} = \phi_0 - \phi_1$, $\psi_{02} = \phi_0 - \phi_2$, and $\psi_{12} = \phi_1 - \phi_2$, where the phase fields have been ordered $\phi_0 > \phi_1 > \phi_2$. During the subsequent phase field update, any interface field for which extension has not produced a non-zero value is assumed to have energy $e_{ab} = 1.0$.

And finally, extension is a process that depends on the derived interface fields, and not the phase fields. To ensure that boundary extension is disjoint from one boundary to the next, we use a sparse, doubly-indexed data structure to store the boundary energies at every grid node [18]. In other words, the energy associated with the interface field ψ_{ab} is stored and accessed as the triplet (a, b, ψ_{ab}). Any interface field ψ_{ab} for which a corresponding energy is not stored is assigned an energy identical to $e_{ab} = 0$.

The resulting junction extension method is relatively fast - on average, only 10-20 iterations are needed.

Appendix E

Filling the 5-parameter space with SNL energies

The following procedure is used to fill up the energy space (the value in cell $[c_1, c_2, c_3, c_4, c_5]$ equals to the energy of the corresponding GB type) using the GB energies extracted for *388* GB types *(Sandia)*.

1. For each of the *388* type (say *kth*), the orientations for grain **A** and **B** are expressed as active rotation matrices g_A and g_B respectively (as in *dsc_csl.txt*). These are post-multiplied by the *ith* (and *jth*) symmetry operator as in $g_A O_A$ and $g_B O_B$.

2. The misorientation between these grains (in the crystal frame) is expressed as (note

that in the sample frame the misorientation for active rotations is $\triangle g_{AB,active} = (g_B O_B)(g_A O_A)^{-1}$ in contrast to the expression below)

$$\triangle g_{AB,active} = (g_A O_A)^{-1}(g_B O_B) \tag{4.41}$$

3. The corresponding Euler angles for $\triangle g_{AB,active}$ are determined as (ϕ_1, Φ, ϕ_2). If all three are less than 90°, the corresponding indices in misorientation space $[c_1, c_2, c_3]$ are calculated, then we proceed to step 4, else go to step 7.

$$\begin{aligned} c_1 &= 2 * CD * \phi_1/\pi \\ c_2 &= CD * cos\Phi \\ c_3 &= 2 * CD * \phi_2/\pi \end{aligned}$$

4. The normal vector (in crystal frame) for grain A and B can be expessed as the 1st row of the matrices $g_A O_A$ and $g_B O_B$

$$n_{xA} = g_A O_A(1,1) \tag{4.42}$$

$$n_{yA} = g_A O_A(1,2) \tag{4.43}$$

$$n_{zA} = g_A O_A(1,3) \tag{4.44}$$

5. For the normal n_A (and n_B) the angular variables (θ, φ) are computed which give the corresponding indices in inclination space $[c_4, c_5]$

$$\theta = cos^{-1}\left(\frac{c_4}{CD_2}\right) \tag{4.45}$$

$$\varphi = \frac{\pi c_5}{2CD_2} \tag{4.46}$$

6. The cells $[c_1, c_2, c_3, c_{4A}, c_{5A}]$ and $[c_1, c_2, c_3, c_{4B}, c_{5B}]$ are assigned the energy of the kth (of the 388) GB type.

7. The misorientation is then expressed as the transpose $g^T_{AB,active} = (g_B O_B)^{-1}(g_A O_A)$ and steps $3-6$ are repeated.

8. The (active rotation) matrices g_A and g_B are then are then exchanged and steps $1-7$ are repeated.

9. We repeat steps $1-8$ for the $(i+1)th$ (and $(j+1)th$) symmetry operator where i, j vary independently as $1 \leq i \leq 24, 1 \leq j \leq 24$.

10. For cell $[c_1, c_2, c_3, c_4, c_5]$ in the energy space we compute the energy as an average.

In the following figures we plot the energy variation at specific misorientations for $CD = 9, CD_2 = 9$. Note that not all cells are $filled$, only those cells that correspond to one of the *388* GB types (or one of their crystallographic equivalents) are $non-zero$.

Bibliography

[1] S.M. Allen and J.W. Cahn. A microscopic theory for antiphase boundary motion and its application to antiphase domain coarsening. *Acta Metallurgica*, 27(6):1085–1095, 1979.

[2] M.P. Anderson, G.S. Grest, and D.J. Srolovitz. Computer simulation of normal grain growth in three dimensions. *Phil. Mag. B*, 59(3):293–329, 1989.

[3] M.P. Anderson, D. Srolovitz, and G.S. Grest. Computer simulation of grain growth–i. kinetics. *Acta metallurgica*, Jan 1984.

[4] H. Brooks. *Metal Interfaces*. 1952.

[5] J.W. Cahn and D. Hoffman. A vector thermodynamics for anisotropic surfaces: I. fundamentals and application to plane surface junctions. *Surface Science*, 31:368–388, 1972.

[6] J.W. Cahn and D. Hoffman. A vector thermodlnamics for anisotropic surfaces–ii. curved and faceted surfaces. *Acta metall.*, 22(10):1205–1214, 1974.

[7] J.W. Cahn and J.E. Taylor. Metrics, measures, and parametrizations for grain boundaries: a dialog. *Journal of Materials Science*, Jan 2006.

[8] L.Q. Chen. Phase field models for microstructure evolution. *Annual Review of Materials Research*, 32(1):113–140, 2002.

[9] L.Q. Chen and Y. Wang. The continuum field approach to modeling microstructural evolution. *Jom*, 48(12):13–18, 1996.

[10] K.; Courant, R.; Friedrichs and H. Lewy. On the partial difference equations of mathematical physics. *IBM J.*, 11:215–234, 1967.

[11] J.M. Debierre, A. Karma, F. Celestini, and R. Guérin. Phase-field approach for faceted solidification. *Physical Review E*, 68(4):41604, 2003.

[12] S.J. Dillon and G.S. Rohrer. Mechanism for the development of anisotropic grain boundary character distributions during normal grain growth. *Acta Materialia*, 57(1):1–7, 2009.

[13] J.J. Eggleston, G.B. McFadden, and P.W. Voorhees. A phase-field model for highly anisotropic interfacial energy. *Physica D: Nonlinear Phenomena*, 150(1-2):91–103, 2001.

[14] G. Gottstein. On the orientation dependence of grain boundary energy and mobility. *Materials Science Forum*, Jan 1992.

[15] G. Gottstein, A.H. King, and L.S. Shvindlerman. The effect of triple-junction drag on grain growth. *Acta Materialia*, 48(2):397–403, 2000.

[16] G. Gottstein and L.S. Shvindlerman. Triple junction drag and grain growth in 2d polycrystals. *Acta Materialia*, 50(4):703–713, 2002.

[17] J. Gruber, D.C. George, A.P. Kuprat, G.S. Rohrer, and A.D. Rollett. Effect of anisotropic interfacial energy on grain boundary distributions during grain growth. *Materials Science Forum*, 467:733–738, 2004.

[18] J. Gruber, N. Ma, Y., A.D. Rollett, and G.S. Rohrer. Sparse data structure and algorithm for the phase field method. *Modelling and Simulation in Materials Science and Engineering*, 14:1189, 2006.

[19] J. Gruber, H.M. Miller, T.D. Hoffmann, G.S. Rohrer, and A.D. Rollett. Misorientation texture development during grain growth. part i: Simulation and experiment. *Acta Materialia*, 57(20):6102–6112, 2009.

[20] J. Gruber, A.D. Rollett, and G.S. Rohrer. Misorientation texture development during grain growth. part ii: Theory. *Acta Materialia*, 58(1):14–19, 2010.

[21] W. Guo, R. Spatschek, and I. Steinbach. An analytical study of the static state of multi-junctions in a multi-phase field model. *Physica D: Nonlinear Phenomena*, Jan 2010.

[22] M. Hillert. On the theory of normal and abnormal grain growth. *Acta metall.*, 13(3):227–238, 1965.

[23] E.A. Holm, G.N. Hassold, and M.A. Miodownik. On misorientation distribution evolution during anisotropic grain growth. *Acta Materialia*, 49(15):2981–2991, 2001.

[24] C.E. Krill Iii and L.Q. Chen. Computer simulation of 3-d grain growth using a phase-field model. *Acta Materialia*, 50(12):3059–3075, 2002.

[25] O. Ivasishin, S. Shevchenko, and N. Vasiliev. 3d monte-carlo simulation of texture-controlled grain growth. *Acta Materialia*, Jan 2003.

[26] D. Kar, S.D. Sintay, G.S. Rohrer, and A.D. Rollett. Role of inclination dependent anisotropy on boundary populations during two-dimensional grain growth.

[27] A. Karma and W.J. Rappel. Quantitative phase-field modeling of dendritic growth in two and three dimensions. *Physical Review E*, 57(4):4323–4349, 1998.

[28] A. Kazaryan, Y., S.A. Dregia, and B.R. Patton. Generalized phase-field model for computer simulation of grain growth in anisotropic systems. *Physical Review B*, 61(21):14275–14278, 2000.

[29] S.G. Kim, D.I. Kim, W.T. Kim, and Y.B. Park. Computer simulations of two-dimensional and three-dimensional ideal grain growth. *Physical Review E*, 74(6):61605, 2006.

[30] D. Kinderlehrer, I. Livshits, G.S. Rohrer, S. Ta'asan, and P. Yu. Mesoscale simulation of the evolution of the grain boundary character distribution. *Materials Science Forum*, 467:1063–1068, 2004.

[31] Y Kwon, K Thornton, and PW Voorhees. Coarsening of bicontinuous structures via nonconserved and conserved dynamics. *Physical Review E*, 75(2):21120, 2007.

[32] J. Li, S.J. Dillon, and G.S. Rohrer. Relative grain boundary area and energy distributions in nickel. *Acta Materialia*, 57(14):4304–4311, Aug 2009.

[33] I. Loginova, J. Ågren, and G. Amberg. On the formation of widmanstätten ferrite in binary fe-c-phase-field approach. *Acta Materialia*, 52(13):4055–4063, 2004.

[34] N. Ma, Q. Chen, and Y. Wang. Implementation of high interfacial energy anisotropy in phase field simulations. *Scripta materialia*, 54(11):1919–1924, 2006.

[35] N. Ma, A. Kazaryan, S.A. Dregia, and Y. Wang. Computer simulation of texture evolution during grain growth: effect of boundary properties and initial microstructure. *Acta Materialia*, 52(13):3869–3879, 2004.

[36] R. MacPherson and D. Srolovitz. The von neumann relation generalized to coarsening of three-dimensional microstructures. *Nature*, Jan 2007.

[37] A. Mastroberardino and B.J. Spencer. Three-dimensional equilibrium crystal shapes with corner energy regularization. *IMA Journal of Applied Mathematics*, Jan 2010.

[38] G.B. McFadden, A.A. Wheeler, R.J. Braun, S.R. Coriell, and R.F. Sekerka. Phase-field models for anisotropic interfaces. *Physical Review E*, 48(3):2016–2024, 1993.

[39] I.M. McKenna, M.P. Gururajan, and P.W. Voorhees. Phase field modeling of grain growth: effect of boundary thickness, triple junctions, misorientation, and anisotropy. *Journal of materials science*, 44(9):2206–2217, 2009.

[40] N. Moelans, B. Blanpain, and P. Wollants. Quantitative analysis of grain boundary properties in a generalized phase field model for grain growth in anisotropic systems. *Physical Review B*, 78(2):24113, 2008.

[41] N. Moelans, B. Blanpain, and P. Wollants. Quantitative phase-field approach for simulating grain growth in anisotropic systems with arbitrary inclination and misorientation dependence. *Physical review letters*, 101(2):25502, 2008.

[42] N. Moelans, F. Wendler, and B. Nestler. Comparative study of two phase-field models for grain growth. *Computational Materials Science*, 46(2):479–490, Aug 2009.

[43] A. Morawiec. Method to calculate the grain boundary energy distribution over the space of macroscopic boundary parameters from the geometry of triple junctions. *Acta Materialia*, Jan 2000.

[44] A Morawiec. Models of uniformity for grain boundary distributions. *Journal of Applied Crystallography*, 42(5):783–792, Aug 2009.

[45] W. Mullins. Two?dimensional motion of idealized grain boundaries. *Journal of Applied Physics*, 27(8):900–904, 1956.

[46] R. Napolitano and S. Liu. Three-dimensional crystal-melt wulff-shape and interfacial stiffness in the al-sn binary system. *Physical Review B*, 70(21):214103, Dec 2004.

[47] R.E. Napolitano, S. Liu, and R. Trivedi. Experimental measurement of anisotropy in crystal-melt interfacial energy. *Interface Science*, 10(2):217–232, 2002.

[48] D. Olmsted. A new class of metrics for the macroscopic crystallographic space of grain boundaries. *Acta Materialia*, Jan 2009.

[49] D. Olmsted and S. Foiles. Survey of computed grain boundary properties in face-centered cubic metals: I. grain boundary energy. *Acta Materialia*, Jan 2009.

[50] A. Otsuki. Variation of energies of aluminum [001] boundaries with misorientation and inclination. *Materials Science Forum*, Jan 1996.

[51] G. Palumbo and E. Lehockey. Applications for grain boundary engineered materials. *JOM Journal of the Minerals*, Jan 1998.

[52] T. Pusztai, G. Tegze, G.I. Tóth, L. Környei, G. Bansel, Z. Fan, and L. Gránásy. Phase-field approach to polycrystalline solidification including heterogeneous and homogeneous nucleation. *Journal of Physics: Condensed Matter*, 20:404205, 2008.

[53] W. Rappel and A. Karma. Quantitative phase-field modeling of dendritic growth in two and three dimensions. *APS Meeting Abstracts*, Jan 1996.

[54] W.T. Read and W. Shockley. Dislocation models of crystal grain boundaries. *Phys. Rev.*, 78:275–289, 1990.

[55] G.S. Rohrer, D.M. Saylor, B.S. El-Dasher, B.L. Adams, A.D. Rollett, and P. Wynblatt. The distribution of internal interfaces in polycrystals. *Z. Metall*, 95:197–214, 2004.

[56] D.M. Saylor, B.S. El Dasher, A.D Rollett, and G.S. Rohrer. Distribution of grain boundaries in aluminum as a function of five macroscopic parameters. *Acta Materialia*, 52(12):3649–3655, 2004.

[57] D.M. Saylor, A. Morawiec, and G.S. Rohrer. The relative free energies of grain boundaries in magnesia as a function of five macroscopic parameters. *Acta Materialia*, 51(13):3675–3686, 2003.

[58] R. Sekerka. Analytical criteria for missing orientations on three-dimensional equilibrium shapes. *Journal of crystal growth*, Jan 2005.

[59] C.W. Shu. High-order finite difference and finite volume weno schemes and discontinuous galerkin methods for cfd. *International Journal of Computational Fluid Dynamics*, 17(2):107–118, 2003.

[60] C.W. Shu and G.S. Jiang. Efficient implementation of weighted eno schemes. 1995.

[61] S. Sintay and A.D. Rollett. Dual grid approach for meshing 3d images. *Proc. Minerals, Metals, Materials Soc. AIME*, Feb 2010.

[62] D. Srolovitz, M.P. Anderson, and P. Sahni. Computer simulation of grain growth–ii. grain size distribution, topology, and local dynamics. *Acta metallurgica*, Jan 1984.

[63] I. Steinbach and F. Pezzolla. A generalized field method for multiphase transformations using interface fields. *Physica D: Nonlinear Phenomena*, 134(4):385–393, 1999.

[64] Y. Suwa, Y. Saito, and H. Onodera. Computer simulation of grain growth in three dimensions by the phase field model with anisotropic grain-boundary mobilities. *Materials Science Forum*, 539:2437–2442, 2007.

[65] J.E. Taylor and J.W. Cahn. Diffuse interfaces with sharp corners and facets: Phase field models with strongly anisotropic surfaces. *Physica D: Nonlinear Phenomena*, 112(3-4):381–411, 1998.

[66] S. Torabi, J. Lowengrub, A. Voigt, and S. Wise. A new phase-field model for strongly anisotropic systems. *Proceedings of the Royal Society A: Mathematical, Physical and Engineering Science*, 465(2105):1337, 2009.

[67] T. Uehara and R.F. Sekerka. Phase field simulations of faceted growth for strong anisotropy of kinetic coefficient. *Journal of crystal growth*, 254(1-2):251–261, 2003.

[68] M. Upmanyu, G.N. Hassold, A. Kazaryan, E.A. Holm, Y., B. Patton, and D.J. Srolovitz. Boundary mobility and energy anisotropy effects on microstructural evolution during grain growth. *Interface Science*, 10(2):201–216, 2002.

[69] J von Neumann. *Metal Interfaces*. 1952.

[70] F. Wakai and N. Enomoto. Three-dimensional microstructural evolution in ideal grain growth–general statistics. *Acta Materialia*, Jan 2000.

[71] Eric W. Weisstein. Courant-friedrichs-lewy condition. *Mathworld*.

[72] A.A. Wheeler and G.B. McFadden. A -vector formulation of anisotropic phase-field models: 3d asymptotics. *European Journal of Applied Mathematics*, 7(4):367–381, 1996.

[73] A.A. Wheeler and G.B. McFadden. On the notion of a Ðvector and a stress tensor for a general class of anisotropic diffuse interface models. *Proceedings of the Royal Society of London. Series A: Mathematical, Physical and Engineering Sciences*, 453(1963):1611–1630, 1997.